Large-eddy Simulation of Turbulent Boundary Layers with Spatially Varying Roughness

Thesis by
Akshay Sridhar

In Partial Fulfillment of the Requirements for the
Degree of
Doctor of Philosophy

CALIFORNIA INSTITUTE OF TECHNOLOGY
Pasadena, California

2019
Defended 21 August 2018

Akshay Sridhar
ORCID: 0000-0002-2642-8246

Priya, Amma, Appa

ACKNOWLEDGEMENTS

I would like to thank Professor Dale Pullin for his advice over the years, beginning with his mentorship during my first year of classes at Caltech, and continuing on as my research advisor over the last four years. His insights on scientific research, teaching and mentorship, his feedback on manuscripts, presentations and on general progress in our meetings has been extremely helpful. I am grateful for the financial support under KAUST OCRF Award No. URF/1/1394-01 and partially under NSF award CBET 1235605. The William Pickering and Stanback STEM fellowships have also enabled my pursuit of doctoral research. I extend my thanks to Profs. McKeon, Colonius and Meiron for serving on my candidacy committee. Their feedback at a crucial stage of the research process has been helpful in shaping my dissertation. Thanks also to the boundary layer group (Profs. Chung and Hutchins, and M.Li) at the University of Melbourne whose willingness to discuss experimental results has been very helpful. I also thank my dissertation committee, Profs Pullin, McKeon, Hornung and Callies for their willingness to provide feedback on this dissertation. I have appreciated the opportunity to present this work to the extended GALCIT community through the FMRC meetings.

The BASE11/AMP mentorship program has been an excellent experience, and I thank Profs McKeon and Pullin for supporting my involvement therein, the other mentors and volunteers for stepping up to inspire young scientists and to Jamie, for helping everything run smoothly.

To the other members of the Pullin group, conversations with you about work and otherwise have always been welcome, and have provided an excellent platform for informal discussion; Wan, for helping me get started with the LES code, and to Noah, Dustin, Wouter who have been great friends and colleagues - I wish them all the best. Barbara and Christine, thanks for making administration work seamless for us!

To the 2013 GALCIT crew, your support and encouragement through classes and exams has been great. Thank you. Laura, Daniel and the ISP team, you've been great friends since I first landed in Pasadena, thanks for your support and help over the years.

Thanks to my cousins, aunt and uncle in T.O. for hosting me time and time again, it's comforting to know family is always nearby. Go Pack Go!

I have had the pleasure of sharing the GALCIT experience with some exceptional people: Arnold (the 14 hour pre-quals roadtrip to Portland will remain a driving record for a long time), Paul (we were on TV playing rugby 7s together! Hiking around *La Avenidas de los Volcanes* will be a good memory for life), Nelson (cheers for the video-game breaks!) - we've shared good laughs, and conversations about ups and downs these last few years, and I hope we continue trading stories beyond our time at graduate school. Thanks to all my GALCIT friends for being their awesome, lively selves (our Zion and Seqouia trip and weekend hangouts will forever provide funny stories).

Thank you, my dearest Kiwi friends; Claire, Georgina, Adam for staying in touch over my time at graduate school. I wish you the best in your lives; you are destined for fulfilling, exciting futures.

My wonderful, supportive family; I love you all. It's not always easy being away for so long, yet you have always been with me through this journey. You are brave, strong people and I'm incredibly grateful that you are there for me, always. I hope I've made you proud. *Kia Kaha*.

"It's a magical world, Hobbes, ol' buddy... Let's go exploring!"

Bill Watterson, 1995

ABSTRACT

This dissertation addresses high Reynolds number turbulent boundary layers flows with different inhomogeneous surface roughness distributions using large eddy simulations. The stretched vortex subgrid scale model for the outer flow LES is coupled with a virtual-wall model for the friction velocity with a correction accounting for local roughness effects.

A semi-empirical model that describes a fully developed rough-walled turbulent boundary layer with sand-grain roughness length-scale $k_s = \alpha x$ that varies linearly with streamwise distance is first developed, with α a dimensionless constant. For large Re_x and a free-stream velocity $U_\infty \propto x^m$, a simple log-wake model of the local turbulent mean-velocity profile is used that contains a standard mean-velocity correction for the asymptotic, fully rough regime. A two parameter (α, m) family of solutions is obtained for which U_∞^+ (or equivalently C_f) and boundary-layer measures can be calculated. These correspond to perfectly self-similar boundary-layer growth in the streamwise direction with similarity variable $z/(\alpha\, x)$ where z is the wall-normal co-ordinate. Results over a range of α are discussed for cases including the zero-pressure gradient ($m = 0$) and sink-flow ($m = -1$) boundary layers. Model trends are supported by high Re wall-modeled LES. Linear streamwise growth of boundary layer measures is confirmed, while for each α, mean-velocity profiles and streamwise turbulent stresses are shown to collapse against $z/(\alpha\, x)$. Inner scaled velocity defects are shown to collapse against z/Δ, where Δ is the Rotta-Clauser parameter. The present results suggest that these flows may be interpreted as the fully-rough limit for boundary layers in the presence of small-scale, linear roughness.

Next, an LES study of a flat-plate turbulent boundary layer at high Re under non-equilibrium flow conditions due to the presence of abrupt changes in surface roughness is presented. Two specific cases, smooth-rough (SR) and rough-smooth (RS) transition are examined in detail. Streamwise developing velocity and turbulent stress profiles are considered and sharp departures from equilibrium flow properties with subsequent relaxation are shown downstream. Relaxation trends are studied using integral parameters and higher-order mean flow statistics with emphasis on Re_τ and k_s^+ dependence. Results are compared with RS experiments at matched Re_τ, and show good agreement in terms of recovery rates.

Finally, the case of static, impulsive wall-roughness in flows at high Re is addressed

using the same LES framework. The initial perturbation from smooth-to-rough appears to dominate the flow behaviour with the length of the impulsive patch showing little effect on recovery rates at matched Re_τ and k_s^+. The resulting trends show good agreement with low Re experiments and support the wall-modeled LES framework as a suitable method for analysing high Re flows in practical applications.

PUBLISHED CONTENT AND CONTRIBUTIONS

[1] A. Sridhar, D. I. Pullin, and W. Cheng. “Rough-wall turbulent boundary layers with constant skin friction”. In: *Journal of Fluid Mechanics* 818 (2017), pp. 26–45. DOI: 10.1017/jfm.2017.132.

TABLE OF CONTENTS

LIST OF ILLUSTRATIONS

Number *Page*

LIST OF TABLES

Chapter 1

INTRODUCTION

1.1 Turbulent boundary layers

Turbulent flows are characterised by irregular, time-varying yet often distinguishable features with statistics determined by fluctuations about a mean state. An early visualisation of turbulence was presented by Reynolds in his 1883 experiments [67], broadly categorising the behaviour of pipe flow as either 'direct' (laminar) or 'sinuous' (turbulent). Often, one considers the concept of eddies, a description of structures within flows, which occupy distinct length-scales. Richardson's [68] notion is a particularly useful one when visualising the effects of turbulence - that the larger eddies eventually break up and result in the formation of smaller eddies, in an energy transfer mechanism to smaller scales that is elegantly described as the 'energy cascade'. The range of scales involved in turbulent flows through this cascade [62], from the largest inertial scales to the smallest ones dominated by viscous forces and dissipation, present interesting challenges from both experimental and numerical perspectives.

Practical flows often occur adjacent to wall boundaries and in confined geometries. Prandtl [64] introduced the concept of the boundary layer through his idea that viscous effects are confined locally to a thin wall-parallel layer adjacent to a solid body, assuming the 'no-slip' condition due to frictional effects. Boundary layer flows, given their prevalence in engineering applications such as airfoils, engines, pipe flows, ducts and channels have naturally been subject to detailed analysis and experimental studies. Significant contributions were made by von Kármán [87] and Millikan [48], through the idea of the log-law for mean velocity profiles and its associated multiplicative constant κ now named after him. Coles [20] further extended this idea by introducing the law of the wake to complete the presently accepted description of the mean velocity profiles in turbulent boundary layers, which we shall explore in the following pages.

The structure of the boundary layer moving away from the wall can be considered (in the mean sense) as follows. In the near wall region known classically as the viscous sublayer, the velocity $u^+ = \overline{u}/u_\tau$ scales linearly with z^+, the inner-scaled wall normal coordinate. The limit of this region has been shown to be around $z^+ \approx 5$

through various experimental programs. The overlap region between this viscous sublayer and the logarithmic profile identified by Kármán is known as the buffer layer, where the effect of viscosity diminishes. The log-law itself, as stated by von Kármán can be expressed as (1.1),

$$\frac{\overline{u}}{u_\tau} = \frac{1}{\kappa}\left(\ln \frac{z u_\tau}{\nu} + C\right) \tag{1.1}$$

with the friction velocity $u_\tau = \sqrt{\frac{\tau_w}{\rho}}$, z the wall normal coordinate, and a constant C which is a consequence of the specific geometry. The addition of a wake-function (1.1) in the outer part of the boundary layer [20] then completes the classical description of the turbulent boundary layer mean velocity.

$$\frac{\overline{u}}{u_\tau} = \frac{1}{\kappa}\ln\left(\frac{z u_\tau}{\nu}\right) + const. + \frac{\Pi}{\kappa} W\left(\frac{z}{\delta}\right) \tag{1.2}$$

where $W(z/\delta)$ is the wake-function, and Π, the Coles wake factor, may vary with the streamwise coordinate in non-equilibrium flows. In his 1956 manuscript, Coles also provides a physical interpretation of the law of the wake making reference to large-scale mixing processes with stronger inertial influence than viscous influence. The imposition of the no-slip wall condition then necessarily modifies the exterior of the boundary layer to what we now know as the wake-region of the boundary layer.

Logarithmic dependence of streamwise Reynolds stresses on z/δ was proposed by Townsend [86] and has been observed in experiments by Marusic and Kunkel [45] and Squire et al. [82]. Recent boundary layer experiments have provided evidence for the onset of log-law behaviour at $z^+ = 200$ [59, 56]. Boundary layers have been shown to require both inner (via the lengthscale ν/u_τ) and outer scaled (via the boundary layer thickness δ) quantities for a full description of the mean velocity and Reynolds stress $\rho u_i' u_i'$ statistics, where u_i' represent turbulent fluctuating velocity components. Key integral parameters describing the growth of a turbulent boundary layer include the displacement thickness δ^*, momentum thickness θ, skin-friction C_f and the shape-factor $H = \delta^*/\theta$. Power-law behaviour has been suggested by Barenblatt and Prostokishin [5], such that $\frac{\overline{u}}{u_\tau} = C_1\left(\frac{z u_\tau}{\nu}\right)^b$; while this question remains under investigation, there is compelling evidence through computational solutions and experiments for the log-law behaviour at high Reynolds numbers [11, 82].

Techniques such as hot-wire anemometry, particle image velocimetry, floating element balances, Preston-tube methods and oil-film interferometry have been developed to enable observations and analysis of specific parameters, length and time scales to inform detailed mathematical modeling and predictive capabilities for a range of turbulent flow conditions. The efficacy of various measurement techniques is tied to specific flow configurations. Marusic et al. [46] provide a review of key developments and questions that require careful investigation in high Re turbulence. The issue of accurate wall-shear stress measurements is identified as an important step towards enabling strong conclusions about parameter dependence at high Re. In internal flows such as pipes and channels, 'equilibrium' is said to have been achieved with streamwise invariance in the mean velocity and turbulence quantities. Marusic et al. [46] refer to the strict definition of Rotta [69], requiring invariance in streamwise quantities with respect to the local length and velocity scales; the requirement for two similarity measures in boundary layer flows (based on zu_τ/ν and z/δ) drives their suggestion for a definition of equilibrium based on the relaxation of velocity deficit in the outer region.

1.2 Roughness in engineering applications

This section provides a broad overview of roughness in practical flows, with references to key studies. A detailed discussion of rough-wall effects specific to boundary layer flows follows in chapter 2. Wall roughness effects can be deliberate and desirable, as in the use of shark-skin riblets with specific geometric parameters to reduce drag [22], or an undesirable, natural result of deterioration in engineering materials, such as that observed in piping, aerospace and naval applications. Even with advanced manufacturing techniques, it has been shown that roughness effects appear in nominally smooth wall flows at high Reynolds numbers [47]. Mckeon et al. [47] found that their pipe flow measurements did not display roughness effects until $Re_D > 13.6 \times 10^6$, where Re_D is the Reynolds number based on pipe diameter. Flows with internal and external geometries are known to behave differently compared with the canonical smooth-walled scenario under, firstly, the mere presence of roughness, and secondly the specific type of roughness involved. Turbulent flows modified by roughness are demonstrable in atmospheric and oceanic boundary layer flows, with forest canopies, urban architecture [89] and ocean-land surface topography [6] representing significant modifications to the flow from the ideal smooth surface. In many applications this represents a direct impact on operational costs [77] due to an increase in drag, providing further incentives for an improved

understanding of rough-wall turbulent flows.

Rough walls present themselves in a variety of geometries, from the classical sand-grain roughness studied by Nikuradse [57] to riblet [22], cuboidal block elements [7] and sinusoidal roughness elements [44] studied more recently. Each of these roughness geometries can be defined by various measures including, but not limited to the maximum roughness crest height, the root-mean-square value of individual peaks, or by using the Hama [29] roughness function to assign an equivalent sand-grain roughness measure k_s. Given the complexity of the roughness scales and geometries involved, the flat plate turbulent boundary layer, with allowances for roughness and modified surface finishes offers a platform using which we can study, both experimentally and numerically, the main characteristics of rough-wall flows to inform detailed modelling and predictive capabilities over more complicated boundary geometries. Rough-walled flat plate TBL with sand-grain type roughness of lengthscale k_s (as introduced by Nikuradse (1933) in his pipe-flow experiments) have been studied experimentally by Prandtl and Schlichting (1934) and in a similarity scaling analysis by Granville (1958). Jiménez [35] has identified δ/k_s as an important parameter in determining the influence of roughness on turbulent boundary layers, where δ is the boundary layer thickness and k_s is the equivalent sand-grain roughness. The wall-normal extent to which each form of roughness affects the boundary layer is then dependent on the regime (smooth, transitionally rough or asymptotically rough) in which $k_s^+ = k_s u_\tau/\nu$ and δ/k_s lie. Colebrook [19], Nikuradse [57] and Moody [52] contributed greatly to early research through experiments and empirical modeling. The Moody diagram for pipe flow friction factors [51] is one of the best known tools for characterising the roughness in a form amenable to a simple calculation of skin-friction. Modern experiments [24, 82] have generated vast datasets on the fundamental boundary layer roughness problem, and are a promising step towards developing advanced modeling techniques.

1.3 Overview of dissertation

The overarching subject of this dissertation is the computational study, using large-eddy simulations, of zero pressure gradient (ZPG) turbulent boundary layer (TBL) flows with spatially varying roughness, which represent an interesting class of problems in engineering applications. We have begun the discussion with notes on the broader topics of turbulent boundary layers and wall roughness in this introductory chapter. Rough-wall theory and existing experimental studies are reviewed in chapter 2, followed by a description in chapter 3 of the numerical methods and code used

in this dissertation. An interesting class of flows with constant skin-friction is then addressed in chapter 4 by means of semi-empirical model development and LES using the stretched vortex subgrid-scale model with wall-modeling that incorporates a term accounting for surface roughness. This is followed by a study of flat plate TBL with isotropic, spatially varying roughness in chapter 5, where non-equilibrium flows owing to transitions between smooth-rough and rough-smooth surfaces are studied using large-eddy simulations over a range of Re_τ and k_s^+. Chapter 6 then explores the effects of a static patch of roughness that extends a short distance in the streamwise direction, across the entire spanwise extent of the computational domain, on an otherwise smooth walled boundary layer flow at high Re. A final summary of the results, and concluding remarks are presented in chapter 7.

Chapter 2

BACKGROUND

2.1 Governing equations

The governing equations for flows considered in this dissertation are the incompressible ($M << 1$, M = Mach number) Navier-Stokes equations (2.1).

$$\frac{\partial u_i}{\partial t} + u_j \frac{\partial u_i}{\partial x_j} = -\frac{1}{\rho}\frac{\partial p}{\partial x_i} + \nu \frac{\partial^2 u_i}{\partial x_j^2}, \qquad \frac{\partial u_i}{\partial x_i} = 0, \tag{2.1}$$

u_i denotes the velocity field, x_i represent spatial coordinates, ν is the kinematic viscosity, ρ the density. These equations describe the conservation of mass and momentum within the flow field.

2.2 Rough-walled TBL

The theory behind the effect of wall roughness is briefly highlighted in this section as a precursor to the classification of roughness elements based on flow properties. We begin with the logarithmic velocity profile in turbulent boundary layers with a velocity deficit ΔU^+ due to roughness (2.2), as stated by Clauser [17].

$$\frac{u}{u_\tau} = \frac{1}{\kappa}\ln\left(\frac{z u_\tau}{\nu}\right) + A - \Delta U^+\left(\frac{k_s u_\tau}{\nu}\right) \tag{2.2}$$

where, for simplicity of exposition, the Coles wake function has been omitted. Here u_τ represents the friction velocity, which is related to the wall shear stress τ_w such that $\tau_w = \rho u_\tau^2$ where ρ is the density, A is a constant offset parameter. Henceforth, the application of inner scaling via u_τ/ν will be denoted by a $^+$ superscript, for example, $k_s^+ = k_s u_\tau/\nu$, where k_s is the equivalent roughness lengthscale of the 'k-type' (a discussion of this terminology follows). Studies have shown [61] the need for an offset parameter ε to capture the effect of flow displacement relative to the wall due to roughness.

$$\frac{\overline{u}}{u_\tau} = \frac{1}{\kappa}\ln\left(\frac{(z+\varepsilon) u_\tau}{\nu}\right) + A - \Delta U^+\left(\frac{k_s u_\tau}{\nu}\right) \tag{2.3}$$

Figure 2.1 presents the idea of the log-layer velocity deficit using LES mean profiles for purely smooth and purely rough-walled turbulent boundary layers. The example presented uses a virtual-wall model, which, through a slip velocity prescription based on the vorticity dynamics negates the requirement for DNS-like resolution in the near-wall region. Thus the first point demonstrated in this case is in the log-layer (the buffer layer $10 \leq z^+ \leq 100$ and the viscous sub-layer for $z^+ \lessapprox 5$ [62] are not explicitly resolved on the computational grid).

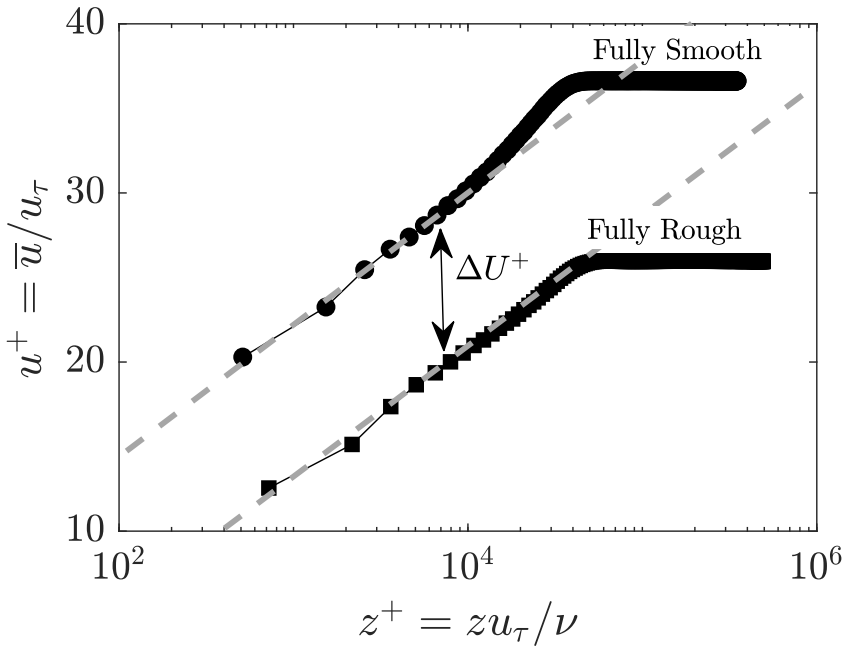

Figure 2.1: Typical inner-scaled mean velocity plots showing log-layer deficit $\Delta U^+ = f(k_s^+)$ in rough-wall flow. Annotations describe filled symbol curves. Sample data from wall-modeled LES performed as part of this dissertation. Dashed lines show log-law dependence on inner scaled wall units z^+.

In (2.2) the form of ΔU^+ is not specified. The image reproduced in figure 2.2 [35] compiles experimentally determined ΔU^+ from the hydrodynamically smooth to the fully rough regimes, and highlights that each surface type requires individual treatment if we wish to successfully model the mean-flow effects over a large range of k_s^+. A priori determination of k_s remains an interesting question, and techniques such as minimal-channel DNS [44] have been developed to allow rapid calculation of ΔU^+ and therefore a determination of k_s from the mean velocity log-layer for various roughness geometries.

Typically ΔU^+, measured from experiments, allows k_s to be calculated using the

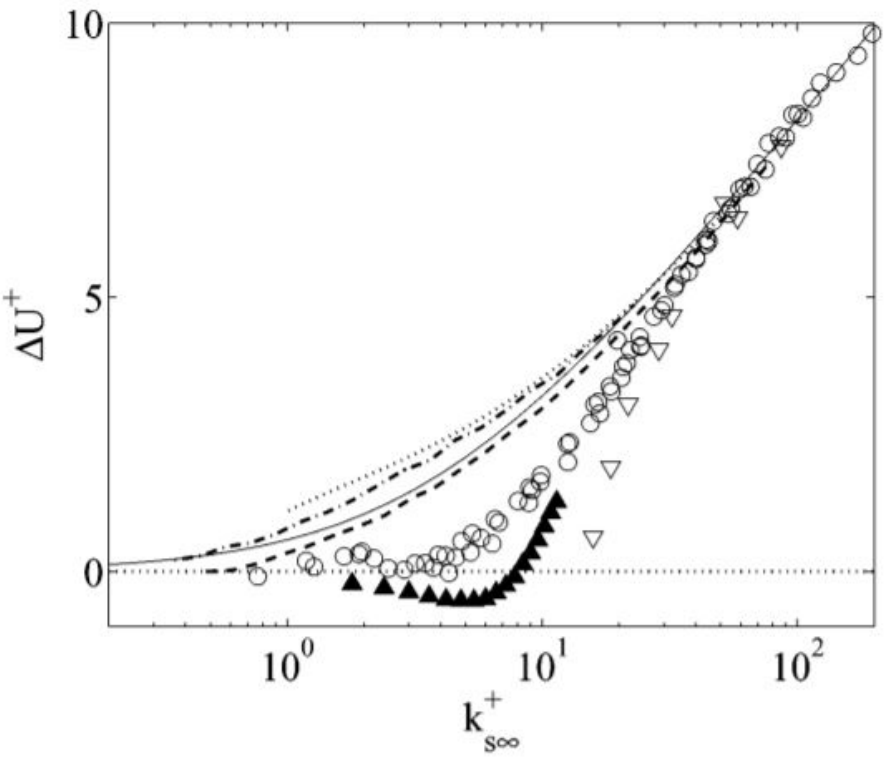

Figure 2.2: Reproduction of Figure 3 from Jiménez [35]. Log-law velocity deficit ΔU^+ as a function of $k^+_{s\infty}$, the Reynolds number based on the equivalent sand-grain roughness k_s. Symbols and broken lines represent specific types of roughness, detail in Jiménez [35]. Solid line represents Colebrook's full-range interpolation formula $\Delta U^+ = \kappa^{-1} \log(1 + 0.26 k^+_{s\infty})$

asymptotic roughness assumption; k_s is not directly tied to a geometric roughness measurement (but is representative of the roughness height k rather than the boundary layer δ)[82], and in this dissertation is used as the equivalent sand-grain roughness parameter [57]. Attempts have been made to tie k_s to measured geometric quantities - Flack and Schultz [24] identify the roughness root-mean-square height k_{rms} and skewness s_k as important measures that correlate the roughness function in the fully-developed regime, suggesting (2.4). In their study, $k^+_s > 75$ is taken as the asymptotically rough regime.

$$k_s \approx 4.43 k_{rms} (1 + s_k)^{1.37} \tag{2.4}$$

We also note the work of Simpson [79] in the development of correlations for three-dimensional roughness patterns, including the recognition that large k/δ would result in roughness effects visible across the extent of the boundary layer.

In the sense used here, we classify the sand-grain type roughness as the 'k-type' roughness as stated by Jiménez [35], such that δ/k_s is large, with $k^+ >> 1$. An alternative class of roughness perturbations is the 'd-type', and the roughness height relative to the boundary layer thickness δ is large (low δ/k_s), such that the roughness influence extends much further into the boundary layer than with k-type roughness. d-type walls consist of grooves in between individual roughness elements, where sheltering behaviour is observed such that the outer flow is isolated from the groove resulting in partial slip-wall boundary conditions [35].

Townsend's hypothesis is an important consideration in rough-walled TBL; he stated that [86] at high Re, the structure of turbulence in a boundary layer remains unaffected by the exact nature of the roughness, rather through a boundary condition effect in the viscous sublayer. The wall-normal extent of the direct influence of roughness elements is termed the roughness sublayer. Studies with 'k-type' elements have supported this hypothesis [76, 66, 78, 26], and departures from the Townsend hypothesis have been attributed to low values of δ/k_s, typically when two-dimensional roughness effects become significant. Schultz and Flack [76] studied the rough-wall boundary layer, providing evidence for Townsend's wall similarity hypothesis and concluding that with sufficient separation between the roughness scale and the largest turbulence scales, the outer layer remains unaffected except for a boundary condition prescription via δ and u_τ, the friction velocity. In terms of experiment design, Jiménez [35] suggests that experiments be conducted at $k_s^+ > 100$, with $\delta/k_s > 40$ for roughness to affect less than half the log-layer extent. Flack et. al [25] have experimentally shown that the rough element influence extends up to three times the sand-grain equivalent height, with the potential for disruption of the near-wall cycle as this value is approached.

Hama [29] showed the universality of the log wake law (2.2) through experiments on pipe, channel and zero-pressure gradient boundary layer flow. The Colebrook [19] interpolated form of the roughness function captures both transitional and fully-rough regimes, and offers a simple model amenable to practical flow problems, and in computational solutions to capture statistics in complex wall-bounded turbulence.

The specific geometry of roughness, despite resulting in the same ΔU^+ has been experimentally shown to have some effect on the turbulent parameters such as the Reynolds stresses [2]. One must therefore exact caution when applying the ΔU^+ formulation to arbitrarily complex roughness element geometries. Equilibrium flows over uniformly rough and smooth walls have been studied in great detail recently

by Squire et al. [82], who presented a detailed comparison between smooth and rough walls for $26 \leq k_s^+ \leq 155$ and $2890 \leq \delta_{99}^+ \leq 29900$. Schultz and Flack [76] considered rough-walled boundary layer flows up to $Re_\theta = U_\infty \theta/\nu = 27100$, θ being the momentum thickness, determining that ΔU^+ exhibits inflectional behaviour when plotted against k_s^+ in the case of three-dimensional Gaussian roughness.

2.3 Computational studies of turbulent boundary layers

The abundance of boundary layer flows in physical applications necessitates the development and evaluation of numerical solutions of the equations of fluid motion. Of these, Direct Numerical Simulation (DNS) provides the most accurate (and the most computationally expensive) solution to flow problems. Other methods include Reynolds Averaged Navier-Stokes (RANS), Large Eddy Simulation (LES), and hybrid RANS-LES. RANS and hybrid RANS-LES approaches are typically found in commercial applications. In the context of this dissertation, we only discuss DNS and LES in greater detail.

2.3.1 Direct Numerical Simulations (DNS)

The method offering the highest fidelity (subject to appropriate understanding and application of numerical stability issues, order of accuracy of differential equation solvers, and mesh-design) in computational results is referred to as DNS. The computational cost, in terms of the number of nodes required scales as Re_λ^6 where λ represents the Taylor lengthscale. It can be shown that the majority of modes resolved through DNS lie in the dissipative range [62], motivating the pursuit of methods which focus on the larger, more tractable scales which dominate the energy spectrum while modeling the effect of the smallest, dissipative scales. DNS has been applied to problems such as transition to turbulence [74], channel flows at low Re [38], turbulent boundary layer flow at Re_θ up to 940 [88]. Given our focus on high Re flow solutions in this dissertation, we highlight the work of Lee and Moser [41], whose DNS of channel flow at $Re_\tau = 5200$ is (as of July 2018) the highest achieved Re_τ carried out on petascale computer architectures, representing months of wall-clock time.

2.3.2 Large Eddy Simulations (LES)

LES can further be classified into wall-resolved (WRLES) and wall-modelled (WM-LES) formulations. Recent work has demonstrated the efficacy of LES in complex flow phenomena; examples include flows with transition to turbulence [75], wall-

resolved boundary layer flows with separation and re-attachment [12] and flow over grooved cylinders (WRLES) at high Reynolds numbers [10]. WMLES has been used to study high-*Re* effects in turbulent boundary layer, channel and pipe flows [16, 31, 72]. An opportunity exists to develop the capability to carry out LES in complex flow scenarios with the ultimate goal of providing a viable alternative to DNS while expanding the problem scope and minimally compromising solution accuracy. Figure 2.3 presents a visual representation of the scale interactions in turbulence using an image of storm clouds on Jupiter (retrieved from NASA APOD, 7/26/2018). We present the main idea of the presence of multiple lengthscales in turbulent flows, and schematically demonstrate the grid-requirements for LES and DNS by considering visually discernible eddy lengthscales in figure 2.3. Interactions of flows with wall boundaries introduces added complexities through vorticity generation near walls (not shown in the image).

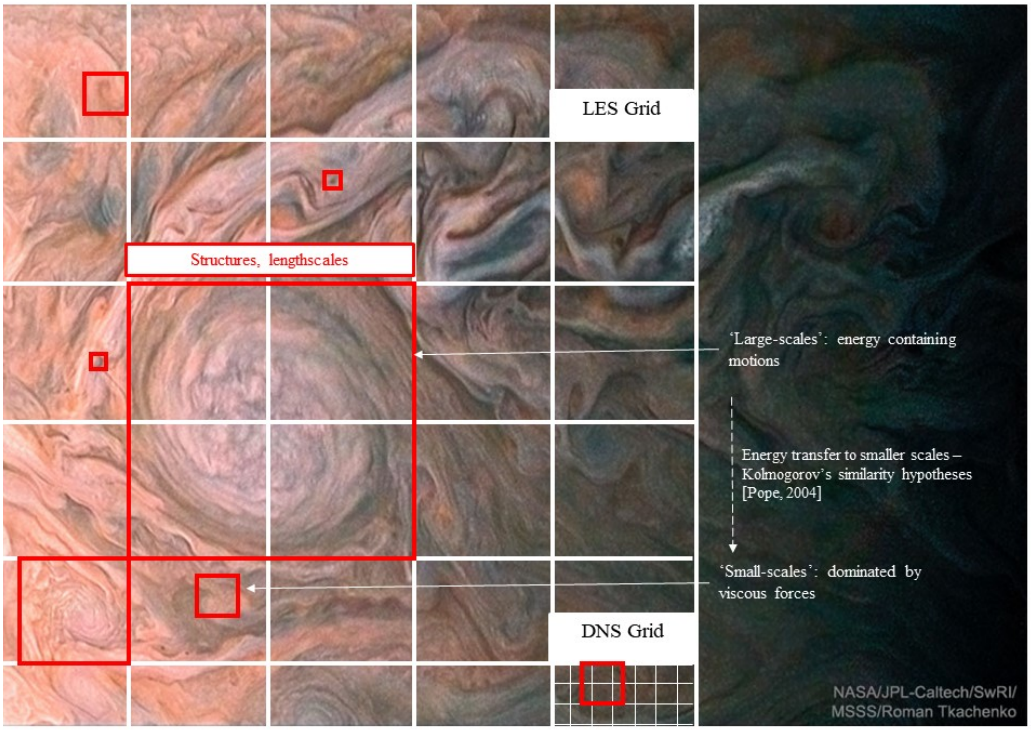

Figure 2.3: Schematic representation of turbulent scales on Jupiter storm clouds. Red boxes highlight eddies of various lengthscales. White boxes highlight examples of grids that may be used in computations. DNS resolves smaller scales, LES requires additional equations to model their effects. Image reproduced from NASA-APOD, annotated for purposes of this dissertation.

Chapter 3

SUBGRID-SCALE MODELLING AND NUMERICAL METHOD

3.1 Overview

The present LES uses the stretched vortex (SV) subgrid scale (SGS) model in the outer flow developed by Misra and Pullin [50], with extensions by Chung and Pullin [16] for smooth-walled turbulent boundary layer flows. In this model SGSs are assumed to be comprised of vortices with orientation determined by the resolved scale velocity field. The outer flow LES is coupled to the near-wall model through an ODE for the friction velocity u_τ obtained via the wall-normal integration of the wall-parallel filtered streamwise momentum equation. Information from the outer LES serves as an input to this ODE. This ODE incorporates a dynamic value for the Kármán constant, and is not restricted to a specific form of inner scaling for the unsteady terms. Detailed descriptions of the model have been compiled by Inoue and Pullin [31], Saito, Pullin, and Inoue [71], Chung [14]. The following sections discuss the numerical method, subgrid scale and wall-modelling techniques in some detail. This chapter captures the common aspects of the LES and numerical techniques applied to the flows in chapters 4, 5 and 6.

3.2 Large-eddy simulation with wall modelling

Expressing the velocity field $u_i(x, y, z, t)$ in terms of the filtered scale $\widetilde{u_i}(x, y, z, t)$ and fluctuating components $u_i'(x, y, z, t)$, such that $u_i(x, y, z, t) = \widetilde{u_i}(x, y, z, t) + u_i'(x, y, z, t)$ allows us to write the formally filtered Navier-Stokes (NS) equations

$$\frac{\partial \widetilde{u_i}}{\partial t} + \frac{\partial \widetilde{u_i}\widetilde{u_j}}{\partial x_j} = -\frac{\partial \tilde{p}}{\partial x_j} + \nu \frac{\partial^2 \widetilde{u_i}}{\partial x_j^2} - \frac{\partial T_{ij}}{\partial x_j}, \qquad \frac{\partial \widetilde{u_i}}{\partial x_i} = 0, \tag{3.1}$$

for the filtered velocity field $\widetilde{u_i}(x, y, z, t)$, where $T_{ij} \equiv \widetilde{u_i u_j} - \widetilde{u_i}\widetilde{u_j}$ is the subgrid stress tensor and where subscripted variables denote three Cartesian components in the x (streamwise), y (span-wise) and z (wall-normal) directions respectively with corresponding velocity components u, v and w. $\widetilde{(\ )}$ denotes filtered quantities as described in Chung and Pullin [16], presently viewed as a strictly formal construction. Henceforth we make the assumption that the formally filtered velocity $\tilde{u_i}$ can be identified with the resolved velocity in the LES.

3.2.1 Stretched vortex SGS model

We apply the the stretched vortex (SV) subgrid-scale (SGS) model [49, 16, 31] in the present work. This is a structure-based approach in which we assume that the subgrid turbulent motion in each cell is given by approximately axisymmetric tubes in every computational cell. The orientation of these vortices is given by the eigenvectors of the local resolved scale strain-rate tensor. Considering e^v as the vortex orientation, the subgrid stress is modelled as

$$T_{ij} = \left(\delta_{ij} - e_i^v\, e_j^v\right) K, \tag{3.2}$$

where the model for the subgrid energy, and energy spectrum, is obtained using the approach of Lundgren [43] on the stretched spiral vortex local solution to the equations of fluid motion.

$$K = \int_{k_c}^{\infty} E(k)dk, \qquad E(k) = \mathcal{K}_0 \epsilon^{2/3} k^{-5/3} \exp\left(-\frac{2k^2\nu}{3|\tilde{a}|}\right), \tag{3.3}$$

where $k_c = \pi/\Delta_c$ represents the cut-off wavenumber, $\Delta_c = \left(\Delta_x\Delta_y\Delta_z\right)^{1/3}$, it is tied to the grid spacing given by the subscripted Cartesian coordinates, and $a = \widetilde{S}_{ij}\, e_i^v\, e_j^v$ gives the projection of the resolved-scale strain-rate onto the SGS vortex direction. Integration gives

$$K = \frac{1}{2}\mathcal{K}_0'\Gamma[-\frac{1}{3}, \kappa_c^2], \qquad \Gamma[s,t] = \int_t^{\infty} u^{s-1}\exp(-u)du. \tag{3.4}$$

$\mathcal{K}_0' = \mathcal{K}_0\epsilon^{2/3}\lambda_v^{2/3}$ is a group constant obtained by matching structure functions to the local resolved-scale flow [16, 31], with $\lambda_v = (2\nu/3|\overline{a}|)^{1/2}$, and $\kappa_c = k_c\lambda_v$. In the present implementation e_i^v is aligned with the principal extensional eigenvector of $\widetilde{S}_{ij}$. The advantage of such a model is that the local cell-size is the main adjustable parameter (The model is still subject to some assumptions in its derivation).

3.3 Wall model with roughness: friction velocity u_τ

3.3.1 General discussion

In wall-resolved LES, the viscous length scale ν/u_τ is resolved or partially resolved near the wall. By "partially resolved" we mean that the viscous length scale is resolved in the wall-normal direction but may not be fully resolved in the wall-parallel directions. Wall-normal resolution usually requires the use of a stretched mesh that has higher resolution near the wall. A recent example is the work of Cheng et al. [13] who use wall-modelled LES for flow past a cylinder up to

Reynolds number Re_D based on the cylinder diameter and the free-stream velocity up to $Re_D = 8.5 \times 10^5$.

In wall-modelled LES, a specific wall model is used to represent both the effect of the wall itself and also the anisotropic character of near-wall eddies. The wall viscous scale is not resolved and in fact may be orders of magnitude smaller than the local mesh size in any co-ordinate direction. In particular the Chung & Pullin wall model introduces a "raised" virtual wall at height h_0 above the actual wall. As will be seen, in the rough-wall extension [71], the wall roughness scale, for example the sand-grain roughness scale, must be smaller than h_0. If this condition is not satisfied, the roughness would begin to be of the order of the wall-normal cell spacing, which would require specific modelling of its geometry. In this sense, the present wall model is limited by the constraint that the roughness scale must be subgrid.

We apply the virtual-wall model (VWM) [16, 31, 12] and include within it a correction that is determined by the local distribution of roughness on the wall boundary as shown by Saito, Pullin, and Inoue [71]. The key assumption used within this wall-model is the presence of near wall vortices whose size scales with distance away from the wall. Two key aspects of the VWM are highlighted here. The wall-parallel streamwise momentum equation is first combined with the assumption of inner scaling on u_τ and ν/u_τ as velocity and length scales for the near-wall subgrid, streamwise velocity. For the canonical flat plate we arrive at an ordinary differential equation (ODE) for the friction velocity $u_\tau(x, y, t) = \sqrt{\frac{\tau_w(x,y,t)}{\rho}}$ at each wall point. ODE coefficients are obtained dynamically through coupling with the outer LES at the first few wall-normal grid points. The locally determined u_τ is then combined with a log-linear approximation to a slip velocity at a raised or virtual wall plane at a specified distance h_0 from the wall. h_0 is thus a model parameter and is subgrid in the sense that $h_0 < h$, where $h \equiv \Delta z$ is first wall-normal grid position. The virtual-wall concept leads to the idea of an "interface" at $z = h_0$ between the outer LES and the wall-modelled region $z \leq h_0$. In the [16] approach the outer LES informs the wall model by supplying some information in the form of resolved-scale flow quantities and the wall model responds by supplying a slip velocity as an effective Dirichlet boundary condition for the outer LES. The two major elements of the model are an ODE to calculate u_τ and the subsequent evaluation of both a slip and a wall-normal velocity using a local wall-equilibrium based on Townsend's attached-eddy hypothesis.

The effect of h_0 on the turbulent mean velocity profiles has been explored by Chung [15], and is presently linked to the wall-normal cell size such that $h_0 = 0.18\Delta_z$. Reynolds-averaged Navier-Stokes equations are not necessary in the near-wall region with $u_\tau(x, y, t)$, and therefore $h_0^+ \equiv h_0\, \nu/u_\tau$ is calculated dynamically. Cheng, Pullin, and Samtaney [12] develop a two-dimensional wall-model and demonstrate its efficacy in the case of boundary layer flows with separation.

3.3.2 Ordinary differential equation for u_τ.

The focus of this dissertation is on attached flows, hence the one-dimensional version based on the streamwise equation of the virtual wall model is used in the numerical setup. In both wall-modelling approaches, the flow is assumed to be in local equilibrium when developing the equation for u_τ. The present development of the wall model follows the detailed derivation given by Saito, Pullin, and Inoue [71]. We denote streamwise, spanwise and wall-normal coordinates, respectively by x, y, and z while u, v, and w are the corresponding velocity components. Following Saito [70] wall-parallel filtering and wall-normal integration operators are defined by

$$\widetilde{\phi}\,(x, y, z, t) = \int\int \phi\,(x', y, z', t)\, G\,(x - x'; \Delta_c)\, G\,(y - y'; \Delta_c)\, dx' dy', \tag{3.5}$$

$$\langle\widetilde{\phi}\rangle\,(x, y) = \frac{1}{h - k\,(x, y)} \int_{k(x,y)}^{h} \widetilde{\phi}\,(x, y, z)\; dz, \tag{3.6}$$

where $\widetilde{\phi}$ denotes wall-parallel filtering and $\langle\phi\rangle$ denotes a wall-normal average, and Δ_c is the filter cutoff length given by the SGS model.

We now obtain the ODE for the friction velocity u_τ. Let the wall shape be $y = k(x, z)$ with $\overline{k(x, y)} = 0$ and define $f(x, y) \equiv k(x, y) - z$. The object $\overline{(\ )}$ represents a filtering with some length scale (of order the wall-parallel grid size) over the wall-parallel plane. We denote the wall-normal (into the wall) by $\boldsymbol{n} = \nabla f/|\nabla f|$ on $f = 0$. Attention is now focused on a small control volume at the channel wall with x, y dimensions given by the local wall-parallel grid sizes Δx, Δy (the local grid size), and wall-normal dimension of scale h, which at this stage is arbitrary. The subgrid roughness assumption is that all scales Δx, Δy and h are much larger than the maximum roughness scale which can be taken as $max|k(x, y)|$. Of the control surface that surrounds the control volume, four wall-normal surfaces intersect the wall while the wall itself is the bottom surface. We now apply top-hat filtering in the wall-normal direction and averaging as defined above to the streamwise momentum

equation to give an integral form over the control volume

$$\frac{\partial}{\partial t}\iiint \boldsymbol{u}\, dV = -\oiint \boldsymbol{n}.\left(\boldsymbol{u}\,\boldsymbol{u} + \frac{p}{\rho}\boldsymbol{I} - \frac{\boldsymbol{\tau}}{\rho}\right) dS, \tag{3.7}$$

where $\boldsymbol{\tau} = 2\nu\boldsymbol{S}$ and $\boldsymbol{S}$ is the strain-rate tensor. In (3.7) the right-hand side is the momentum flux through the planes defining the control volume. The exterior forces are pressure, and viscous terms.

For a non-planar wall the wall pressure contribution is finite. Since the roughness is subgrid with unknown detailed shape, then both the integrated pressure and viscous terms are generally unknown at the level of wall-modeling. We proceed by aggregating all flux contributions, including unknown terms, and interpret flux differences between parallel wall-normal surfaces by using wall-parallel derivatives. This then gives, for the cell-averaged streamwise momentum equation

$$\frac{\partial\langle\widetilde{u}\rangle}{\partial t} + \frac{\partial\langle\widetilde{uu}\rangle}{\partial x} + \frac{\partial\langle\widetilde{uv}\rangle}{\partial y} + \frac{1}{h}\widetilde{uw}|_h = -\left.\frac{\partial\widetilde{p}/\rho}{\partial x}\right|_h + \left.\frac{\nu}{h}\frac{\partial\widetilde{u}}{\partial z}\right|_h - \frac{1}{h}\left[\frac{1}{\Delta x\,\Delta y}\iint_w \frac{p}{\rho}\,n_x\,dS - \frac{\nu}{\Delta x\,\Delta y}\iint_w \boldsymbol{n}.\nabla\boldsymbol{u}\,dS\right]. \tag{3.8}$$

In this equation, the streamwise component of the wall normal unit vector is n_x and $\iint_w$ denotes an integral over the wall. The unknown pressure and viscous terms due to roughness are now characterised by the definition of the wall- friction velocity u_τ

$$u_\tau^2 = \frac{1}{\Delta x\,\Delta y}\iint_w \frac{p}{\rho}\,n_x\,dS - \frac{\nu}{\Delta x\,\Delta y}\iint_w \boldsymbol{n}.\nabla\boldsymbol{u}\,dS = \frac{1}{\rho}\overline{\tau_w}, \tag{3.9}$$

where $\overline{\tau_w}$ is now the total surface drag force per unit projected area and $\overline{(\,)}$ now refers to an average over the intersection of the control volume (cell) and the wall. Equation (3.8) can now be written as

$$\frac{\partial\langle\widetilde{u}\rangle}{\partial t} + \frac{\partial\langle\widetilde{uu}\rangle}{\partial x} + \frac{\partial\langle\widetilde{uv}\rangle}{\partial y} + \frac{1}{h}\widetilde{uw}|_h = -\left.\frac{1}{\rho}\frac{\partial\widetilde{p}}{\partial x}\right|_h + \left.\frac{\nu}{h}\frac{\partial\widetilde{u}}{\partial z}\right|_h - \frac{1}{h}u_\tau^2. \tag{3.10}$$

It is recognised that $\overline{\tau_w}$ contains both pressure and viscous contributions and so represents a pressure-viscous force per unit area rather than a pure viscous force as for the smooth-wall case. The smooth-wall case is recovered with $k(x, y) \equiv 0$ and $\boldsymbol{n} = (0, 1, 0)$.

3.3.3 Inner scaling ansatz

Following [16] the unsteady term in Equation (3.10) is now treated with a general form of inner scaling combined with an empirical roughness correction to represent the additional momentum deficit, and increased surface drag, produced by the roughness elements. This downward shift is presently modelled using a general roughness function ΔU^+. This can be included in the inner-scaling ansatz as

$$\widetilde{u}(x, y, z, t) = u_\tau(x, y, t) \left(F_1 \left(z^+ \right) - \Delta U^+ \left(k_s^+ \right) \right), \tag{3.11}$$

where $z^+ = z\, u_\tau/\nu$ and $k_s^+ = u_\tau k_s/\nu$. In (3.11), $F_1\left(z^+\right)$ appears for smooth and rough walls, whilst $\Delta U^+\left(k_s^+\right)$ is the roughness correction function expressed in terms of an equivalent sand roughness, k_s and $k_s^+ \equiv k_s\, u_\tau/\nu$. Using this and now applying a the wall-normal average we obtain

$$\frac{\partial}{\partial t}\langle\tilde{u}\rangle = \frac{d}{dt}\left(\frac{u_\tau}{h} \int_0^h \left[F_1 \left(z^+ \right) - \Delta U^+ \left(k_s^+ \right) \right] \, dz \right) \tag{3.12}$$

Here $u_\tau = u_\tau\left(x, z, t\right)$ and so varies both temporally and from point-to-point across the wall. Differentiating (3.11) with respect to u_τ then gives

$$\frac{\partial \tilde{u}}{\partial u_\tau} = F_1(z^+) + z^+ F_1'(z^+) - \Delta U^+ \left(k_s^+\right) - k_s^+ \Delta U'^+ \left(k_s^+\right) = \frac{d(z^+ F)}{dz^+} - \frac{d(k_s^+ \Delta U^+)}{dk_s^+}. \tag{3.13}$$

Appling wall-normal averaging as defined by (3.6) then leads to

$$\frac{\partial \langle\tilde{u}\rangle}{\partial u_\tau} = \frac{\tilde{u}|_h}{u_\tau} - k_s^+ \frac{\partial \Delta U^+}{\partial k_s^+}. \tag{3.14}$$

Where $\tilde{u}|_h$ is interpreted as the right-hand side of (3.11). Subsequently this will be replaced or identified with the streamwise velocity obtained from the LES at the first grid point away from the wall. Equation (3.12) can then be written in the form

$$\frac{\partial}{\partial t}\langle\tilde{u}\rangle = \frac{\partial \langle\tilde{u}\rangle}{\partial u_\tau}\frac{\partial u_\tau}{\partial t} = \frac{\partial u_\tau}{\partial t}\left(\frac{\tilde{u}\,|_h}{u_\tau} - k_s^+ \frac{\partial \Delta U^+}{\partial k_s^+} \right). \tag{3.15}$$

We remark that (3.15) follows from (3.11) - (3.12) for arbitrary $F_1(z^+)$ and $\Delta U^+(k_s^+)$. It is particularly useful that integrals of $F_1(z^+)$ do not appear in equation (3.15) owing to cancellation. Hence, perhaps surprisingly, this function need not be known in detail for the operation of the wall model.

We can now obtain an ordinary differential equation (ODE) for u_τ at each wall grid-point by substituting (3.15) into (3.10) and by making a simple approximation

of the filtered-averaged nonlinear terms as values at $y = h$ (one-point estimates). This gives

$$\frac{du_\tau}{dt} = \frac{-\left.\frac{\partial \widetilde{uu}}{\partial x}\right|_h - \left.\frac{\partial \widetilde{uv}}{\partial y}\right|_h - \left.\frac{\partial \widetilde{P}}{\partial x}\right|_h - \frac{1}{h}\widetilde{uw}\,|_h + \frac{\nu}{h}\left.\frac{\partial \widetilde{u}}{\partial z}\right|_h - \frac{1}{h}u_\tau^2}{\frac{\widetilde{u}\,|_h}{u_\tau} - k_s^+ \frac{\partial \Delta U^+}{\partial k_s^+}}. \tag{3.16}$$

The wall-normal height h is arbitrary. Previous experience ([16, 70, 13]) indicates that a good choice for h should correspond to the first or second grid cell of the LES domain. Surface roughness appears in (3.16) as the derivative of ΔU^+ with respect to k_s^+. Note that since u_τ is dynamic then both k_s^+ and this derivative will also be a dynamic part of the right-hand side of the ODE. We also remark that (3.16) can be used for boundary layer flows in the presence of pressure gradient (the present focus is still on the zero pressure gradient case). As pointed out by Saito, Pullin, and Inoue [71] (3.16) can in principle be extended to two wall-parallel co-ordinates and also to wall curvature effects. Generalisation to arbitrary roughness functions with multiple scales and horizontal distributions $\Delta U^+(k_s^{+(1)}, k_s^{+(2)}, k_s^{+(3)}, ...)$ is also possible.

3.3.4 Slip velocity at a virtual wall

A summary of the derivation of the slip velocity is given by Inoue & Pullin [31]. This is not given presently in detail. But the main idea is to utilize the attached-eddy hypothesis by assuming that in the wall-modeled region $0 \leq z \leq h_0$, the near-wall eddies are attached and almost parallel to the wall, while in the outer LES the eddies are detached and have no knowledge of the wall save for the effect of u_τ as incorporated in the slip velocity at $y = h_0$. For smooth walls this gives a log-relation for the slip velocity above smooth walls as

$$\widetilde{u} = u_\tau \left(\frac{1}{\mathcal{K}_1} \log\left(z^+\right) + A \right), \tag{3.17}$$

where

$$\mathcal{K}_1 = -\frac{\gamma_{II}\, K^{1/2}}{2\,(-T_{xz})}, \tag{3.18}$$

is a dynamically calculated von Kármán "constant". In (3.18), T_{xz} is an estimate of the Reynolds stress obtained from the outer LES at the first grid point and the vertical momentum mixing constant is given by $\gamma_{II} = 0.45$ has been calculated by matching model Reynolds stresses from both the outer LES and the wall-modelled region at $z = h_0$ using the Townsend attached-eddy model [16]. The quantity K is a measure

of the local subgrid turbulent kinetic energy obtained from the stretched-vortex model as described above. This can be extended to rough surfaces by incorporation of the roughness correction $\Delta U^+ \left(k_s^+\right)$. This leads to the model profile in the overlap layer above rough surfaces as

$$\widetilde{u} = u_\tau \left(\frac{1}{\mathcal{K}_1} \log\left(z^+\right) + A - \Delta U^+ \left(k_s^+\right) \right). \tag{3.19}$$

Equation (3.19) is now used to calculate a slip-velocity boundary condition at the flat, lifted virtual wall at $h_0 > k(x, z)$. This requires that the roughness be subgrid. The slip velocity can then be expressed as

$$\widetilde{u}\,|_{h_0} = u_\tau \left(\frac{1}{\mathcal{K}_1} \log\left(h_0^+\right) + A - \Delta U^+ \left(k_s^+\right) \right), \tag{3.20}$$

Typically, the height of the virtual wall h_0 is determined as some fraction of the first grid size, and presently $h_0 = 0.18\Delta_y$ is used following [16].

To implement the wall model, (3.16) is solved for u_τ. Then the log-relation in Equation (3.20) is used to obtain the slip velocity at the lifted virtual wall at $y = h_0$. Coupling with the outer LES occurs because some terms (3.16), as well as the shear stress T_{xy} needed for evaluating $\mathcal{K}_1$, are supplied by the outer LES. In turn the wall model supplies the slip velocity for the outer LES. Any roughness type for which a model of $\Delta U^+(k_s^+)$ is known can be incorporated.

3.3.5 Wall-normal velocity boundary condition

We have yet to discuss the wall-normal velocity at the lifted wall. The filtered continuity equation is

$$\frac{\partial \tilde{u}}{\partial x} + \frac{\partial \tilde{v}}{\partial y} + \frac{\partial \tilde{w}}{\partial z} = 0. \tag{3.21}$$

Integrating (3.21) in $0 - h_0$ and assuming zero filtered span-wise velocity gives the wall-normal velocity as

$$\widetilde{w}\,|_{h_0} = -h_0 \frac{\partial \langle \tilde{u} \rangle}{\partial x}. \tag{3.22}$$

Again using an inner-scaling argument for the derivative leads to the wall-normal velocity boundary condition,

$$\widetilde{w}\,|_{h_0} = -h_0 \frac{\partial u_\tau}{\partial x} \left(\frac{\tilde{u}\,|_{h_0}}{u_\tau} - k_s^+ \frac{\partial \Delta U^+}{\partial k_s^+} \right). \tag{3.23}$$

3.3.6 Example of roughness function

Jiménez [35] gives an extensive discussion of roughness functions for various surfaces. A particular ΔU^+ will generally be determined by the specific surface type through either theory, experiment or perhaps DNS at moderate Reynolds number. It is considered an input to the present wall model. As a specific example that will be used in the present work, we discuss briefly the Colebrook empirical formula that spans smooth walls ($k_s^+ \leq 5$) through the roughness transition regime to the fully rough limit $k_s^+ > 100$

$$\Delta U^+ \quad = \quad \frac{1}{\mathcal{K}_1} \log\left(1 + \beta\, k_s^+\right). \tag{3.24}$$

where β is a defined constant. Equation (3.16) then becomes

$$k_s^+ \frac{\partial \Delta U^+}{\partial k_s^+} = \frac{1}{\mathcal{K}_1} \frac{\beta\, k_s^+}{1 + \beta\, k_s^+}, \tag{3.25}$$

while (3.20) is then

$$\widetilde{u}\,|_{h_0} = u_\tau \left(\frac{1}{\mathcal{K}_1} \log\left(h_0^+\right) + A - \frac{1}{\mathcal{K}_1} \log\left(1 + \beta\, k_s^+\right) \right). \tag{3.26}$$

It will be evident from the above discussion and development that the present wall model effectively assumes that, in the wall-modelled region, the flow is in a state of local equilibrium with the wall state be this either smooth or rough. In the present applications, this will constitute a rather thin slab of order $0.5 \sim 1\%$ of the local boundary-layer thickness δ_{99} (the exact value varies with grid resolution). The use of Townsend's hypothesis is an essential statement that the wall surface state is communicated to the outer flow through the friction velocity. However there is two-way inner-outer coupling in the sense that the outer LES information also affects the local wall state in determining u_τ.

Due to the local, dynamic nature of the present wall model, u_τ is a spatially and temporally varying function. Consequently, both k_s^+ and thus $\Delta U^+(k_s^+)$ also vary spatially and temporally on the wall. In referring to LES results that follow, we use the notation $\overline{u}_\tau$ to refer to either time or spatially averaged values but, for simplicity, redefine $u^+ = u/\overline{u}_\tau$, $U_\infty^+ = U_\infty/\overline{u}_\tau$.

The inclusion of the wall-model with a roughness correction $\Delta U^+[k_s^+]$ only modifies the near-wall behaviour, and the outer LES, coupled through the ODE for u_τ in the wall-model, is modified only through interaction with the modelled inner dynamics. This is consistent with the notion of outer flow modification due to changes in boundary condition through the inclusion of surface roughness in a physical sense.

3.3.7 Details of the numerical method

The numerical method implemented for LES of boundary-layer flow in this dissertation is described in detail in publications [31, 12, 83], with key aspects presented here. The discrete form of the Navier Stokes equations (incompressible) are given as follows,

$$\frac{\mathbf{u}^{n+1}-\mathbf{u}^{n}}{dt} = -\mathbf{G}p - \left(\frac{3}{2}\mathbf{N}\mathbf{u}^{n} - \frac{1}{2}\mathbf{N}\mathbf{u}^{n-1}\right) + \frac{1}{2Re}\left(\mathbf{L}\mathbf{u}^{n+1} + b_1^{n+1} + \mathbf{L}\mathbf{u}^{n} + b_1^{n}\right) \quad (3.27)$$

with the discretised divergence free condition given by

$$\mathbf{D}\mathbf{u}^{n+1} = b_2^{n+1} \quad (3.28)$$

In (3.27) and (3.28), $\mathbf{N}$ represents the convective operator, $\mathbf{D}$ is the divergence operator, $\mathbf{L}$ is the Laplacian operator, $\mathbf{G}$ is the gradient operator, b_1 and b_2 represent the boundary condition vectors for the momentum equation and divergence-free equations respectively, $\mathbf{u}$ is the discretised velocity field. We can define an operator $\mathbf{A}$ to implicitly represent the advection-diffusion component of the momentum conservation equation. The specific form of $\mathbf{A}$ is tied to the numerical approximation in the time-stepping, and discussed shortly hereafter. A three-stage low-storage Runge-Kutta method [81] is used to integrate (3.1) and (3.16) in time with the inclusion of the fractional-step method [60] at each stage. We summarise the equations of this temporal scheme specific to the present implementation here,

$$\mathbf{A}\mathbf{u}*^{n+1} = \mathbf{r}^{n} + \beta_n b_1, \quad \mathbf{A} = \mathbf{I} - \frac{\beta_n dt}{Re}\mathbf{L} \quad (3.29)$$

$$dt(\alpha_n + \beta_n)\mathbf{D}\mathbf{G}p = (\mathbf{D}\mathbf{u}*^{n+1} + b_2) \quad (3.30)$$

$$\mathbf{u}^{n+1} = \mathbf{u}*^{n+1} - dt(\alpha_n + \beta_n)\mathbf{G}p \quad (3.31)$$

$$\mathbf{r}^{n} = dt\Big[-\gamma_n\mathbf{N}\mathbf{u}^{n} - \zeta_n\mathbf{N}\mathbf{u}^{n-1} + \alpha_n(\mathbf{L}\mathbf{u}^{n} + b_1^{n})\Big] \quad (3.32)$$

Constants $\alpha_n, \beta_n, \gamma_n, \zeta_n$ for $n = 0, 1, 2$ are detailed in Spalart, Moser, and Rogers [81], and we do not list them here for brevity. The formulation presented in (3.29)-(3.32) serve as an approximate solution of the matrix-vector (LU diagonalised) form of (3.27). By treating the wall-normal viscous term implicitly, we obtain a modified Helmholtz equation for the velocity update together with a pressure Poisson equation followed by the velocity correction step [31]. Solving the pressure Poisson equation facilitates the projection of the intermediate velocity field (which is not necessarily

divergence free) onto a divergence-free field while keeping its vorticity constant. The time step is constrained by the CFL number, with the maximum allowable value determined by the velocity field such that $\max(|u|/\Delta_x, |v|/\Delta_y, |w|/\Delta_z)dt \leq 1$.

For spatial discretisation, a fourth-order accurate finite-difference scheme is utilised in the x and z-directions while Fourier-series expansions of the velocity and pressure terms are employed in the y-direction, since we assume spanwise periodic flow. A staggered grid is used, following the scheme of Morinishi et al. [53] in the streamwise/wall-normal $(x-z)$ plane where the (u, w) velocity components are stored at the centers of (x, z) cell faces with cell-centered storage in the y direction.. The skew-symmetric form of convective terms is utilised to improve energy conservation and de-aliasing behaviour. To ensure the usage of a consistent stencil in the interior, ghost points are utilised in the exterior of the domain (in the non-periodic directions of the flow), with boundary conditions in the v and uv terms determined by the discretised continuity and momentum conservation conditions respectively. The Poisson equation for pressure reduces to a sequence of one-dimensional equations in the wall-normal z-direction through a combination of spectral representation in the spanwise y coordinate with a fast-cosine transform in x (hence we term this framework a pseudo-spectral code). The overall numerical method has been validated using low Re_θ direct numerical simulations [31] of the turbulent boundary layer.

The base flow is span-wise (y) periodic, has a prescribed velocity w_{top} derived from the zero-vorticity condition with an inviscid outer flow at the upper boundary of the computational domain and a convective boundary condition at the streamwise exit plane as follows,

$$w_{top} = U_\infty \frac{d\delta^*}{dx}, \qquad \frac{\partial \mathbf{u}}{\partial t} = U_c(z)\frac{\partial \mathbf{u}}{\partial x}, \tag{3.33}$$

where $U_c(z)$ is the mean streamwise exit velocity and the displacement thickness is given by

$$\delta^* = \int_0^{L_z} \left(1 - \frac{u}{U_\infty}\right) dz \tag{3.34}$$

The value $d\delta^*/dx$ is represented by a single streamwise average [31]. A turbulent initial condition is used, and turbulent flow is sustained through an inflow condition generated by a recycling method specific to the domain formulation, but based on the work of Lund, Wu, and Squires [42], and described in greater detail in chapters 4 and 5.

Chapter 4

SEMI-EMPIRICAL MODEL FOR TBL WITH LINEAR VARIATION IN SURFACE ROUGHNESS

This chapter includes results and discussions adapted from

[1] A. Sridhar, D. I. Pullin, and W. Cheng. "Rough-wall turbulent boundary layers with constant skin friction". In: *Journal of Fluid Mechanics* 818 (2017), pp. 26–45. DOI: 10.1017/jfm.2017.132.

4.1 Overview

In this chapter, we examine an interesting class of turbulent boundary layer flows with constant skin-friction. In adhering to the overall theme of this dissertation, we identify, based on previous experimental data [37] and similarity analysis [85], a class of equilibrium turbulent boundary layer flows which occur when the wall comprises of a linearly increasing equivalent sand-grain roughness measure k_s. Skin-friction typically represents an important metric in engineering analyses and practical applications, and it is therefore of interest to examine these flows in greater detail. We focus on zero pressure gradient flows in this chapter, but briefly comment on the results for Falkner-Skan and sink flows.

4.2 Background

Turbulent wall-bounded flows with streamwise constant skin-friction coefficient C_f comprise an interesting class of turbulent flows with mean-flow self-similarity. Examples for internal flows are turbulent pipe flow and open channel flow that exhibit streamwise statistical invariance. For fully developed turbulent flow in a pipe of diameter D with statistically uniform sand-grain type surface roughness whose length scale k_s satisfies $k_s/D << 1$ and where $k_s^+ \equiv k_s\, u_\tau/\nu$ is sufficiently large, the experiments of Nikuradse [57] showed that the average wall-friction coefficient $C_f = 2\,\overline{\tau}_w/(\rho\, u_b^2)$, ($\overline{\tau}_w$ is the average wall shear stress and u_b the bulk flow speed) becomes independent of Reynolds number $Re_b \equiv u_b\, D/\nu$ when this is sufficiently large, and depends only on k_s/D. This is referred to as the "fully-rough" regime (see Jiménez [35] for a discussion) where the dominant near-wall physics length

scale is k_s rather than the viscous scale ν/u_τ, where $u_\tau^2 = \tau_w/\rho$ is the square of the wall friction velocity. Using a roughness correction suggested by Colebrook [19], Moody [52] developed an empirical characterisation of $C_f(Re_b, k_s/D)$ known as the Moody diagram that covered part of the transitionally-rough regime (where both Re_b and k_s/D effects are present), and the fully-rough regime.

The flow of a zero-pressure-gradient turbulent boundary layer (ZPGTBL) at large Reynolds number over a plate covered with sand-grain type roughness of streamwise constant k_s was considered by Prandtl and Schlichting [65] and Granville [28]. For a plate of length L, when $Re_L = U_\infty L/\nu$ becomes large, Granville developed a model showing that if $k_s/L << 1$ is held constant, then the total steam-wise-integrated frictional drag coefficient C_D becomes independent of Re_L at sufficiently large values and depends only on k_s/L. Here the local skin-friction coefficient $C_f(Re_L, k_s/L, x/L)$ also becomes independent of Re_L but is not streamwise constant.

A class of boundary-layer flows with spatially constant skin-friction coefficient was discussed by Rotta [69] who gave quantitative arguments for the hypothesis that, for the ratio of the local outer flow speed to the skin-friction velocity to be spatially invariant, surface roughness whose sand-grain-type scale k_s varies linearly with streamwise distance must be present. Specific parameterisations or calculations were not provided. Kameda et al. [37] measured the wall skin friction for a flat-plate boundary layer over a wall in the presence of a two-dimensional k-type roughness with length scale that varied linearly with distance x from the leading edge. They observed that U_∞^+ was nearly constant in x and that the layer thickness increased linearly with x. This idea was developed further by Talluru et al. [85] who used a self-preserving analysis based on the equations of motion to argue that the data of Kameda et al. [37] support self-similarity of the ZPGTBL when $k_s \sim x$.

In this chapter we first develop a simple semi-empirical model for high Reynolds number turbulent boundary-layer flows with streamwise spatially-varying, nominally sand-grain-type surface roughness in the presence of an outer flow whose velocity varies as $U_\infty = P\, x^m$ where P is a dimensional constant. The model makes use of the log-wake law with assumed streamwise constant parameters combined with a fully-rough representation of the streamwise velocity roughness correction, and further utilises the von Kármán boundary-layer integral equation under the assumption that all terms are constant in the streamwise direction. This shows that k_s proportional to streamwise distance x is required for closed, self-similar solutions. Several cases of interest are discussed and comparisons with the results of Kameda et al.

[37] are made. The main focus is the zero-pressure gradient turbulent boundary layer. Large-eddy simulations (LES) of this flow using a wall-model with linearly-varying streamwise roughness are presented. The LES utilises the stretched-vortex subgrid-scale model of Misra and Pullin [49] combined with the virtual-wall model (VWM) [16, 31] for high-Reynolds number turbulent flow that incorporates modeled subgrid wall roughness [71]. It is found that, at sufficiently large Reynolds number, $U_\infty^+ = U_\infty/u_\tau$ becomes independent of Re_x and depends only on the dimensionless parameter α that characterises the roughness growth. Comparisons of LES results with model predictions are discussed.

4.3 Flows with linear roughness

4.3.1 Mean velocity profile

We consider turbulent boundary layers with power-law wall-roughness $k_s = K\,x^n$ where k_s is the local surface roughness height at the streamwise co-ordinate x with an origin such that both k_s and all measures of the boundary layer thickness are zero at $x = 0$. The length-scale of streamwise roughness variation is $K^{1/(1-n)}$. A Reynolds number $Re_x \equiv U_\infty(x)\,x/\nu$ is considered sufficiently large that flow is fully turbulent. It is assumed that the velocity profile within the boundary layer at any streamwise station is given by the classical log-wake relationship

$$\frac{u(z)}{u_\tau} = \frac{1}{\kappa}\left(\log\left(\frac{(z+\varepsilon)\,u_\tau}{\nu}\right) + \Pi\,W\left(\frac{z}{\delta}\right)\right) - \Delta U^+\left(\frac{k_s\,u_\tau}{\nu}\right) + A, \tag{4.1}$$

where κ is the Kármán constant, z a suitably defined wall-normal distance, A an offset constant, W the wake function with $W(1) = 2$ [20], Π the Coles wake factor and ε a roughness offset parameter. The latter is often used to account for an overall wall-normal shift of the logarithmic region in the presence of wall roughness: see Squire et al. [82] for discussion. It is expected that $\varepsilon = O(k_s)$. In the LES to be described, first, the roughness is considered subgrid with k_s smaller than the near-wall cell size, and second, we will mainly consider flows for which $\delta/k_s >> 1$. Hence this correction is presently neglected by taking $\varepsilon = 0$.

In (4.1) $\Delta U^+(k_s^+)$ is a roughness function that quantifies the effect of surface roughness on the mean velocity profile. Various forms of $\Delta U^+(k_s^+)$ are discussed in Jiménez [35]. An implicit present assumption is that the streamwise variation of $\Delta U(k_s^+)$ is sufficiently slow that the developing boundary layer can adjust to local roughness conditions. We assume a standard form for fully rough conditions

$$\Delta U^+(k_s^+) = \frac{1}{\kappa}\,\log\left(k_s^+\right) + A - B, \tag{4.2}$$

where $k_s^+ = k_s\, u_\tau/\nu$, where $B \approx 8.5$ is a constant. In (4.2) k_s is to be interpreted as the equivalent sand-grain roughness of the surface in the sense of Nikuradse [57]. This gives

$$\frac{u(z)}{u_\tau} = \begin{cases} \frac{1}{\kappa}\left(\log\left(\frac{z}{k_s}\right) + \Pi\, W\left(\frac{z}{\delta}\right)\right) + B, & z < \delta, \\ \\ \frac{U_\infty}{u_\tau}, & z > \delta, \end{cases} \tag{4.3}$$

where the length scale δ is defined such that

$$U_\infty^+ \equiv \frac{U_\infty}{u_\tau} = \frac{1}{\kappa}\left(\log\left(\frac{\delta}{k_s}\right) + 2\,\Pi\right) + B. \tag{4.4}$$

We utilize a simple model for the wake function [63].

$$W\left(\frac{z}{\delta}\right) = 2\,\sin^2\left(\frac{\pi\, z}{2\,\delta}\right). \tag{4.5}$$

The displacement thickness δ^* and the momentum thickness θ can now be obtained as

$$\begin{aligned} \delta^* &= \int_0^\delta \left(1 - \frac{u}{U_\infty}\right) dz, \\ &= \delta\, \frac{1 + \Pi}{\kappa\, B + 2\,\Pi + \log(\delta/k_s)}, \end{aligned} \tag{4.6}$$

$$\begin{aligned} \theta &= \int_0^\delta \frac{u}{U_\infty}\left(1 - \frac{u}{U_\infty}\right) dz, \\ &= \delta\, \frac{\Pi^2 - 4 + 2\,\kappa\, B\,(1 + \Pi) + 2\,(1 + \Pi)\,\log(\delta/k_s) - 4\,\Pi\, Q/\pi}{2\,(\kappa\, B + 2\,\Pi + \log(\delta/k_s))^2}, \end{aligned} \tag{4.7}$$

where

$$Q = Si(\pi) \equiv \int_0^\pi \frac{\sin z}{z}\, dz = 1.85194. \tag{4.8}$$

In both (4.6) and (4.7) the log-wake profile is used down to $z = 0$. This gives integrable singularities at $z = 0$. Since at large Reynolds number with $\delta >> k_s$, the roughness sub-layer can be expected to make negligible contributions to the overall mass and momentum transport across the boundary layer, the error incurred is small while the analytical simplification is substantial. Also, it can be seen in (4.6) and (4.7) that both δ^* and θ show a nonlinear dependence on Π. The possible dependence of Π on surface roughness conditions has been discussed in the literature [40, 37].

In the following model it will be required that Π be streamwise constant and so this approximation will be used subsequently.

The Rotta-Clauser parameter, sometimes used as a measure of the outer scale of the boundary layer is defined as $\Delta \equiv U_\infty^+ \delta^*$. Using (4.4) and (4.6) it follows that

$$\frac{\Delta}{\delta} = \frac{1+\Pi}{\kappa}. \tag{4.9}$$

This is independent of the following model development.

4.3.2 Two-parameter model

The Kármán integral relation can be written as

$$\frac{d\,\theta}{d\,x} = \left(\frac{u_\tau}{U_\infty}\right)^2 - \frac{\theta}{U_\infty}\,\frac{dU_\infty}{dx}\,\left(2 + \frac{\delta^*}{\theta}\right), \tag{4.10}$$

where $U_\infty = U_\infty(x)$, $u_\tau = u_\tau(x)$. We now consider conditions under which all terms of (4.10) are constant. This immediately implies that u_τ/U_∞ is independent of x, and that $\theta \sim x$. It then follows from (4.4) that δ/k_s is independent of x and so $\delta \sim k_s(x)$. If it is assumed that all of κ, B, Π are independent of x, then, since $\theta \sim x$, it follows from (4.6) and (4.7) that both $\delta \sim x$ and $\delta^* \sim x$. Since $\delta \sim k_s(x)$ then the only possibility is $k_s \sim x$ in agreement with Rotta [69], Kameda et al. [37], and Talluru et al. [85] for the zero-pressure gradient boundary layer where U_∞ is constant. Since $n = 1$ then the flow does not contain a finite length scale associated with the streamwise variation of roughness and, at large Re_x, is therefore fully self similar with similarity variable proportional to z/x. Hence we put

$$k_s = \alpha\, x, \tag{4.11}$$

where α is a dimensionless constant. For power law outer velocity profiles $U_\infty = P\,x^m$ where P is a dimensional constant it can now be seen that the second term on the right-side of (4.10) is constant for arbitrary m.

Next we put $\delta = \epsilon\, x$, where ϵ is to be determined. Hence $\delta/k_s = \epsilon/\alpha$. Substituting (4.4), (4.6) and (4.7) into (4.10) and simplifying then gives

$$\begin{aligned} -2\,\kappa^2\,\pi + \epsilon\,(-4 - 8\,m + 2\,B\,\kappa\,(1+3m)(1+\Pi) + \Pi(\Pi + m\,(4+6\,\Pi)))\,\pi \\ - 4\,\epsilon\,(1+2m)\,\Pi\,Q + 2\,\epsilon\,(1+3m)(1+\Pi)\,\pi\,\log(\epsilon/\alpha) = 0. \end{aligned} \tag{4.12}$$

The above can be summarised as follows: We fix κ, B, Π as given numerical constants (independent of x) giving a two-parameter (m, α) model. For given (m, α), (4.12)

is then a transcendental equation for ϵ that can be solved numerically. We note in passing that, for given ϵ, (4.12) can be in fact be solved analytically for $\alpha(\epsilon)$ giving closed form solutions. But we prefer to fix α as the physical control parameter and so proceed numerically. Once ϵ is known U_∞/u_τ follows from (4.4) while $\delta^*/x \equiv Re_{\delta^*}/Re_x$ and $\theta/x \equiv Re_\theta/Re_x$ can be obtained from (4.6) and (4.7) respectively. For general m, and at finite viscosity ν, there exists a length scale $(\nu/P)^{1/(m+1)}$ and a streamwise Reynolds number $Re_x = P\,x^{1+m}/\nu$. The case $m = 0$ corresponds to the ZPGTBL with $P = U_\infty$ for which the length scale is the inverse of the unit Reynolds number U_∞/ν. An exception is $m = -1$ where no length-scale exists and the Reynolds number is independent of x.

Asymptotic behaviour when $\alpha \to 0$

If $\log(\epsilon)$ is neglected compared with $\log(\alpha)$ in (4.12), an asymptotic form for ϵ when $\alpha \to 0$ can be obtained. For illustrative purposes we display this for $m = 0$ only as

$$\epsilon = \frac{2\,\kappa^2\,\pi}{(-4 + \Pi^2 + 2\,B\,\kappa\,(1+\Pi))\,\pi - 4\,\Pi\,Q - 2\,(1+\Pi)\,\pi\,\log[\alpha]} + HOT. \quad (4.13)$$

When $\alpha \to 0$ so that $|\log[\alpha]| >> 1$, this becomes

$$\epsilon \equiv \frac{\delta}{x} = -\frac{\kappa^2}{(1+\Pi)\,\log[\alpha]} + HOT. \quad (4.14)$$

Substitution into (4.6) and (4.7) gives

$$\frac{\delta^*}{x} = \left(\frac{\kappa}{\log[\alpha]}\right)^2 + HOT, \quad \frac{\theta}{x} = \left(\frac{\kappa}{\log[\alpha]}\right)^2 + HOT. \quad (4.15)$$

Substitution of (4.13) into (4.4) then shows that

$$U_\infty^+ = -\frac{1}{\kappa}\,\log(\alpha) + O\left(\log(-\log(\alpha))\right), \quad \alpha \to 0, \quad (4.16)$$

and is singular in this limit. It can be verified that (4.9) is satisfied to leading order and further, that when $\alpha \to 0$, $H \equiv \delta^*/\theta \to 1$. The model is not asymptotic to smooth-wall flow when $\alpha \to 0$. Smooth-wall flow always requires a description of Reynolds number effects which are not included in the analysis.

4.3.3 Self-similar mean-velocity profiles

If the outer flow is given by fixing m, the only remaining parameter is the roughness slope α, and so all quantities are then functions of α. For α fixed, the mean velocity

profile can now be written in a self similar form with similarity variable $\eta \equiv z/(\alpha\, x)$

$$\frac{u(z)}{u_\tau} = \begin{cases} \frac{1}{\kappa}\left(\log(\eta) + 2\,\Pi\,\sin^2\left(\dfrac{\pi\,\alpha}{2\,\epsilon(\alpha)}\,\eta\right)\right) + B, & \eta < \epsilon(\alpha)/\alpha \\ \\ U^+_\infty, & \eta > \epsilon(\alpha)/\alpha. \end{cases} \tag{4.17}$$

Using continuity, the wall-normal velocity component is

$$\frac{w(z)}{u_\tau} = \begin{cases} \frac{1}{\kappa}\left[\alpha\,\eta\left(1 - \Pi\,\cos\left(\dfrac{\pi\,\alpha}{\epsilon(\alpha)}\,\eta\right)\right) + \dfrac{\epsilon(\alpha)\,\Pi}{\pi}\,\sin\left(\dfrac{\pi\,\alpha}{\epsilon(\alpha)}\,\eta\right)\right], & \eta < \epsilon(\alpha)/\alpha \\ \\ \dfrac{\epsilon(\alpha)(1+\Pi)}{\kappa}, & \eta > \epsilon(\alpha)/\alpha. \end{cases} \tag{4.18}$$

The streamline slope at $z = \delta = \epsilon(\alpha)\,x$ is

$$\left(\frac{dz}{dx}\right)_{z=\delta} = \frac{\epsilon(\alpha)\,(1+\Pi)}{B\,\kappa + 2\,\Pi + \log(\epsilon(\alpha)/\alpha)}. \tag{4.19}$$

The above model can easily be formulated with α replaced by a specified value of k_s/δ as the independent parameter. While this is somewhat closer to the concept of the fully-rough limit of the Moody diagram, with here k_s/δ playing the role of k_s/D for a pipe flow, we nonetheless retain α as the parameter because this will be defined by a given roughness profile.

4.4 Some special cases

Three cases of interest are:

4.4.1 Falkner-Skan flows

For Falkner-Skan type boundary layer flows, $m = \beta/(2\,\pi - \beta)$ where $\beta > 0$ is a wedge double angle. Here the streamwise co-ordinate x has an origin at the start of the boundary layer and $m > 0$. The pressure gradient is favourable and it may be expected that Π is approximately constant. This case is not discussed further.

4.4.2 The zero-pressure-gradient turbulent boundary layer $m = 0$

Here $x > 0$ where $x = 0$ is the virtual origin of the boundary-layer growth. Tables 4.1 and 4.2 show the model parameters calculated numerically for four values of α. First numerical values of κ, B, Π are specified with $m = 0$. For several values of α, (4.12) is then solved numerically for $\epsilon = \delta/x$. The quantity $\delta/k_s = (\delta/x)/(k_s/x) = \epsilon/\alpha$ can

Table 4.1: Numerical results for boundary layer with $m = 0$, $k_s = \alpha\, x$, $x > 0$. $\kappa = 0.384$, $B = 8.5, \Pi = 0.55$ using the model of §4.3.2. Values of α specified with other quantities calculated from model as described in §4.4.2.

α	U_∞^+	$\frac{\theta}{x}$	$\frac{\delta^*}{x}$	$\epsilon = \frac{\delta}{x}$	$\frac{\delta}{k_s}$
10^{-7}	40.46	6.08×10^{-4}	7.36×10^{-4}	7.40×10^{-3}	7.40×10^{4}
10^{-6}	35.03	8.15×10^{-4}	1.02×10^{-3}	8.86×10^{-3}	8.86×10^{3}
10^{-5}	29.60	1.14×10^{-3}	1.49×10^{-3}	1.10×10^{-2}	1.10×10^{3}
10^{-4}	24.30	1.69×10^{-3}	2.39×10^{-3}	1.44×10^{-2}	1.43×10^{2}
10^{-3}	19.22	2.71×10^{-3}	4.28×10^{-3}	2.04×10^{-2}	2.04×10^{1}

Table 4.2: Numerical results for boundary layer with $m = 0$, $k_s = \alpha\, x$, $x > 0$. $\kappa = 0.384$, $B = 8.5, \Pi = 0.36$ using the model of §4.3.2. Values of α specified with other quantities calculated from model as described in §4.4.2.

α	U_∞^+	$\frac{\theta}{x}$	$\frac{\delta^*}{x}$	$\epsilon = \frac{\delta}{x}$	$\frac{\delta}{k_s}$
10^{-7}	39.91	6.23×10^{-4}	7.48×10^{-4}	8.42×10^{-3}	8.42×10^{4}
10^{-6}	34.38	8.45×10^{-4}	1.04×10^{-3}	1.01×10^{-2}	1.01×10^{4}
10^{-5}	28.95	1.19×10^{-3}	1.53×10^{-3}	1.25×10^{-2}	1.25×10^{3}
10^{-4}	23.65	1.79×10^{-3}	2.45×10^{-3}	1.63×10^{-2}	1.63×10^{2}
10^{-3}	18.56	2.96×10^{-3}	4.42×10^{-3}	2.32×10^{-2}	2.32×10^{1}

Table 4.3: Comparison of present model of §4.3.2 with experiments of Kameda et al. [37]: $\alpha = 0.0055$, $m = 0$, $\kappa = 0.384, B = 8.5$. $\Delta_{R-C} = \delta^*\, U_\infty/u_\tau$ is the Rotta-Clauser parameter. Values of H for experiment obtained using an average of δ^*, θ tabulated in Talluru et al. [85].

Case	Π	U_∞^+	$\frac{\theta}{x}$	$\frac{\delta_{99}}{k}$	$\frac{\Delta_{R-C}}{k}$	$H = \frac{\delta^*}{\theta}$
Model	0.70	16.21	0.00380	16.66	92.64	1.88
	0.55	15.67	0.00407	18.26	92.86	1.82
Expt.		15.56	0.00477	19.43	78.33	1.83

Table 4.4: Numerical results boundary layer sink flow with $m = -1$, $k_s = \alpha\, x$, $x < 0$. $\kappa = 0.384$, $B = 8.5, \Pi = 0$ using model of §4.3.2. Values of α specified with other quantities calculated from model.

α	U_∞^+	$\frac{\theta}{(-x)}$	$\frac{\delta^*}{(-x)}$	$-\epsilon = \frac{\delta}{(-x)}$	$\frac{\delta}{k_s}$	β
-10^{-7}	36.97	3.38×10^{-4}	3.94×10^{-4}	5.59×10^{-3}	5.59×10^{4}	-0.538
-10^{-6}	31.43	4.61×10^{-4}	5.52×10^{-4}	6.66×10^{-3}	6.66×10^{3}	-0.545
-10^{-5}	25.98	6.58×10^{-4}	8.24×10^{-4}	8.21×10^{-3}	8.21×10^{2}	-0.556
-10^{-4}	20.65	1.00×10^{-3}	1.34×10^{-3}	1.06×10^{-2}	1.06×10^{2}	-0.572
-10^{-3}	15.53	1.65×10^{-3}	2.49×10^{-3}	1.49×10^{-2}	1.49×10^{1}	-0.600

then be calculated which enables calculation of U_∞/u_τ using (4.4). Finally $\delta^*/x \equiv Re_{\delta^*}/Re_x$ and $\theta/x \equiv Re_\theta/Re_x$ are calculated using (4.6) and (4.7) respectively.

We fix $\kappa = 0.384, B = 8.5$ which are standard values (we note that these cannot be independently selected). The value of Π is somewhat uncertain. We use a standard value $\Pi = 0.55$. Solving (4.9) for Π gives $\Pi = \kappa\,(\Delta/\delta) - 1$. In the LES to be described it was found that for the higher resolution runs, $\Delta/\delta_{99} = 3.54$ independent of α. If we identify δ_{99} (LES) = δ (model), then we calculate $\Pi = 0.36$ which will be taken as an alternative value. These values are used in Tables 4.1 and 4.2 respectively which can be taken to show the effect of Π on the calculated results. Calculations were also done (not shown) using an alternative algebraic form of the wake function $W(z/\delta)$ (see Jones, Marusic, and Perry [36]) with small effect on calculated quantities for the same specified κ, B, Π. In the tables it may be seen that as α increases, U_∞/u_τ decreases meaning that C_f increases with increasing roughness in qualitative agreement with rough-wall pipe flow.

The roughness elements used by Kameda et al. [37] for the ZPGTBL were of two-dimensional riblet-like form with rectangular cross section. Their height k to width w ratio was $k/w = 1$ while the element separation was $(b + w)/k = 4$. The local root-mean square roughness height is $\sigma = \sqrt{3}/4\,k$ and the riblet height increased linearly as $dk/dx = 0.00125$. In order to compare results of the present model with Kameda et al. [37], the equivalent sand-grain roughness k_s for the rectangular roughness elements must be determined. We estimate this at a single station and assume a linear dependence on the distance x from the leading edge. From Figures 7 and 9 of Kameda et al. [37], $\Delta U^+ \approx 13.2$ at $x = 3.340$ m while from their Figure 4, $C_f = 0.00826$ gives $U^+ = 15.56$. Using $k_s^+ \equiv k_s\,(U_\infty/\nu)/U^+$, their unit Reynolds number of $U_\infty/\nu = 6.24{\times}10^5$ m^{-1} and substituting into (4.2) with $\kappa = 0.384, B = 8.5$ then gives $k_s \approx 0.018$m at $x = 3.340$ m. This gives $\alpha = k_s/x = 0.0055$ which is 3.7 times the growth in k given by $dk/dx = 0.00125$ [37]and more than 8 times the rms value of the surface roughness. Values of equivalent sand-grain roughness that are substantially larger than the physical roughness scale have been observed previously. For example Squire et al. [82] report that the equivalent k_s for a specific sand-paper roughness is about 13 times the measured wall-normal root-mean-square length scale of the surface profile.

Results from the present model with $\alpha = 0.0055$ are shown in Table 4.3 for two values of $\Pi = 0.70$, the value suggested by Kameda et al. [37], and $\Pi = 0.55$. In making a comparison with experiment we have identified $\delta = \delta_{99}$. The present

model assumes the existence of a log regime. Jiménez [35] remarks that $\delta/k \geq 40$ is needed in order to produce a finite log layer, otherwise the log-layer may be suppressed by the wall-normal extent of the viscous roughness sublayer. Kameda et al. [37] find $\delta/k \approx 19.4$. Since we have

$$k_s^+ = \left(\frac{\delta_{99}}{k_s}\right)^{-1} Re_\tau, \tag{4.20}$$

then large $k_s^+ > 100$ (asymptotically rough regime) coupled with large δ_{99}/k_s requires large Re_τ. In Kameda et al. [37], $Re_\tau \sim 2200 - 4030$ which is on the low side for this.

4.4.3 Boundary-layer sink flow $m = -1$

Boundary layer sink flow given by $m = -1$. Here, to a good approximation we may take $\Pi = 0$ [21, 36]. For this case $x < 0$ with the origin of x at the sink. Hence $\epsilon < 0$, $\alpha < 0$. The calculated parameters for this flow are given in Table 4.4. These parameters can be seen to be qualitatively similar to the zero-pressure gradient case. Pure sink flow exhibits some special features. First, $Re_x = P/\nu$ is constant; the Reynolds numbers at all streamwise stations are the same, and so there exists a family of sink flows with parameter P/ν. In other words, with P and ν fixed, large Reynolds number cannot be achieved with a sufficiently long plate. Second, the boundary layer for pure sink flow for the smooth-wall case is of equilibrium form and is self-similar [21]. As a result, the present model applied to sink flow with linearly reducing roughness can in fact be mapped into the smooth wall case. Calculation shows that the equivalence is $(u_\tau/U_\infty)\,\alpha \to \nu/P$. So for pure sink flow, both the smooth-wall flow and the sink flow with linearly decreasing roughness at large Reynolds number are self similar.

While the Clauser parameter $\beta = \delta^*/\tau_w\, dp/dx$ is useful mainly for flows with adverse pressure gradients [18], it is interesting that this is exactly constant for the present class of rough-wall flows. It is straightforward to show that

$$\beta = -m \left(\frac{U_\infty}{u_\tau}\right)^2 \frac{\delta^*}{x} \tag{4.21}$$

and is negative for flows with favourable pressure gradients. Values for $m = -1$ are given in Table 4.4. These can be seen to be small in magnitude.

4.4.4 Recycling

For generating the inflow, we refer to the recycling method by Lund, Wu, and Squires [42], in which the components of inflow velocity, including mean and fluctuation

parts, are mapped from the flow field at an internal plane. This mapping idea originates from the scaling-similarity property of boundary layer flow. Similar to the classical scaling, the recycling method recognises an inner region and an outer region. In the original recycling method for zero-pressure-gradient turbulent boundary layer flow, velocity components in the inner region are mapped using the law of wall, which means the scaled coordinate is $z^+ = z/l^+$ with $l^+ = \nu/u_\tau$. In the outer region, velocity components are recycled using the defect law, where the scaled coordinate is $\eta = z/\delta$ with δ some measure of the boundary layer thickness. For the entire recycling process, velocity components are scaled using u_τ.

The formula used for the recycling method can thus be summarised as follows:

$$\phi_{in}^{inn} = \phi_{re}^{inn}, \quad \phi_{in}^{out} = \phi_{re}^{out}, \tag{4.22}$$

where ϕ denotes the velocity component, either the mean streamwise velocity $u(z)$, the mean wall-normal velocity $w(z)$, or three fluctuation components $u'(y,z)$, $v'(y,z)$ and $w'(y,z)$. The subscripts "in" and "re" for the inlet plane and recycling plane indicate the position where velocity components are evaluated. The superscripts "inn" and "out" denote different scaled coordinate as discussed above.

In generating the inflow velocity, a weighted function is defined to combine the velocity components in inner region and outer region. This procedure closely follows the original recycling method, and its detailed description is not repeated here. In the implementation of the recycling procedure, the mirroring method by Jewkes et al. [34], which serves to almost remove the spatially quasi-periodic effect, is used.

4.4.5 LES performed

The LES were performed on a rectangular domain. Parameters for the LES discussed are summarised in Table 4.5. In what follows we refer to two streamwise co-ordinates x and x' related by $x' = x - x_0$. The co-ordinate x' has origin $x' = 0$ at the domain inlet while the origin of x is the nominal flat-plate leading edge. Each individual LES was performed on a rectangular domain with inlet at $x = x_0, x' = 0$ where the determination of x_0 is to be discussed. At the domain inlet, in computational co-ordinates, δ_{99}, the 99% boundary layer thickness is set to unit length. With ν specified and $U_\infty = 1$ this fixes the nominal inlet Reynolds number $Re_{\delta_{99}} = \delta_{99} U_\infty/\nu$. For each LES the fixed parameters are then δ_{99}, U_∞, ν and

the streamwise roughness growth rate α. We note that $k_s = \alpha\, x$ and denote by $k_{s,0} = \alpha\, x_0$ the roughness height at the domain inlet $x = x_0$.

For given α, denote the value of δ/k_s given by the empirical model (see Table 4.1) by $(\delta/k_s)_{model}$. Then identifying $\delta_{99} = \delta$, an initial estimate of x_0 is

$$x_0 = \frac{1}{\alpha}\left(\frac{\delta}{k_s}\right)^{-1}_{model}. \tag{4.23}$$

With x_0 known, LES is then performed with fixed parameters and with k_s calculated as $k_s(x) = \alpha\, x = \alpha\,(x' + x_0)$. It was found that, following the usual transient to statistically steady flow, $\theta(x)$ obtained from the LES showed a strong linear correlation with x' downstream of the recycling region, but that its virtual origin was near to but not at the present x_0. An updated x_0 was then calculated using linear extrapolation of θ in x' to determine a virtual leading-edge origin $x' = -x_0$. For each fixed α and $Re_{\delta_{99}}$, an iterative process was then used until a converged x_0 was obtained. For 1% accuracy, usually 1-3 individual LES runs were required. We remark that (4.23) is used only as an initial guess for x_0 in the iterative process and is then abandoned. In this sense the present LES results are independent of the empirical model.

In this way, LES were performed for $\alpha = (10^{-4}, 10^{-5}, 10^{-6}, 10^{-7})$, each with several values of Re_x. The case $\alpha = 1.25 \times 10^{-3}$ was not considered because a log-layer is not expected for this α. The only physical length scale available for these LES is ν/U_∞. Hence mean flow results in the physical (x, y) plane are presented as either $(Re_x, Re_\theta) = (U_\infty\, x/\nu, U_\infty\, \theta/\nu)$ or as scaled versions of these co-ordinates.

4.5 Results and discussion

Figure 4.1 shows U^+_∞ versus Re_x for a series of higher-resolution (BH,CH,DH) LES runs at different α and at different inlet Reynolds numbers. Three ranges of Re_x - lower, intermediate and higher - are shown for each α. For all cases, the results displayed begin at the recycling plane and extend downstream. For all runs, some effect of the recycling region $0 \le x/L_x \le 0.2$, can be seen just downstream of the recycling plane. As Re_x increases, U^+_∞ remains almost constant for each α but at levels that vary with α. In this sense these figures can be interpreted as essentially the fully-rough, large-Reynolds number limit for the zero-pressure gradient boundary layer flowing over roughness whose scale increases linearly with x.

The corresponding variation of Re_θ with distance x is displayed in Figure 4.2 in both linear-log (a) and log-log (b) form. Figure 4.2(a) indicates that all curves appear to

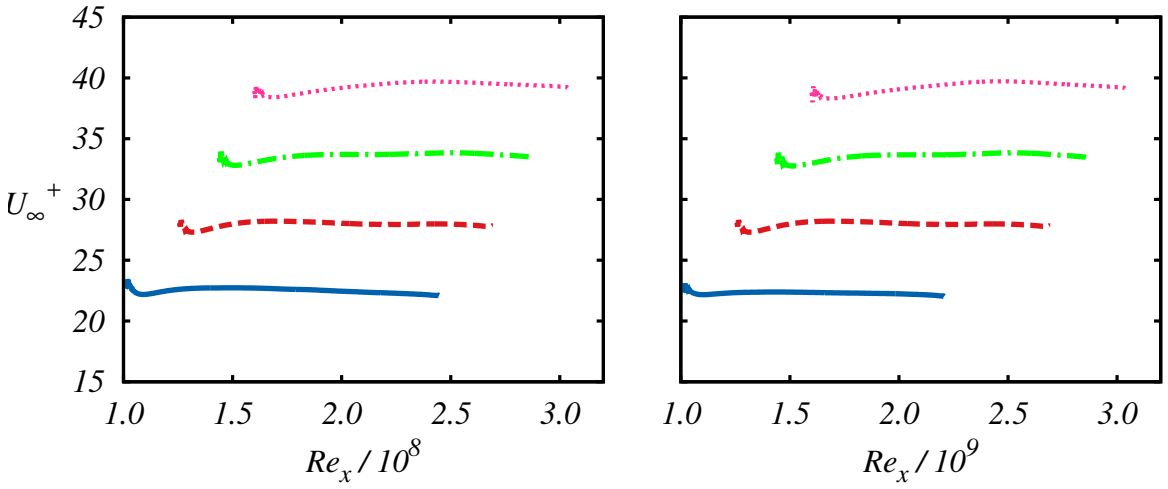

(a) Low *Re*

(b) Intermediate *Re*

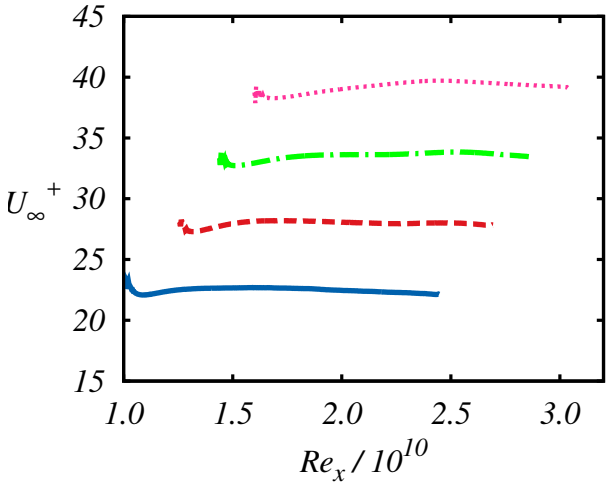

(c) High *Re*

Figure 4.1: Velocity ratio U_∞^+ for a range of Re_x: Results represent individual LES over different Re_x. Results plotted are for cases *BH*, *CH*, *DH*. Line key: ——, $\alpha = 10^{-4}$; — — — —, $\alpha = 10^{-5}$; — · — ·, $\alpha = 10^{-6}$; ····, $\alpha = 10^{-7}$. Note increasing U_∞^+ with decreasing α.

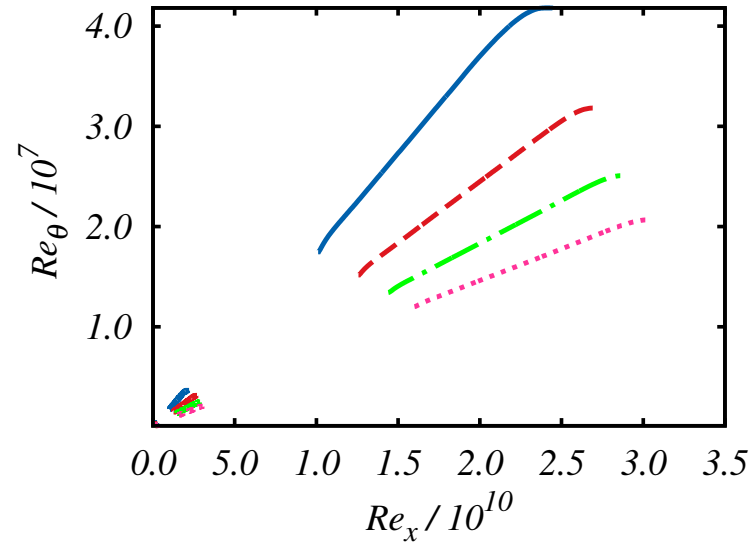

(a) Linear-linear plot of Re_θ vs Re_x

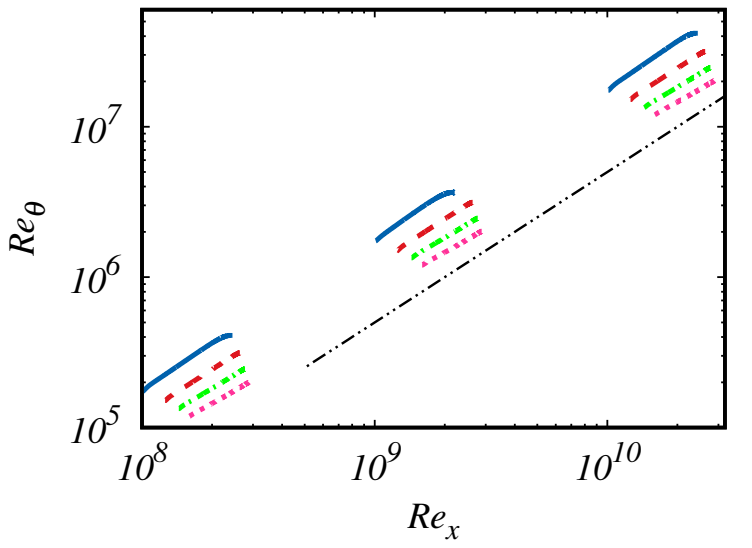

(b) Log-log plot of Re_θ vs Re_x

Figure 4.2: Re_θ versus Re_x with linear-linear (top) and log-log (bottom) axes. Cases BH, CH, DH. Results represent individual LES over different Re_x for cases BH, CH, DH. See Fig. 4.1 for key. —·—·—·— : $Re_\theta \sim Re_x$.

Table 4.5: Summary of zero pressure gradient LES with linear roughness: Numbers represent the particular case of α, letters represent different inflow Re_x, H represents a high-resolution simulation. Letters represent order of magnitude of Re_x - $B : 10^8$, $C : 10^9$, $D : 10^{10}$

$Case$	α	Re_x	N_x	N_y	N_z	$\frac{L_x}{\delta_0}$	$\frac{L_y}{\delta_0}$	$\frac{L_z}{\delta_0}$
$1B$	10^{-4}	$1.01 - 2.45 \times 10^8$	192	32	64	90	6	12
$1C$	10^{-4}	$1.01 - 2.16 \times 10^9$	192	32	64	72	6	12
$1D$	10^{-4}	$1.01 - 2.45 \times 10^{10}$	192	32	64	90	6	12
$1BH$	10^{-4}	$1.01 - 2.45 \times 10^8$	384	64	128	90	6	12
$1CH$	10^{-4}	$1.01 - 2.16 \times 10^9$	384	64	128	90	6	12
$1DH$	10^{-4}	$1.01 - 2.45 \times 10^{10}$	384	64	128	90	6	12
$2B$	10^{-5}	$1.26 - 2.70 \times 10^8$	192	32	64	90	6	7
$2C$	10^{-5}	$1.26 - 2.70 \times 10^9$	192	32	64	90	6	7
$2D$	10^{-5}	$1.26 - 2.70 \times 10^{10}$	192	32	64	90	6	7
$2BH$	10^{-5}	$1.01 - 2.70 \times 10^8$	384	64	128	90	6	7
$2CH$	10^{-5}	$1.01 - 2.70 \times 10^9$	384	64	128	90	6	7
$2DH$	10^{-5}	$1.01 - 2.70 \times 10^{10}$	384	64	128	90	6	7
$3B$	10^{-6}	$1.44 - 2.88 \times 10^8$	192	32	64	90	6	7
$3C$	10^{-6}	$1.44 - 2.88 \times 10^9$	192	32	64	90	6	7
$3D$	10^{-6}	$1.44 - 2.88 \times 10^{10}$	192	32	64	90	6	7
$3BH$	10^{-6}	$1.01 - 2.88 \times 10^8$	384	64	128	90	6	7
$3CH$	10^{-6}	$1.01 - 2.88 \times 10^9$	384	64	128	90	6	7
$3DH$	10^{-6}	$1.01 - 2.88 \times 10^{10}$	384	64	128	90	6	7
$4B$	10^{-7}	$1.60 - 3.04 \times 10^8$	192	32	64	90	6	7
$4C$	10^{-7}	$1.60 - 3.04 \times 10^9$	192	32	64	90	6	7
$4D$	10^{-7}	$1.60 - 3.04 \times 10^{10}$	192	32	64	90	6	7
$4BH$	10^{-7}	$1.60 - 3.04 \times 10^8$	384	64	128	90	6	7
$4CH$	10^{-7}	$1.60 - 3.04 \times 10^9$	384	64	128	90	6	7
$4DH$	10^{-7}	$1.60 - 3.04 \times 10^{10}$	384	64	128	90	6	7

Table 4.6: Symbol key for plots with multiple streamwise stations. Stations identified by $Re_x/10^9$

α	■	●	▲	▼
10^{-4}	2.15	2.11	2.08	2.04
10^{-5}	2.63	2.58	2.53	2.49
10^{-6}	2.81	2.77	2.72	2.68
10^{-7}	2.97	2.93	2.88	2.84

converge to the same virtual leading edge, independent of α. A plot of $Re_{\delta*}$ versus Re_x (not shown) shows similar trends. In Figure 4.2 some domain end effects can be seen for all LES. These are most pronounced for the largest value of α. Both

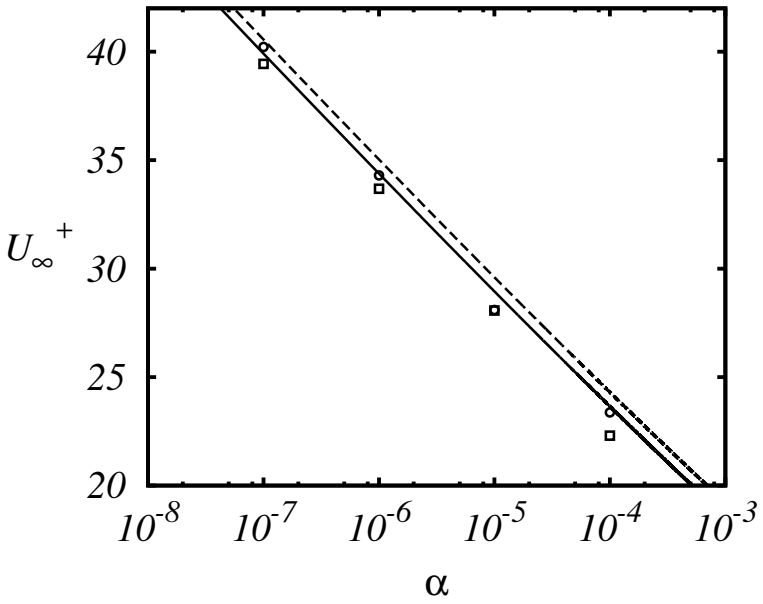

Figure 4.3: Friction velocity ratio U_∞^+ versus α. □, HR-LES; ◯, LR-LES. Solid line; model of §4.3.2 with $\kappa = 0.384, B = 8.5, \Pi = 0.55$. Dashed line; Model with $\kappa = 0.384, B = 8.5, \Pi = 0.36$. Symbols indicate values obtained from LES via averaging from $x'/L_x = 0.2$ to $x'/L_x = 0.90$ in order to avoid effects of the outlet boundary condition. Cases CH, DH.

plots clearly indicate an approximately linear growth of Re_θ with slopes that depend on α but that appear sensibly independent of Re_x. Together, these plots indicate an asymptotic state of the boundary layer at large Re_x that depends on the single parameter α.

In the following comparisons all model calculations use $\kappa = 0.384$, $B = 8.5$ and $\Pi = 0.36, 0.55$. Plots of average values of U_∞^+ and θ/x and δ_{99}/x obtained from the LES are displayed in Figures 4.3 and 4.4 respectively. Both high resolution and low resolution runs are shown for cases C, D (intermediate and large Re_x range). The LES values shown as symbols were obtained by streamwise averaging from $x'/L_x = 0.2$ to $x'/L_x = 0.90$ in order to avoid effects of the outlet boundary condition. In each figure, the solid and dashed lines indicates values derived from the model of §4.3.2 over a continuous range of α for the parameter values shown in the caption. In Figure 4.3, both the lower and higher resolution LES shows good agreement for U_∞^+ with the model predictions for both values of Π. The agreement between the model and LES results for $\overline{\theta}/x$ in Figure 4.4(a) is also good. In Figure 4.4(b) we have plotted δ_{99}/x for the LES and δ defined by the log-wake law for

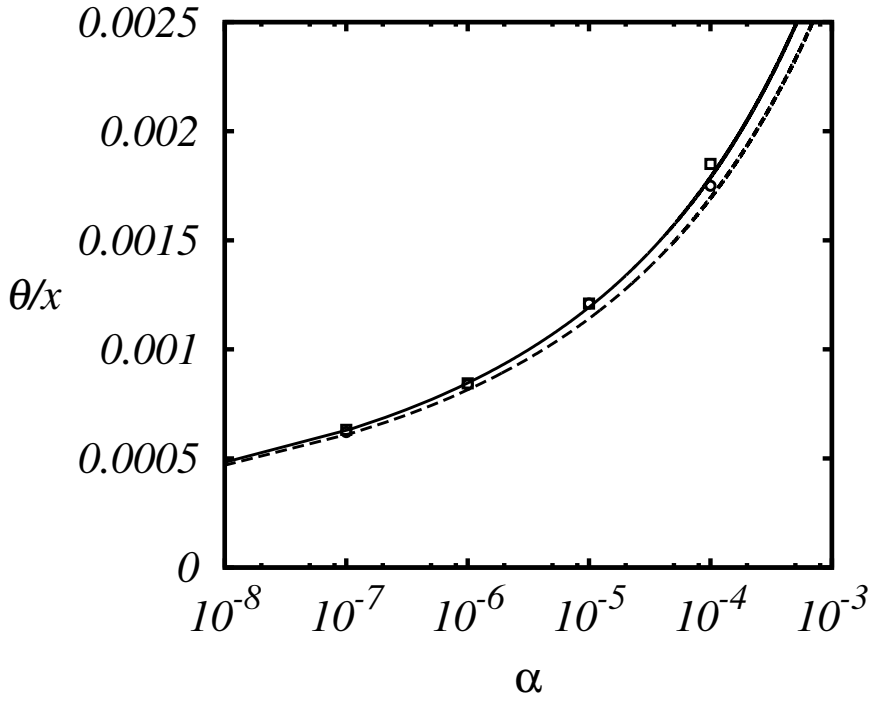

(a) θ/x versus α

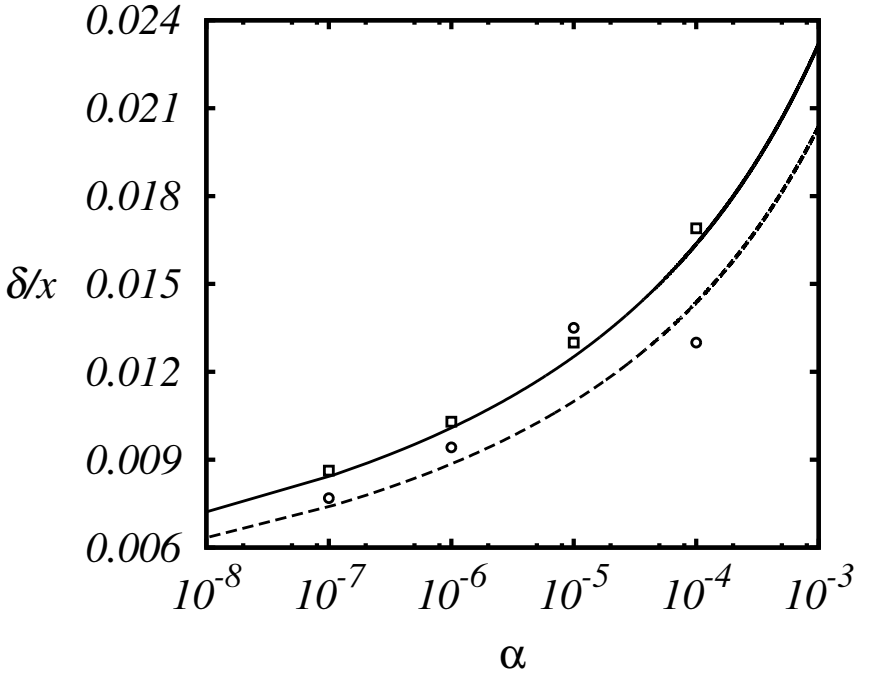

(b) δ/x versus α

Figure 4.4: θ/x versus α and δ/x versus α. For key, see Figure 4.3. LES results represent δ_{99} versus α.

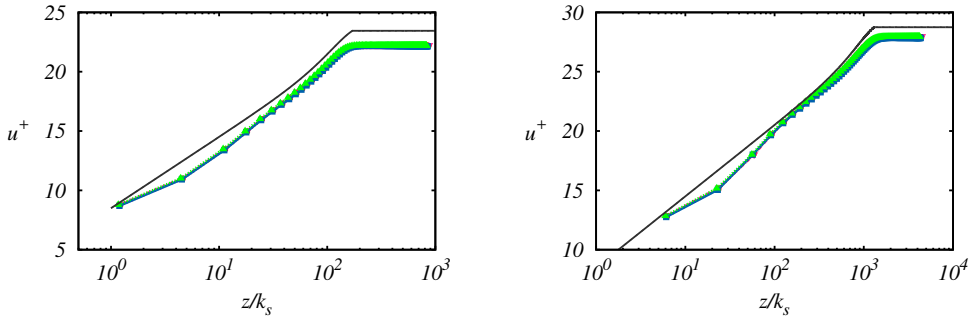

(a) $\alpha = 10^{-4}$ (b) $\alpha = 10^{-5}$

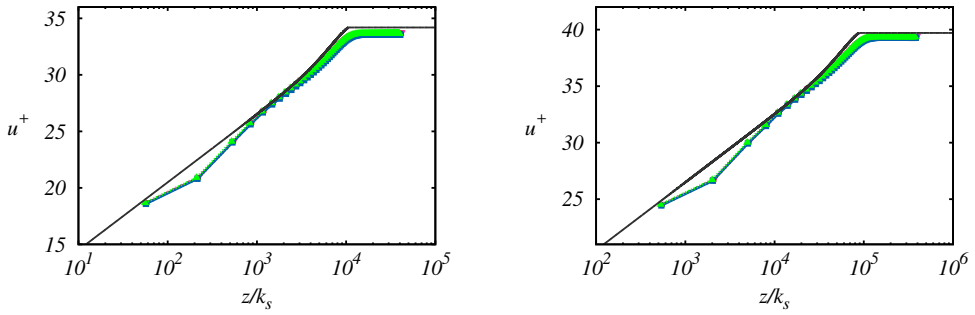

(c) $\alpha = 10^{-6}$ (d) $\alpha = 10^{-7}$

Figure 4.5: Mean velocity profiles u^+ versus $z/k_s = z/(\alpha\, x)$ at four streamwise stations for each α. Results plotted are for cases CH. Values of α as shown. Symbols represent different streamwise stations. See Table 4.6 for key. Solid line; (4.17) with $\kappa = 0.384$, $B = 8.5$, $\Pi = 0.55$

the model. We note that Squire et al. [82] suggest $\delta = 1.26\,\delta_{99}$ but this is not used presently. Overall, Figures 4.1-4.4 indicate that the LES shows similar trends with acceptable quantitative agreement with the semi-empirical model. At large Re_x, decreasing α leads to increased U_∞^+ but slower streamwise boundary-layer growth.

Figure 4.5 shows mean-velocity profiles $u(z)/\overline{u}_\tau$ versus $z/(\alpha\, x)$ for $\alpha = 10^{-4}$, 10^{-5}, 10^{-6}, 10^{-7}. For each value of α, four velocity profiles at streamwise stations indicated in the figure caption are plotted. Reasonable collapse at each α is indicated. The LES show small near-wall effects in the final three near-wall grid points. Also shown in each subfigure is the model mean-velocity profile (4.17). These use the values of α shown together with $\kappa = 0.384$, $B = 8.5$ and $\Pi = 0.55$. The model profile shows slightly higher U_∞/u_τ than the LES profile for each α consistent with the differences between results from the semi-empirical model and the LES shown in Figure 4.3.

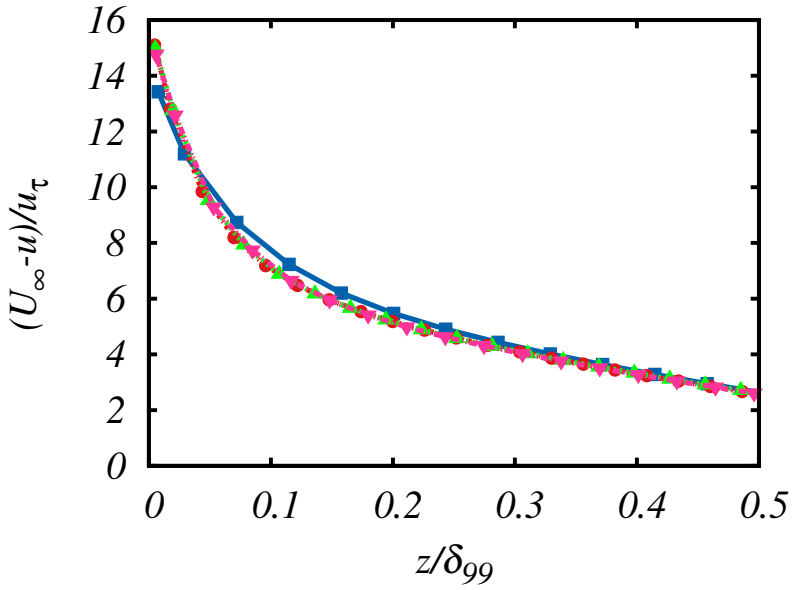

(a) Velocity defect versus z/δ_{99}.

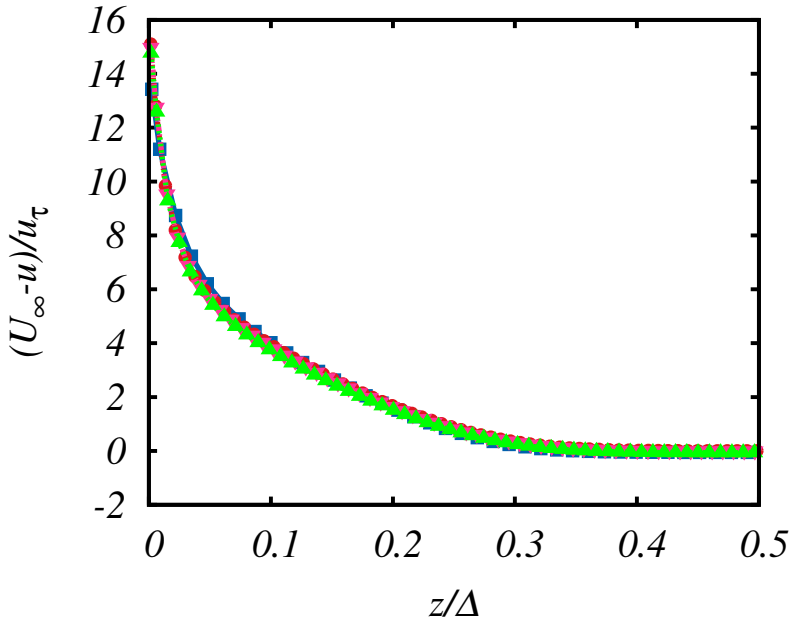

(b) Velocity defect versus z/Δ.

Figure 4.6: Velocity defect $(U_\infty - u)/u_\tau$ for a range of roughness slopes α: versus the wall-normal coordinate z. Single streamwise station for each α shown for clarity. (a) Versus z/δ_{99}. (b) Versus z/Δ with Rotta-Clauser parameter $\Delta = U_\infty \delta^* / u_\tau$. Symbol key: ■, $\alpha = 10^{-4}$; ●,$\alpha = 10^{-5}$; ▲,$\alpha = 10^{-6}$; ▼,$\alpha = 10^{-7}$.

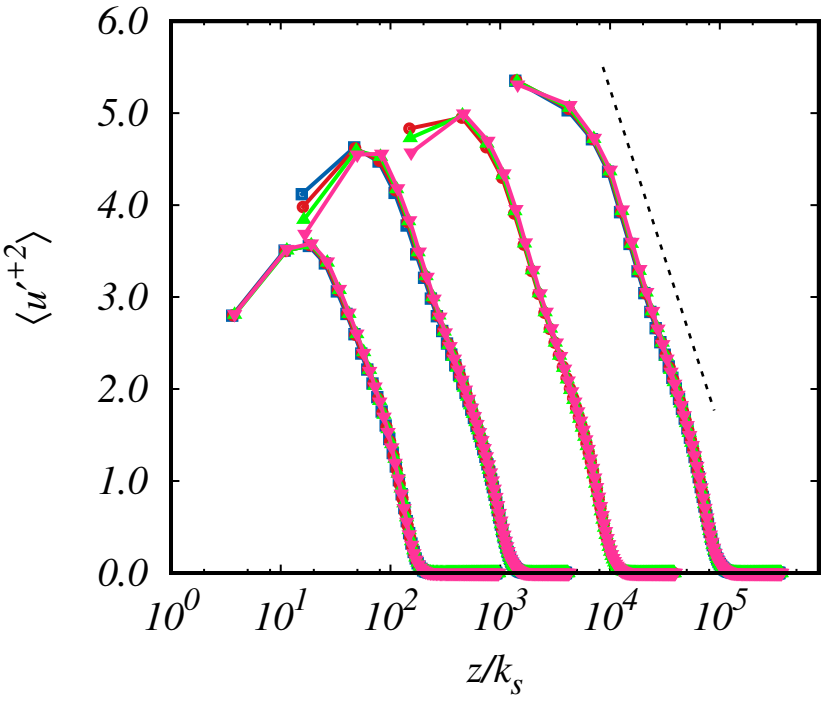

Figure 4.7: streamwise velocity fluctuations $< u'^{+2} >= \frac{\overline{u'^2}}{u_\tau^2}$. Four streamwise stations for each α shown. Note α decreasing left to right. Dashed line is of the form $< u'^{+2} >= B_1 - A_1 \log(z/k_s)$ with $A_1 = 1.60$. See Table 4.6 for key.

In Figure 4.6 the defect velocity $(u - U_\infty)/\overline{u}_\tau$ is plotted against both z/δ_{99} and z/Δ. One profile for each of the four values of α is plotted. Equations (4.3) and (4.4) together suggest that $U_\infty^+ - u^+$ is a function of z/δ_{99} independent of α provided we identify $\delta = \delta_{99}$. This is because the $-\log(k_s)/\kappa$ terms cancel. That $U_\infty^+ - u^+$ can also be expressed as a function of z/Δ independent of α is suggested by the constancy of the ratio $\Delta/\delta_{99} = 3.54$ across all α in the LES and also from the model equation (4.9) that does not depend explicitly on α. Figure 4.6(b) shows reasonable collapse against z/Δ. The collapse is not as good against z/δ_{99} in 4.6(a) where small effects of α can be seen.

Streamwise velocity variances $< u'^{+2} > \equiv \overline{u'^2}/\overline{u}_\tau^2$ obtained from the LES are shown in Figures 4.7 and 4.8. In Figure 4.7, these are plotted against $z/(\alpha\, x)$. Again four streamwise stations are shown in each plot. The three near-wall points are probably affected by the wall modeling and cannot be considered accurate. While the effect of α can clearly be seen in the separation of the profiles when plotted against $z/k_s =$

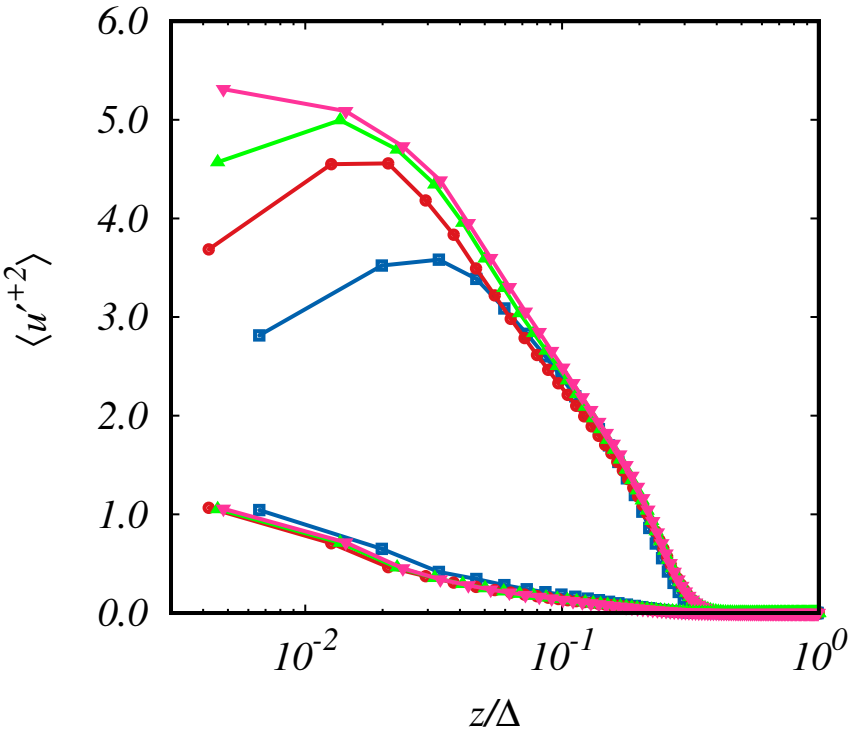

Figure 4.8: Streamwise velocity fluctuations $< u'^{+2} >= \frac{\overline{u'^2}}{u_\tau^2}$ versus z/Δ. One streamwise station for each α shown for clarity. Both sub-grid and total (sub-grid plus resolved-scale) results shown. See Fig 4.6 for symbol key.

$z/(\alpha\, x)$, each profile appears to have approximately the same slope in linear-log coordinates. For the turbulent boundary layer over a uniformly rough wall, Squire et al. [82] find an approximately logarithmic profile for streamwise velocity variances with slope $A_1 \approx 1.27$. Figure 4.7 suggests the form $< u'^{+2} >= B_1(\alpha) - A_1 \log(z/k_s)$ where A_1 is independent of α. The light solid line in the figure has slope $A_1 \approx 1.60$. In Figure 4.8 $< u'^{+2} >$ is plotted against z/Δ, with some degree of collapse over the outer region. The profiles shown in both Figures 4.7 and 4.8 comprise the sum of the resolved-scale component plus the sub-grid component obtained from the SGS model. The latter are shown in Figure 4.8, where they are small but not negligible.

The constant skin-friction turbulent boundary layer has thus been identified as a promising candidate for further study given the observed self-similarity and linear boundary layer growth measures, as emphasised in this chapter with the zero-pressure-gradient constant free-stream velocity ($m = 0$) case. The simplicity of the LES model suggests its utility in examining similar flows of the Falkner-Skan

type - results suggest the existence of an (α, m) family of curves for skin-friction that give a Moody-like diagram for turbulent boundary-layers. Contact with low Re experiments is restricted by the requirement of subgrid roughness $\max(k_s) < h_0$. An appropriate experimental assessment of the ability to control the roughness slope might lead to desirable skin-friction characteristics in applications. This is made more relevant by the increasing prominence of small-scale manufacturing techniques. While we have assumed that the origin of the boundary layer growth is consistent with the origin of the linearly increasing roughness-scale; an opportunity exists for the examination of a flow transition from the equilibrium smooth-walled boundary layer to a fully rough boundary layer. The successful application of the local velocity deficit correction $\Delta U^+(k_s^+)$ to the virtual-wall model suggests the possibility for the exploration of abrupt roughness changes. We address the latter subject in chapter 5.

Chapter 5

LES OF TURBULENT BOUNDARY LAYERS WITH ABRUPT SPATIAL CHANGES IN ROUGHNESS

5.1 Overview

In this chapter, we extend our analysis of turbulent boundary layers with spatially varying roughness to non-equilibrium flows. The non-equilibrium behaviour is introduced to the flow by considering cases with abrupt streamwise changes in boundary surface condition, for both smooth-rough and rough-smooth flows. This type of flow has wide-ranging applications, particularly in the areas of atmospheric boundary layers. Understanding the development of velocity and stress profiles provides a basis for improved flow modelling and perhaps to applications in manipulating drag characteristics.

5.2 Background

5.2.1 Implications of spatially varying roughness

A natural extension to the rough-wall boundary layer flow discussed in chapters 1 and 2, and the linear roughness variation studied in chapter 4 is the introduction of abrupt changes in the roughness distribution. Such flows have been considered in the context of atmospheric boundary layers by Chamorro and Porté-Agel [8], for instance in the case of flow from oceans to landmasses, where the ocean is considered 'smooth' and the land 'rough'. Localised patches of bio-fouling or forest distributions also present physically realistic examples of flows with spatially varying roughness. The distribution of rough elements on a surface can be classified as homogeneous, heterogeneous, isotropic or anisotropic. Homogeneous roughness specifies uniformity in the spatial and temporal description of roughness over the entire domain of interest, such as in Nikuradse's (1933) sand-grain pipe flow experiments. Anisotropy identifies directional bias due to the arrangement of roughness elements, such as that present in the case of riblet surfaces at non-zero yaw angles relative to the impingent flow [22, 58]. Smits and Wood [80] propose a classification based on the severity of the perturbation relative to the upstream flow and the extent of the validity of the boundary layer approximation in the developing downstream flow. In this manuscript, we focus on isotropic, inhomogeneous sand-grain type roughness with an abrupt streamwise transition from a smooth to rough condition

and vice versa.

One of the key studies investigating the effect of roughness transition in wall-bounded flows is attributed to Antonia and Luxton [3, 4]. They conducted experiments of rough-smooth and smooth-rough wall transition, using Preston tube measurements to examine the streamwise development of skin-friction and mean velocity profiles. More recently, the abrupt roughness variation problem has been studied by various authors experimentally [23, 30] and using direct numerical simulations [32]. Saito and Pullin [72] recently studied turbulent channel flows with smooth-rough-smooth wall boundary transitions using large eddy simulations (LES), examining first and second order flow statistics in addition to the growing internal boundary layer (IBL).

Studies of internal boundary layers have been conducted by several authors, including Antonia and Luxton [3, 4], followed by Ghosal [27] and reviewed in detail by Savelyev and Taylor [73]. The IBL serves as a demarcation between the flow immediately next to the wall affected by the new surface condition, and the outer region which adjusts to the new wall condition over several boundary layer thicknesses downstream. Savelyev and Taylor [73] comprehensively summarise various growth formulae for internal boundary layers in the case of TBL transition between two surfaces with differing roughness scales. We note that in the present research we consider transitions between ideally smooth and rough surfaces. Variation in surface roughness has immediate consequences on the near wall behaviour and drag characteristics of wall-bounded flows, and a detailed understanding of these parameters is critical to the development of models and simulation tools for engineering applications.

5.2.2 Scope of present study

The present approach utilizes wall-modelled large eddy simulations (LES) of zero pressure gradient flat plate turbulent boundary layers with modelled sand-grain type roughness as a tool to mitigate the computational costs associated with DNS, wherein grid requirements scale as $O(Re^{9/4})$, allowing us to study the abrupt roughness transition problem at high friction Reynolds numbers Re_τ. We study distinct physical scenarios - smooth-to-rough (SR) and rough-to-smooth (RS) transitions primarily in the asymptotically rough regime such that $k_s^+ \geq 100$ over the rough wall regions and Re_τ is in the range 10^4 to 10^6. Re_τ is chosen as the measure of interest due to its relevance to the skin-friction through u_τ.

5.3 SV, SGS LES with wall modelling

We refer to chapter 3 for a detailed description of the numerical method. The same filtered NS equations, stretched vortex subgrid scale model and virtual wall model (with a roughness correction) described therein and are applied to this problem. Chapter 3 contains a detailed description of the wall-model with roughness.

5.3.1 Wall model with roughness correction: ODE for friction velocity u_τ

In the present computational framework we use the virtual-wall model [16, 31, 12] with the roughness correction ΔU^+ proposed by Hama [29]. The roughness function $\Delta U^+(k_s^+)$ is a model specific roughness correction that may vary across the wall. In this chapter, we use the full-range interpolation formula of Colebrook [19] which covers both the transitional and asymptotically rough regions, and allows $k_s^+ = k_s^+(x, y)$ on the wall:

$$\Delta U^+ = \frac{1}{\mathcal{K}_1} \log(1 + \beta\, k_s^+) \tag{5.1}$$

where presently, $\beta = 0.26$. (In chapter 4 we used the asymptotically rough form of ΔU^+). We refrain from referring to this as the 'universal' interpolation formula due to the implication that this is valid for all engineering surfaces. Most LES reported here have $k_s^+ > 100$ which places the local flow in the fully rough regime where ΔU^+ take the asymptotic form

$$\Delta U^+ = \frac{1}{\kappa} \log(k_s^+) + A - B \tag{5.2}$$

where A and B are constants and $\beta = \exp(\kappa\,(A - B))$. We note that (5.2) is given for completeness and is not explicity utilised in the computations presented in this chapter. Since u_τ is dynamically space and time dependent, both k_s^+ and $\Delta U^+(k_s^+)$ also vary spatially and temporally on the wall. In the present study, we are primarily concerned with statistically stationary turbulence at large particle transit times in the streamwise direction.

5.3.2 Inflow and Boundary Conditions

A general description of the flat plate TBL problem has been presented in § 3.3.7. The inclusion of spatially varying ΔU^+ in the wall velocities enables us to focus on two distinct boundary layer flows, each describing the specific nature of the heterogeneity in the wall-roughness condition. These are smooth-to-rough (henceforth referred to as SR) and rough-to-smooth (RS). The transition to a new wall condition occurs abruptly over a single streamwise grid cell to simulate existing experimental investigations closely. Application of smoothing functions also introduces free

parameters related to the extent over which the roughness transition occurs. Each domain comprises of a recycling region, a development region (smooth or rough), an instantaneous streamwise change in roughness which introduces heterogeneity, and a uniformly smooth or rough zone thereafter for flow recovery. Usage of the wall model of Chung and Pullin [16] in the case of abrupt roughness transitions is based on the assumption that the flow adjusts immediately, within a single grid cell in the streamwise coordinate, to the downstream surface change up to $z < h_0$. Here, with $u^+ = (1/\kappa)\log(z/z_r)$ where $z_r = 1.02 \times 10^{-4}$ is the aerodynamic roughness lengthscale in the restrictive case, the estimated streamwise adjustment length of the roughness sublayer according to Cheng and Castro [9] is $160z_r = 0.016$, which in the present case is 5 times lower than the streamwise grid extent.

Turbulent inflow is generated using the recycling method described in chapter 3. In this section we address parts of the inflow generation recycling and bottom wall boundary conditions that are unique to the spatially varying turbulent boundary layer problem.

Smooth-Rough (SR)**: Recycling and bottom boundary**

Figure 5.1 summarises the domain setup for the SR wall transition. We employ a recycling region to generate realistic smooth wall turbulent inflow upstream of the SR transition. For the SR case, the recycling scheme described by Lund, Wu, and Squires [42] is applied using a plane $14.4\delta_{in}$ downstream of the inlet (δ_{in} is the 99% boundary layer thickness at the inlet) and modified with the mirroring method of Jewkes, Chung, and Carpenter [34] to remove spatial quasi-periodic effects. This method has been tested in smooth-wall boundary layer flows at large Re by Inoue and Pullin [31]. In discussing the results, δ_{SR} is the boundary layer thickness at the location of transition, and we shift our streamwise coordinate origin to the location of transition, such that $x_{SR} = 0$ at this point.

Velocities are first decomposed into mean U_i and fluctuating u_i' components, and again into the inner (superscript inn) and outer layers (superscript out) in the wall-normal coordinate. The composite inlet velocity profile $u_{i,inlet}$ is then given by (5.3)

$$(u_i)_{inlet} = [(U_i)^{inn}_{inlet} + (u_i')^{inn}_{inlet}][1 - W(\eta_{inlet})] + [(U_i)^{out}_{inlet} + (u_i')^{out}_{inlet}][W(\eta_{inlet})] \quad (5.3)$$

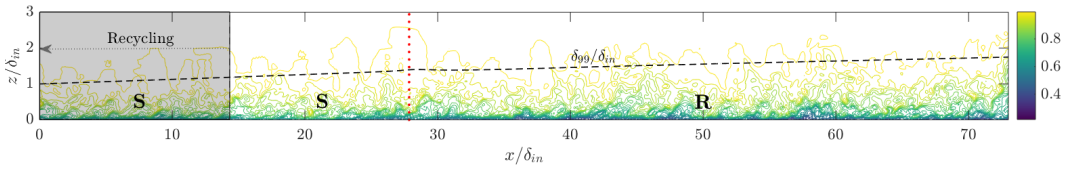

Figure 5.1: Flow visualisation using instantaneous streamwise velocity field to demonstrate domain setup for SR transition- Vertical lines demarcate key regions in the flow; dark shaded zone represents recycled inflow development, vertical dotted line denotes location of SR transition, S denotes smooth wall, R denotes constant roughness region. Note that true extent of $z/\delta_{in} = 8.0$. Not to scale.

$W(\eta)$ is a weighting function detailed in Lund, Wu, and Squires [42]. The recycling method requires the momentum thickness θ and the friction velocity u_τ to form (5.4)

$$\frac{u_{\tau,inlet}}{u_{\tau,rec}} = \left(\frac{\theta_{rec}}{\theta_{inlet}}\right)^{\frac{1}{2(n-1)}} \tag{5.4}$$

where subscript rec indicates the recycling plane and $n = 5$.

We denote the streamwise location of this transition x_{SR} such that the roughness function is given by

$$\Delta U^+ = \begin{cases} 0, & x < x_{SR} \\ \frac{1}{\mathcal{K}_1}\log(1 + 0.26\frac{k_s u_\tau}{\nu}), & x > x_{SR} \end{cases} \tag{5.5}$$

The roughness parameter k_s is kept finite and constant in the rough section.

Rough-Smooth (RS): Recycling and bottom boundary

For the RS flow (visualised in figure 5.2), we use the fact that our analysis lies in the asymptotically rough regime when generating the recycled turbulent inflow. The recycling region $R(L)$ features a linearly increasing roughness measure $k_s = \alpha x$, for which it has been shown that u_τ must be a constant determined by the slope α [84], followed by a development region $R(C)$ with constant k_s. The formula used for the recycling method can thus be summarised as follows,

$$\phi_{in}^{inn} = \phi_{re}^{inn}, \quad \phi_{in}^{out} = \phi_{re}^{out}, \tag{5.6}$$

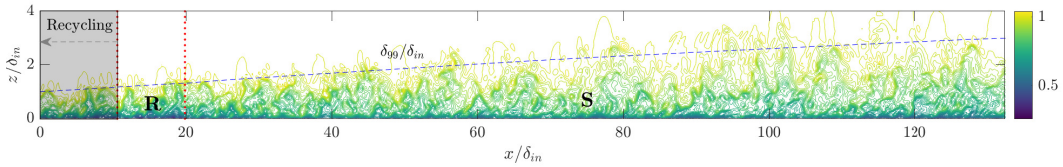

Figure 5.2: Schematic of computational setup for *RS* flow - Vertical lines demarcate key regions in the flow; dashed vertical line represents recycling plane, $R(L)$ denotes fully rough-wall with linearly increasing roughness, $R(C)$ denotes fully rough wall with constant roughness k_s, S denotes smooth wall. Dashed line along horizontal coordinate emphasises rough regions. Note that true extent of $z/\delta_0 = 8.0$. Not to scale.

where ϕ denotes the velocity component, either the mean streamwise velocity $u(z)$, the mean wall-normal velocity $w(z)$, or three fluctuation components $u'(y,z)$, $v'(y,z)$ and $w'(y,z)$. The subscripts "in" and "re" for the inlet plane and recycling plane indicate the streamwise plane where velocity components are evaluated. The superscripts "inn" and "out" denote inner and outer scales respectively. This allows the boundary layer to develop slowly over the spatially increasing roughness from $k_s = 0$ at a virtual leading edge to the constant value used in the fully rough domain at the end of the recycling region. Previous investigations have shown that a return to equilibrium flow after *RS* transition is expected to occur over greater streamwise distances than *SR* transition [23, 3, 4]. Hence our domain is modified accordingly by adjusting the inlet boundary layer thickness such that x/δ_0 is larger than for the *SR* case.

$$\Delta U^+ = \begin{cases} \frac{1}{\mathcal{K}_1}\log(1 + 0.26\frac{k_s u_\tau}{\nu}), & x < x_{RS} \\ 0, & x > x_{RS} \end{cases} \tag{5.7}$$

Inner scaling is given by the law of the wall $z^+ = z/l^+ = zu_\tau$, whereas outer scaling is governed by the defect law using $\eta = y/\delta$. δ represents some measure of boundary layer thickness, and in this chapter, we distinguish between the 99% boundary layer thickness δ_{99} and the internal boundary layer δ_I. In this recycling method, velocity components are scaled by the inner measure u_τ.

5.4 Model validation

5.4.1 Equilibrium flows

We apply the SGS and wall model equations with the recycling technique (§ 5.3 and 5.3.2) to verify the computational framework against purely smooth and rough-walled flows in equilibrium. The roughness in this test case is homogeneous and isotropic sand-grain type roughness, constant k_s everywhere in the domain. The purely smooth and rough cases, being self-preserving forms of boundary layers, are less restrictive to the grid spacing than the transitional roughness cases.

Squire et al. [82] used a series of wind tunnel experiments to characterize the effect of roughness measure k_s^+ and Reynolds number $\delta_{99}^+ = \delta_{99} u_\tau / \nu$ on streamwise velocities and turbulence intensities over fully smooth and fully rough walls with random sand-paper roughness distribution. Their reported equivalent sand-grain roughness is $k_s = 1.96$mm. They observed outer layer collapse of streamwise velocity variance in rough wall flows for $\delta_{99}^+ \geq 14000$. They also present a novel method of determining the friction velocity u_τ which does not require the assumption of logarithmic behaviour in the mean velocity profiles. While a range of experimental conditions are reported, we target their fully smooth measurements at $Re_\tau = 9830$, and fully rough measurements at $Re_\tau = 13130$, $k_s^+ = 106$, with the results shown in figure 5.3. The flow conditions in the present LES have been iterated to match these parameters closely. In both the smooth and rough wall cases, the expected value for U_∞^+ and the log-layer behaviour are captured faithfully by the LES when compared with the experimental campaign of Squire et al. [82]. The simple model using the Hama roughness correction for ΔU^+ is shown to be able to capture the log-layer velocity deficit to a reasonable extent.

5.4.2 Grid sensitivity

Case	N_x	N_y	N_z	L_{SR}/L_x	L_x/δ_0	L_y/δ_0	L_z/δ_0
$V1$	512	192	96	0.35	80	13.2	8.0
$V2$	768	256	128	0.35	80	13.2	8.0
$V3$	960	320	160	0.35	80	13.2	8.0

Table 5.1: Summary of parameters for grid resolution verification. $k_s^+ = 55$, $Re_\tau = 18000$

The sensitivity of the numerical solution to changes in grid resolution is studied using SR transition as the canonical flow. We investigate the grid independence of the solution by considering skin friction, and mean velocity profiles at streamwise

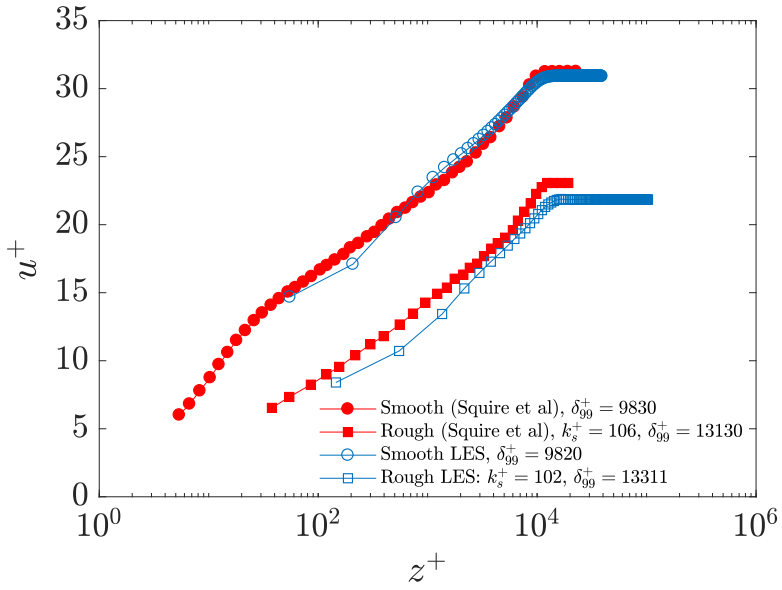

Figure 5.3: Comparison of mean velocity profiles in uniformly smooth and rough flows against experiments of Squire et al. [82]

stations immediately upstream, and a few boundary layer thicknesses downstream of the roughness transition, since experimental evidence from Antonia and Luxton [3] and Efros and Krogstad [23] suggests that this represents the region with the highest streamwise gradients. We test our code against the *SR* transition case, as this is expected to have higher streamwise gradients than the *RS* transition case, and hence is more restrictive.

While we do not define a strict, or formal measure of the order of grid convergence in LES, we use successively finer grid resolutions referred to as $V1$, $V2$ and $V3$ summarised in table 5.1 to verify that any differences in flow statistics are sufficiently small and inconsequential to the overall results. Figures 5.4 and 5.5 present evidence of a sufficiently converged grid resolution for the purposes of a detailed study of the wall-roughness transition problem using the LES framework described in §5.3. The maximum discrepancy in U_∞^+ is shown to be 2.9% for the cases considered. Perhaps most importantly, good agreement is shown in figure 5.4 when comparing the peak values of the C_f overshoot between the different cases. Based on the results, we choose case $V2$ as our grid for detailed computations. We note a near wall effect in the first three wall-normal points in the mean velocity profiles shown in figure 5.3. Good agreement is still observed in the log-layer velocities and the peak skin friction at similar Re. we again show these points in 5.5, where we compare the

mean velocities in the fully smooth, and developing rough-wall flows for cases $V1$, $V2$ and $V3$, but do not discuss them in greater detail in the results that follow.

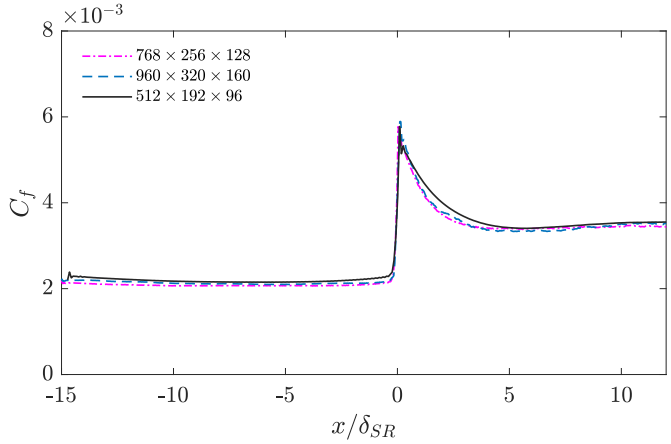

Figure 5.4: Grid resolution effect on streamwise development of skin-friction in SR transition. $k_s^+ = 55$, $Re_\tau = 18000$.

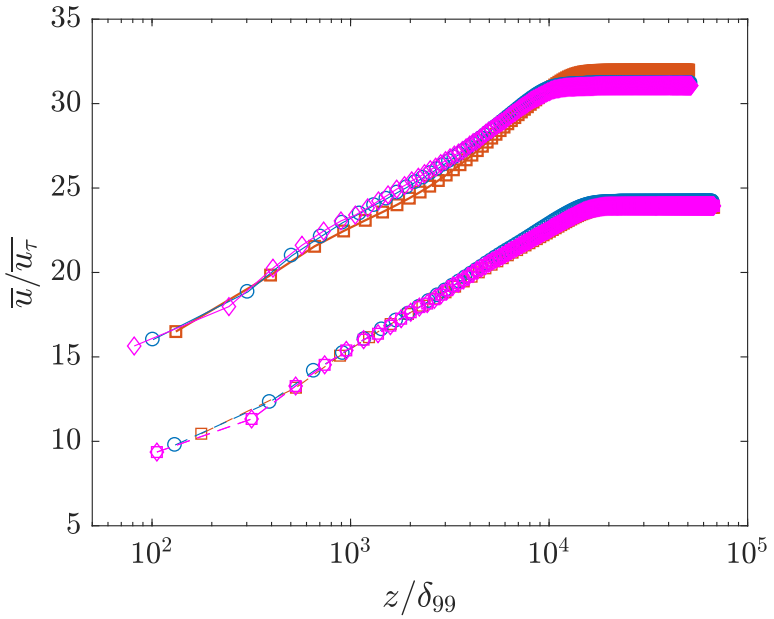

Figure 5.5: Grid resolution effect on streamwise development of mean velocity profiles in SR transition. $k_s^+ = 55$, $Re_\tau = 18000$. Dashed lines represent rough wall flow at $x/\delta_{SR} = 10.9$, solid lines represent smooth wall flow at $x/\delta_{SR} = -2.75$. Symbols represent resolution cases - square: V1; circle: V2; diamond: V3.

5.5 Results: Smooth to rough (SR) transition

5.5.1 Summary of LES parameters

In this section we present the results from simulations of turbulent boundary layer flow with an abrupt SR change in the surface condition. A summary of the simulation parameters is presented in table 5.2. The values of $k_s^+ = k_s u_\tau/\nu$ reported are taken with u_τ immediately upstream of the roughness transition. We note that $k_s^+ > 100$ for all cases considered, thus the results presented here are valid in the asymptotically rough regime. All detailed results presented in this section, including figures, are with respect to case $S0$ for brevity. The qualitative trends in streamwise development described herein for case $S0$ also apply to cases $S1$ and $S2$. We summarise the parameter set studied in the SR transition case in table 5.2 and focus our computational study on the effect of increasing Re_τ while maintaining constant k_s, such that k_s^+ immediately upstream of the transition agrees to within 2.4%. In the results that follow we shift the origin and define $x/\delta_{SR} = 0$ at the SR transition.

Case	Re_τ	k_s^+	δ_{99}/k_s	x/δ_{in}	y/δ_{in}	z/δ_{in}	L_{rec}/δ_{in}	$L_{S\to R}/\delta_{in}$
S0	2.8×10^4	131	214	80	13.2	8.0	14.4	28
S1	8.4×10^4	128	644	80	13.2	8.0	14.4	28
S2	1.3×10^5	128	1218	80	13.2	8.0	14.4	28

Table 5.2: Summary of LES parameters for SR transition. δ_{in} is the 99% boundary layer thickness at the inlet plane

5.5.2 Skin-friction

The skin friction coefficient C_f and dimensionless friction velocity $U_\infty^+ = U_\infty/u_\tau$ are shown in figures 5.6a and 5.6b. Also shown are the Coles-Fernholz 2 empirical fits for each of the cases, calculated as a function of $Re_\theta = U_\infty\theta/\nu$ as compiled by Nagib, Chauhan, and Monkewitz [55]

$$C_f = 2\left[\frac{1}{\kappa}\log(Re_\theta) + C\right]^{-2} \tag{5.8}$$

where $\kappa = 0.384$ and $C = 4.127$. The spanwise averaged momentum thickness is determined at every streamwise location from the numerically calculated velocity fields, which allows us to determine $Re_\theta = U_\infty\theta/\nu$. ΔU^+ is calculated using (5.1), and is non-zero for $x/\delta_{SR} > 0$ due to constant k_s in this region. In figure 5.6a the skin-friction $C_f = 2\tau_w/(\rho U_\infty^2) = 2/U_\infty^{+2}$ with $u_\tau^2 = \tau_w/\rho$ first deviates from the reference self-preserving smooth-wall value around five boundary layer thicknesses upstream of the transition location denoted by $x/\delta_{SR} = 0$, where δ_{SR} is the thickness of the boundary layer at the location of the abrupt change in surface roughness. A

gradual decrease in skin friction in figure 5.6a (conversely an increase in U_∞^+ in figure 5.6b) is shown leading up to a prominent overshoot in C_f at $x/\delta_{SR} = 0$, followed by an undershoot when compared with the equilibrium rough-wall value at matched k_s^+. C_f subsequently relaxes to the equilibrium rough-wall value several boundary layer thicknesses downstream. The downstream distance at which C_f relaxes to the equilibrium rough-wall values shows a dependence on Re_τ and is quantitatively studied in §5.5.6. Efros and Krogstad [23] studied the development of the boundary layer with a smooth-rough wall boundary transition with particular focus on changes in outer layer structure. The present LES model is not applied in direct comparison to their experimental observations at $Re_\tau = 4500$ where its efficacy is somewhat compromised. Thus, the focus in the present study is on moderate to high Reynolds numbers.

5.5.3 Mean velocities and defects

Inner scaled velocity profiles $u^+ = \overline{u}/\overline{u_\tau}$, where the $\overline{(\quad)}$ represents spanwise averaged quantities (presently with no time averaging), are plotted against the inner scaled wall-normal coordinate $z^+ = zu_\tau/\nu$, firstly for $x/\delta_{SR} < 0$ in figure 5.7 followed by the non-equilibrium development for $x/\delta_{SR} > 0$ in figure 5.8, with sub-figures 5.8a and 5.8b showing profiles at multiple streamwise stations with $0 \leq x/\delta_{SR} \leq 4.49$ and $x/\delta_{SR} \geq 4.49$ respectively. Examining the upstream smooth-wall velocity profiles presented in figure 5.7 indicates that the LES with SV-SGS and wall-modelling is more consistent with the theoretical log-law prediction at higher Reynolds numbers. This effect is consistent with previous smooth-wall investigations using this particular SGS wall-modelling approach [31]. We note a near wall effect in the first three grid points adjacent to the bottom wall. In figure 5.8a, the mean velocity profile log-region exhibits an immediate departure in the non-equilibrium rough-wall flow from the $\kappa = 0.384$ line. Figure 5.8b shows that the flow gradually relaxes towards the equilibrium rough flow condition and develops a log-region corresponding to $\kappa \approx 0.384$.

Outer scaled velocity profiles in the developing region are also shown in figure 5.9. We see that approaching the fully-rough and fully-smooth limits essentially forms an envelope within which the developing flow lies, and provides a method of assessing the internal boundary layer by considering the merging points of two adjacent mean velocity profiles as discussed by Chamorro and Porté-Agel [8] and Antonia and Luxton [3]. We also consider the velocity defect as a measure of the flow relaxation to the downstream fully-rough state. The inner scaled velocity defect reveals, in

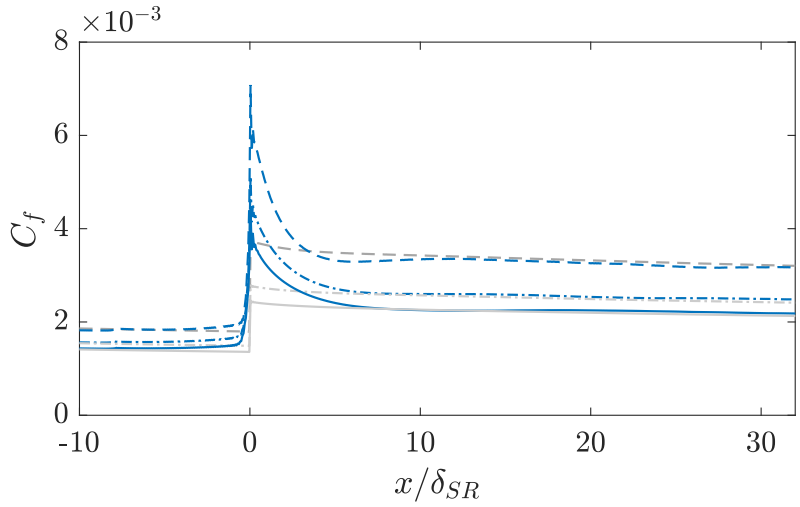

(a) Skin-friction coefficient C_f

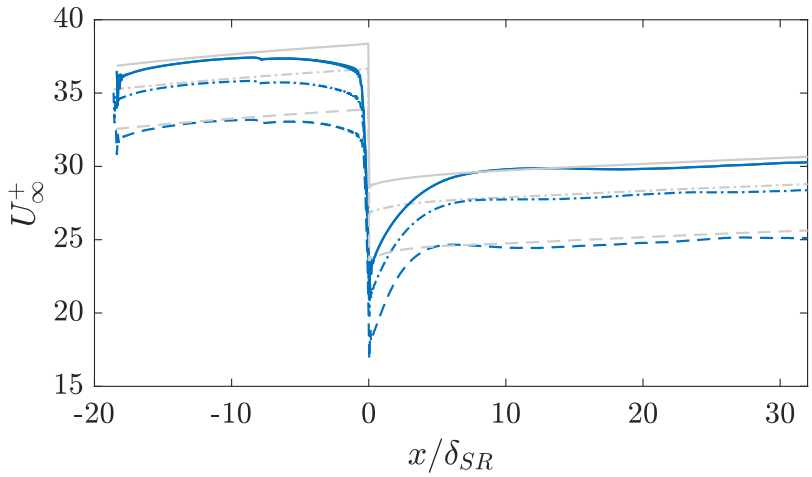

(b) Non-dimensional friction velocity U_∞^+

Figure 5.6: Skin-friction and friction velocity parameter U_∞^+ in SR transition. Line descriptions: dashed = $S0$; dash-dotted = $S1$; solid = $S2$. Cases identified in Table 5.2. Solid lines are theoretical curves from Nagib, Chauhan, and Monkewitz [55] Coles-Fernholz 2 fit (equation (5.8)) with the Colebrook roughness correction ΔU^+ from (equation (5.1))

figure 5.10b, departure from a collapse against z/δ_{99} between $0.15 \leq \delta_{99} \leq 0.6$ in the developing region downstream of the *SR* surface change.

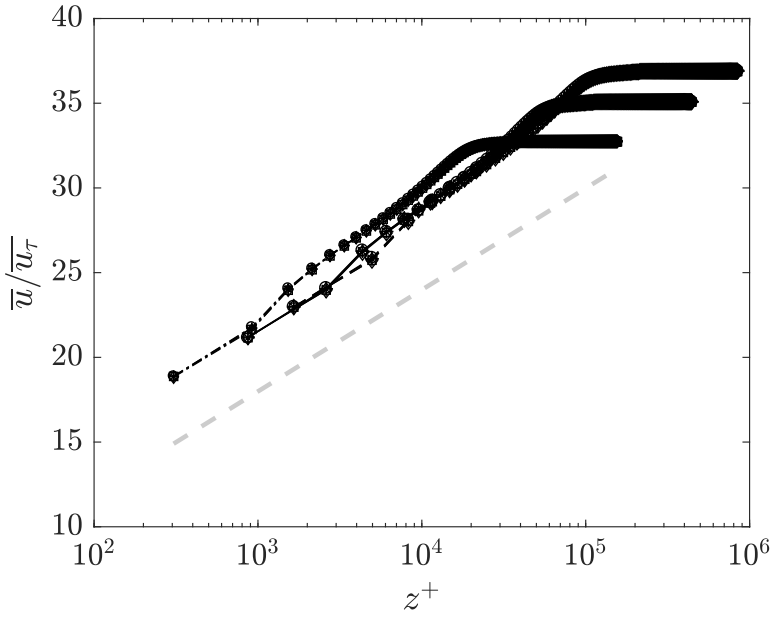

Figure 5.7: Reynolds number dependence of mean velocity profiles in LES (*SR* case shown here). Cases summarised in Table 5.2. Lines indicate smooth-wall profiles at varied Re_τ. Station symbols, in x/δ_{SR} units: circle: -6.5; plus: -6.1, star: -5.6; square: -5.3, diamond: -4.9. Lines indicate Re_τ range. Cases S0, S1, S2 in order of increasing $\overline{u}/\overline{u_\tau}$. Dashed grey line shows $\kappa = 0.384$ in log-wake law.

5.5.4 Turbulence intensities

We note that the first three grid-points nearest to the slip wall at $z = h_0$ in the computational domain display a near wall effect due to the implementation of the SV SGS modelling technique. Hence we display, but neglect these points in the results and discussions that follow. Streamwise Reynolds stresses $\overline{u'^{+2}}$ scaled by the local $u_\tau \equiv \overline{u_\tau}$ values are presented at various streamwise stations in figure 5.11. In figure 5.11a, for $x/\delta_{SR} < -5$, the turbulent stresses are shown to collapse against z/δ_{99}, confirming fully developed smooth-wall flow. The upstream influence of the rough wall condition is observed thereafter at the $x/\delta_{SR} = -0.32$ station, with lower normalised Reynolds stresses than the smooth wall flow. Immediately downstream of the *SR* jump, for $x/\delta_{SR} > 0$ we expect u_τ to increase as shown in §5.5.2. Thus the turbulence levels normalised by the locally calculated u_τ^2 rapidly decrease near the location of transition. A rapid decrease following the initial overshoot in turbulence levels normalised by u_τ^2 is observed in figure 5.11b immediately downstream of

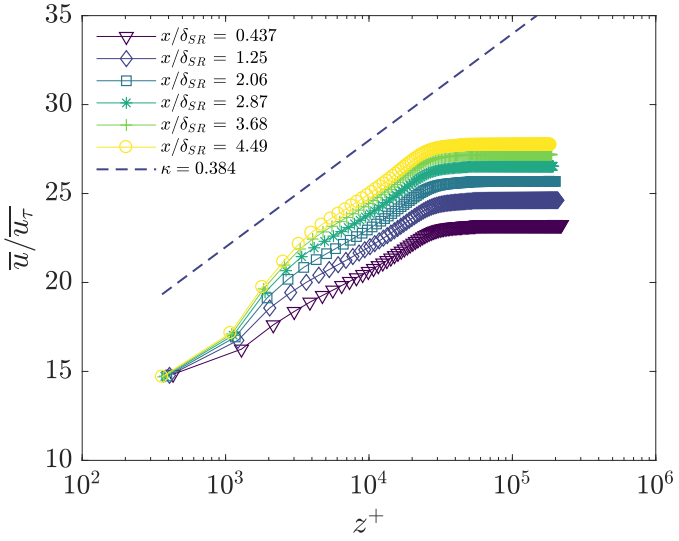

(a) Developing flow, downstream stations with $x/\delta_{SR} \leq 4.49$

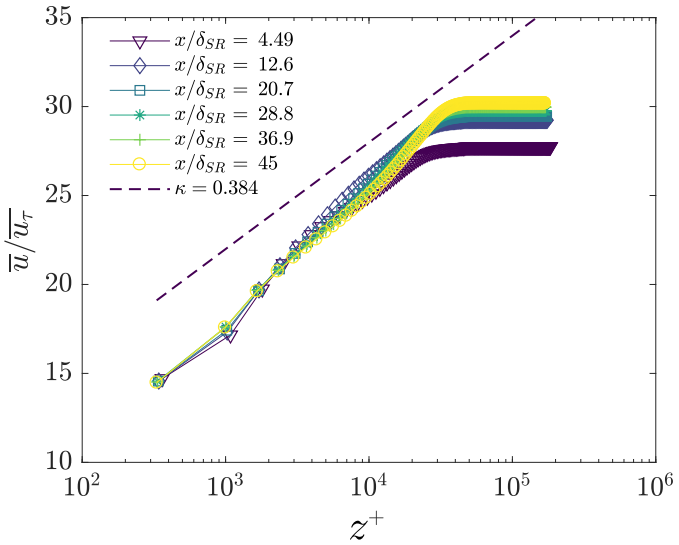

(b) Downstream stations with $x/\delta_{SR} \geq 4.49$

Figure 5.8: Mean velocity development downstream of *SR* wall transition; Case *S*0 examined in detail.

the *SR* surface change, where u_τ overshoots the equilibrium rough-wall value, followed by a merging of the inner and outer distributions of the Reynolds stress towards the equilibrium rough-wall state. The increasing trend in the merging point z/δ_{99} suggests that the increasing turbulence level due to wall roughness is gradually transported perpendicular to the wall until the entire flow exhibits turbulence stresses consistent with the rough-wall flow. We quantify this systematically using the

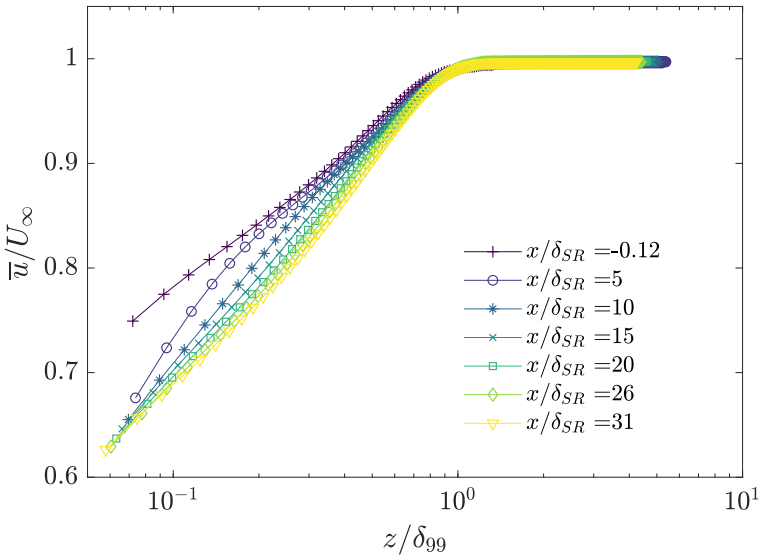

Figure 5.9: Outer scaled spanwise averaged velocity profiles $\overline{u}/U_\infty$ plotted against z/δ_{99} in SR transition. Case $S0$. Symbols indicate streamwise progression.

internal boundary layer in the following section. Previous studies of smooth-walled TBL with the SV-SGS and wall-modelling technique have shown that the log-layer slopes in streamwise turbulent intensities appear flatter than values observed in experiments at comparable Re_τ [31].

We compare our results to the experimental data of Efros and Krogstad [23] in SR flow in figure 5.12 to demonstrate that the present LES captures the structure of the turbulence reasonably well. An interesting observation from their results is that the stress ratios between rough and smooth walls are comparable in the outer layer, with major differences in the ratio of turbulent stresses noted at distances of $z/k = 2$ to 4. Given the implementation of the wall-model and the near-wall effect in the LES, we are unable to comment directly on the turbulent stress ratios at these wall normal distances.

5.5.5 Internal boundary layer growth

The internal boundary layer (IBL), denoted herein by $\delta_I(x)$ serves as a demarcation in the wall-normal extent of the flow affected by the modified roughness condition. We consider two possible representations of the internal boundary layer growth. The first considers the method of Efros and Krogstad [23] based on streamwise velocity intensities, while the second utilizes a method of merging velocity profiles similar to that suggested by Antonia and Luxton [3], who plotted profiles against a

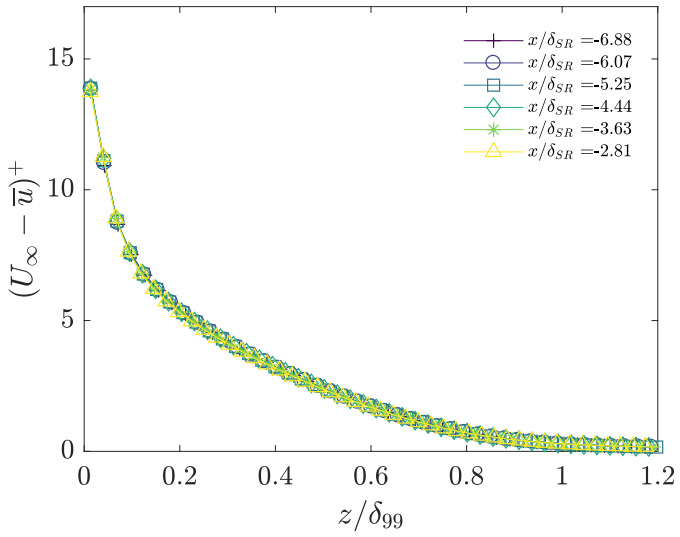

(a) Fully smooth region

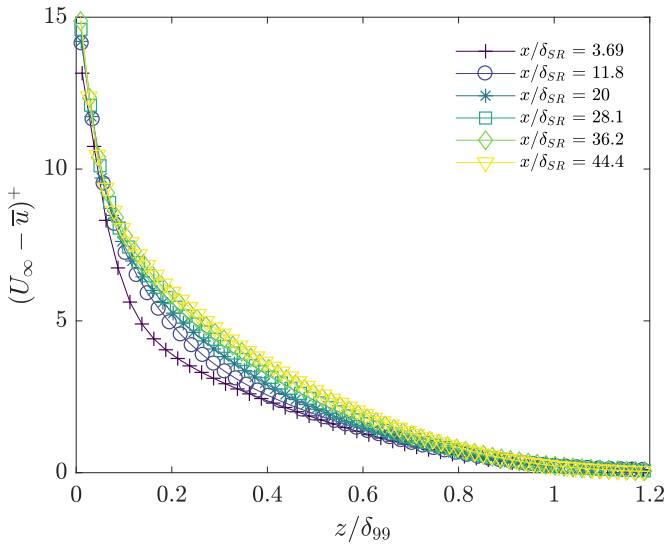

(b) Transitionally rough region

Figure 5.10: Development of velocity defect downstream of SR transition. Downstream progression in x/δ_{SR} is represented with lighter line colours and the symbol key embedded in the figures.

$z^{1/2}$ scaling using the following the SR transition based on dimensional arguments.

Inner-layer growth determined from $\overline{u'^{+2}}$ profiles

This method itself defines two related measures of internal-layer growth

$$\frac{\delta_I(x)}{\delta_{99}(x)} = A_1\left(\frac{x}{\delta_{SR}}\right)^{b_1} \tag{5.9}$$

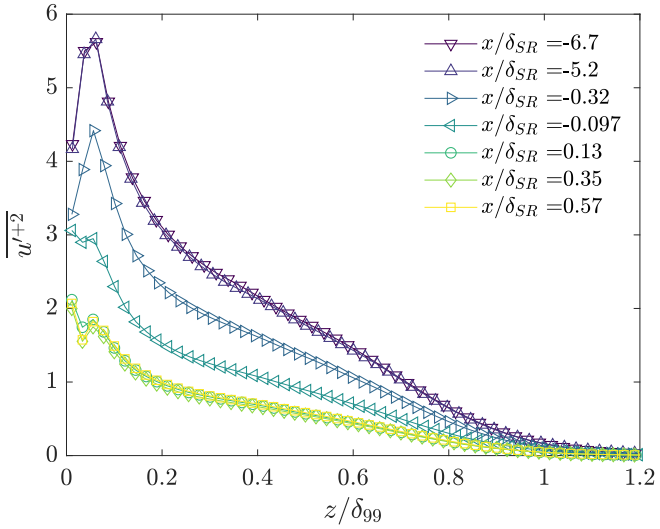

(a) Reynolds stress profiles in the immediate vicinity of the SR transition. Case $S0$

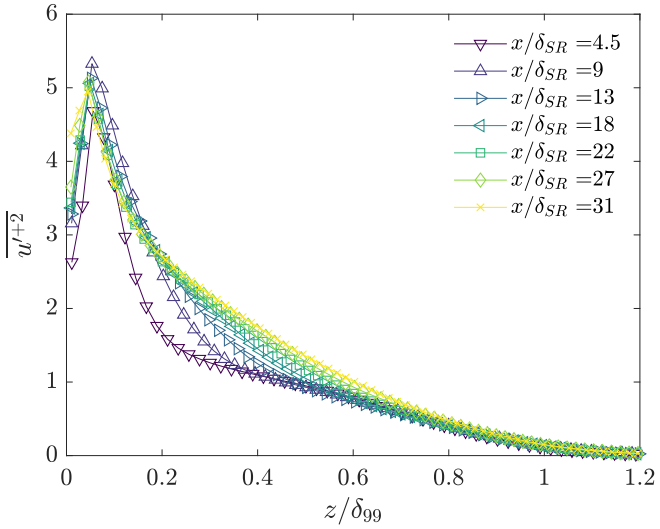

(b) Transitionally rough region

Figure 5.11: Development of streamwise Reynolds stresses near SR transition. Case $S0$. Downstream progression is represented with lighter line colours.

$$\frac{\delta_I(x)}{\delta_{SR}} = A_2\left(\frac{x}{\delta_{SR}}\right)^{b_2} \tag{5.10}$$

where $\delta_{SR} = \delta_{99}$ at the origin. In (5.9) $\delta_{99}(x)$ is incorporated, while in the second in (5.10) the absolute growth $\delta_I(x)/\delta_{SR} = A_2(x/\delta_{SR})^{b_2}$ is recognised. The dimensional form, such that $\delta_I \propto x^b$ is reported by Antonia and Luxton [3, 4] and Efros and Krogstad [23].

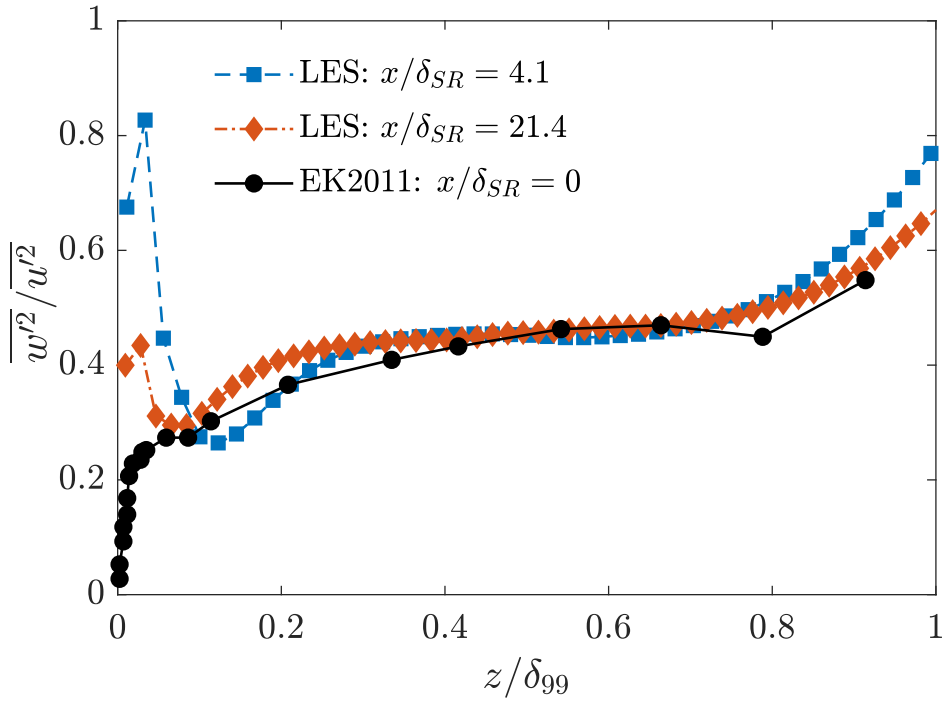

Figure 5.12: Comparison of turbulent stress ratios, wall-normal and streamwise components $\overline{w'^{+2}}/\overline{u'^{+2}}$ with experimental results of Efros and Krogstad [23].

To define the extent of the internal boundary layer and determine the coefficients A_1, A_2, b_1, b_2, we first consider the method proposed by Efros and Krogstad [23], who locate a 'knee' point in the $\overline{u'^{+2}}$ wall-normal profiles using the intersection of linear, least squares fits to the inner and outer regions at multiple stations to define $\delta_I(x)$. Figure 5.13 demonstrates Efros and Krogstad's method with the present result from Case *S*0 at four streamwise stations. For a particular profile at a given x/δ_{SR} (where $x/\delta_{SR} = 0$ corresponds to the location of roughness transition) we visually identify the inner and outer distributions of the $\overline{u'^{+2}}$ profiles. For the *SR* transition, the inner layer will exhibit higher turbulence stresses such that $\partial\overline{u'^{+2}}/\partial(z/\delta_{99})$ has a greater absolute slope. Several points are then selected by defining the inner and outer layer bounds with respect to z/δ_{99}. We exclude points very near the wall, near the blending region, and points near the outer limit δ_{99} of the boundary layer. Least-squares, straight line fits are then calculated for each region, and the point of intersection of the two lines defines the edge of the internal boundary layer at the given x/δ_{SR}. From this method we obtain values of δ_I/δ_{99} at several streamwise locations x/δ_{SR}. Corresponding values for δ_{99}/δ_{SR} and the absolute IBL edge $\delta_I(x)$ are also recorded and are directly obtainable from the LES. Figure 5.14

summarises the IBL growth rates normalised by δ_{SR} with the parameters stated in table 5.2. Experimental data from Antonia and Luxton [3] and Efros and Krogstad [23] suggests the validity of a power-law growth of δ_I, hence we fit power law curves using a least squares approximation to the IBL for the SR case. We report both growth rates δ_I/δ_{99} and δ_I/δ_{SR} in table 5.3.

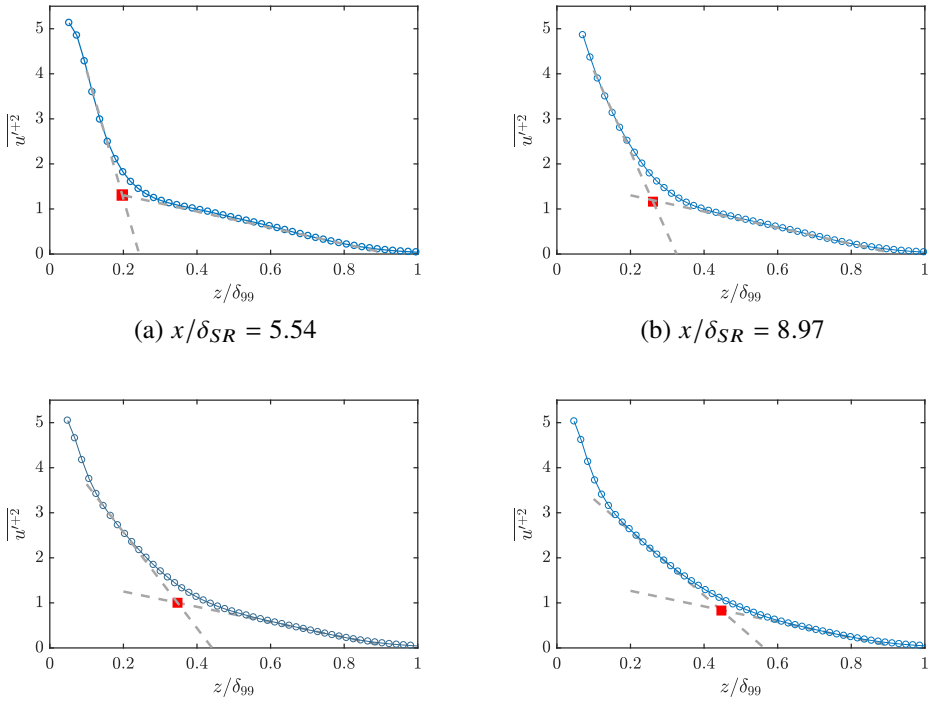

(a) $x/\delta_{SR} = 5.54$ (b) $x/\delta_{SR} = 8.97$

(c) $x/\delta_{SR} = 12.41$ (d) $x/\delta_{SR} = 15.84$

Figure 5.13: Determination of internal boundary layer position via method described by Efros and Krogstad for SR transition. (a)-(d) indicate downstream progression. Dashed lines show inner and outer slopes. Filled squares mark intersection of inner and outer slopes at the known x/δ_{SR} station, and therefore determines δ_I/δ. Case $S0$.

Internal boundary layer growth using merge points of outer-scale normalised velocity profiles

To define a measure of 'merging' between adjacent velocity profiles, we consider the outer scaled velocity defect $D = (U_\infty - \overline{u})/U_\infty = 1 - \overline{u}/U_\infty$, where U_∞ is constant. We consider $D = D(z/\delta_{99}, x/\delta_{SR})$ with x dependency only in the second independent variable. The quantity $\partial D/\partial x$ with z/δ_{99} fixed can then be defined and depends also on $z/\delta_{99}, x/\delta_{SR}$. From the LES, the discrete difference between adjacent stations is calculable, providing an approximation proportional to $\partial D/\partial x$.

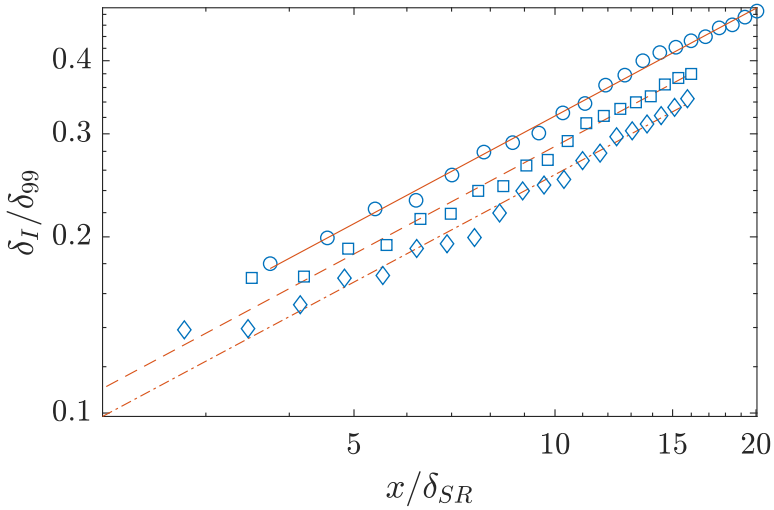

(a) Growth of IBL δ_I/δ_{99}

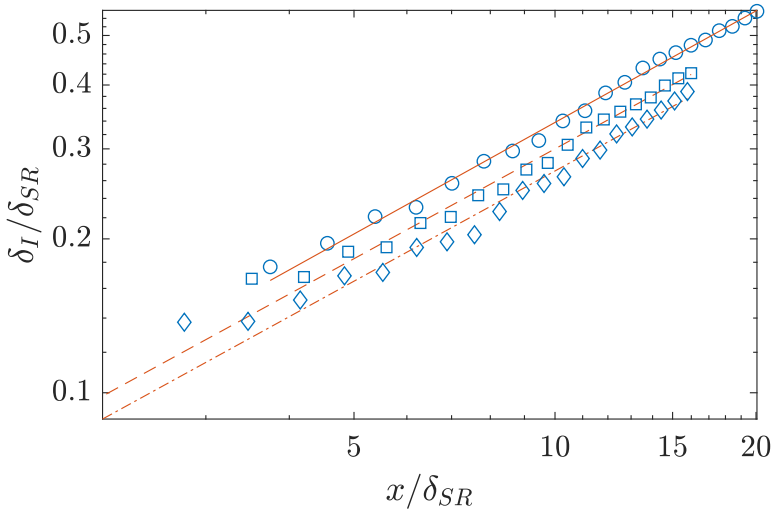

(b) Growth of IBL δ_I/δ_{SR}

Figure 5.14: Internal boundary layer thickness measures in SR flow inferred from identification of inner and outer regions in streamwise Reynolds stress plots detailed in §5.5.5. Symbols are from LES, lines are least square power-law fits shown in table 5.3. Circles and solid line: S0; squares and dashed line: S1, diamonds and dash-dotted line: S2.

Considering adjacent equispaced streamwise stations with indices denoted by n and $n+1$, we have $D_{n+1} - D_n = (\overline{u}_n - \overline{u}_{n+1})/U_\infty$. Our interest is in the merging point between adjacent outer scaled velocity profiles, so defining the relative change in D, defined by $D_r = (\overline{u}_n - \overline{u}_{n+1})/\overline{u_n}$ allows identification (within some tolerance margin) of values of z/δ_{99} at which the merger effectively occurs as the isoline $D_r = 0$ in

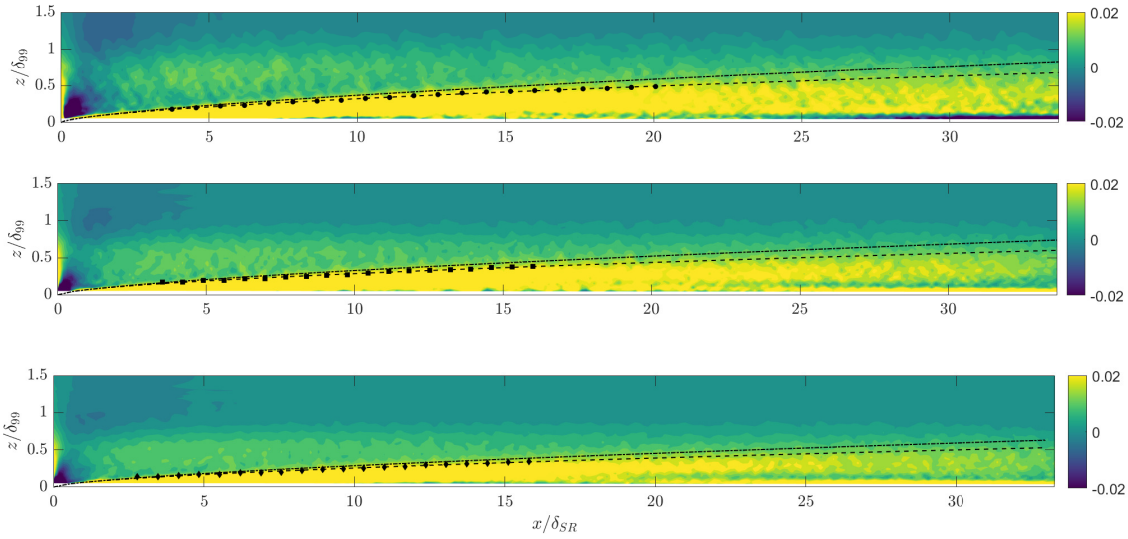

Figure 5.15: Contour plots of $D_r(x/\delta_{SR}, z/\delta_{99}) = (\overline{u_n} - \overline{u_{n+1}})/\overline{u_n}$ where n denotes streamwise station index, SR flow. Percentage change in mean velocity profiles in x/δ_{SR}. Symbols and dashed lines reproduce non-dimensional power law curves shown in figure 5.14a. Top to bottom indicates cases $S0$, $S1$, $S2$. Dash-dotted line indicates 10% increment in power law exponents. First three wall-normal points omitted due to near wall effect.

the $z/\delta_{99} - x/\delta_{SR}$) plane. We consider this a useful method of determining the IBL since it does not require a known 'reference' field at the same Re (which, while obtainable computationally, is potentially difficult to secure in practical situations particularly at atmospheric scales). In practice a tolerance of 0.02% is used to capture numerical effects. We note that the inner scaled velocity defects $U_\infty^+ - u^+$ provides a more universal collapse of mean velocity profiles over both rough and smooth walls. But if this measure is used, it is found that the sharp overshoot in u_τ immediately downstream of $x/\delta_{SR} = 0$ appears to mask the merge zone over $x/\delta_{SR} < 5$ (contours of the inner scaled deficit are presently not shown). Hence we consider the outer scaled relative velocities a more robust visualisation of the internal boundary layer growth.

Color-contours of D_r are plotted for the SR transition in figure 5.15 where figures 5.15a, 5.15b and 5.15c correspond to cases $S0$, $S1$ and $S2$ respectively. The contours identify constant levels of D_r as a function of z/δ_{99} and x/δ_{SR}, and therefore provide a measure of the IBL growth in a similar sense to Antonia and Luxton [3] with their velocity profile 'merge' method. A brief investigation into the sensitivity of δ_I to this

Case	Re_τ	k_s^+	A_1	b_1	A_2	b_2
S0	2.8×10^4	131	0.085	0.60	0.066	0.728
S1	8.4×10^4	128	0.069	0.61	0.058	0.714
S2	1.3×10^5	128	0.062	0.61	0.052	0.716

Table 5.3: Parameters for power-law fit to internal boundary layer in smooth-rough transition. $\delta_I/\delta_{99} = A_1(x/\delta_{SR})^{b_1}$ and $\delta_I/\delta_{SR} = A_2(x/\delta_{SR})^{b_2}$

subjective tolerance suggests that a 25% variation does not result in an appreciable difference in the location of the IBL. A direct comparison with δ_I/δ_{99} obtained from (5.9) with A_1, b_1 from table 5.3 is also included in the in the contour plots, suggesting a good match between the two methods while noting a general trend of under predicted δ_I/δ_{99} with the knee point method. Antonia and Luxton [3] observed a notable difference when considering the IBL growth rates with each of the two methods. An upper bound, such that the power-law exponent is 10% greater than that determined by the knee-point method is also included to emphasize the effect of the exponent on the apparent relaxation distance.

5.5.6 Relaxation length

We now estimate measures of the relaxation length, defined as the streamwise length from the SR transition, to the approximate streamwise station where the boundary layer has reached a fully rough-wall equilibrium state. Two such measures are considered, the first from the streamwise relaxation of C_f to downstream rough-wall equilibrium values at matched Re_τ and k_s^+, and the second from the IBL growth rates. For the skin-friction relaxation length we define $C_{f0}(x)$ as the reference skin-friction coefficient from LES of the fully rough-wall boundary layer using the roughness correction from equation (5.1) with matched Re_τ and k_s^+. We then compute the ratio $C_f(x)/C_{f0}(x)$ where $C_f(x)$ from the non-equilibrium LES. A ratio $C_f(x)/C_{f0}(x) = 1$ would indicate a perfect match between the non-equilibrium and equilibrium LES. Ratios for the three SR LES cases have been plotted in figure 5.16a. It can be seen from both figures 5.6a and 5.16a that the SR LES shows a small offset from unity towards the end of the plotted range. A local minimum value, interpreted as a slight undershoot, also appears as a distinctive feature of the $C_f(x)/C_{f0}(x)$ variation in all the SR cases.

In figure 5.16b, the correction to the friction velocity $U^+_{\infty,SR}$ obtained from the non-equilibrium LES required to match $U^+_{\infty,R}$ calculated from fully rough LES at matched Re_τ and k_s^+ is shown. We define a corrective term ΔU_c^+ in the non-equilibrium region

so that the free-stream velocity normalised by the friction velocity is given by the following form of the classical log-wake relation

$$U^+_{\infty,SR} = \frac{1}{\kappa}\left[\log\left(\frac{\delta_{99}u_\tau}{\nu}\right) + 2\Pi\right] - \Delta U^+(k_s^+) + \Delta U_c^+ + A. \tag{5.11}$$

In (5.5.6), setting $\Delta U_c^+ = 0$ returns the equilibrium values for normalised free-stream velocity $U^+_{\infty,SR} = U^+_{\infty,R}$ with ΔU^+ non-zero in the rough-wall region as defined in (5.1). To calculate the correction ΔU_c^+ at a given station x/δ_{SR}, $U^+_{\infty,SR}$ and the first term on the right-hand side are evaluated from the LES , $\Delta U^+(k_s^+)$ is computed from (5.1) with k_s^+ calculated from the LES and the constants $\Pi = 0.55$, $\kappa = 0.384$, $A = 8.5$ are used. All terms in except ΔU_c^+ are known and the latter can then be calculated. We then define $(x/\delta_{SR})_1$ to be the streamwise location at which $|\Delta U_c^+| = 0.01$ first occurs, neglecting the local maxima in ΔU_c^+ unique to the SR transition cases.

For the IBL measure, we put $\delta_I/\delta_{99} = 1$ in (5.9) and solve for $(x/\delta_{SR})_2$ as

$$\left(\frac{x}{\delta_{SR}}\right)_2 = \left(\frac{1}{A_1}\right)^{1/b_1} \tag{5.12}$$

These relaxation measures are summarised in table 5.4 for the three SR cases considered. We note that both measures of relaxation length have systematic sources of uncertainty. For the IBL measure, in obtaining (5.12) we are extrapolating (5.9) well beyond the range of the least-square fit shown in figure 5.14a. For the skin-friction estimates, subjective values of asymptotic zero-value estimates are used, introducing uncertainties in our results. Nonetheless, it is clearly evident from table 5.4 that the IBL relaxation length is consistently a factor of about five longer than the measure associated with relaxation of the skin-friction. This is probably because the streamwise velocity gradient at the wall is strongly conditioned by near-wall dynamics that reach local equilibrium relatively quickly. On the other hand the relaxation of the outer part of the boundary layer requires the dissipation of energetic turbulence produced by roughness and contained in very-long scale motions (VLSMs) [39]. According to the LES, this takes a surprisingly long streamwise length.

5.5.7 Effect of varied k_s^+ at matched Re_τ

We briefly present results from a study on the effect of k_s^+ on the relaxation of the skin-friction measure $(x/\delta_{SR})_2$ in our study. For this, the intermediate Re_τ case S1 has been used as the reference, and two values of k_s^+ in addition to the previously presented case (see Table 5.2) are included. Table 5.5 summarizes the

Case	Re_τ	k_s^+	$(x/\delta_{SR})_1$	$(x/\delta_{SR})_2$
S0	2.8×10^4	131	13	61
S1	8.4×10^4	128	18	77
S2	1.3×10^5	128	20	93

Table 5.4: Relaxation length estimates in SR transition: $(x/\delta_{SR})_1$ from recovery of skin-friction coefficient; $(x/\delta_{SR})_2$ from extrapolation of internal boundary layer power law curves in table 5.3

Case	k_s^+	$(x/\delta_{SR})_1$
S1L	48	18
S1	128	18
S1H	304	18

Table 5.5: Relaxation length estimates in SR transition: from skin-friction recovery measure

roughness conditions examined in this section. We note that the case denoted by $S1L$ includes a calculation in the transitionally rough regime. Figures 5.17a and 5.17b show the streamwise development of the skin-friction based relaxation measures. There is a noticeable trend of increasing peak C_f (overshoot relative to equilibrium rough value immediately downstream of the surface transition) with increasing k_s^+. Remarkably, the relaxation lengths in each instance at matched Re_τ remains approximately constant. Increasing k_s^+ increases the prominence of the local minimum in C_f/C_{f0}.

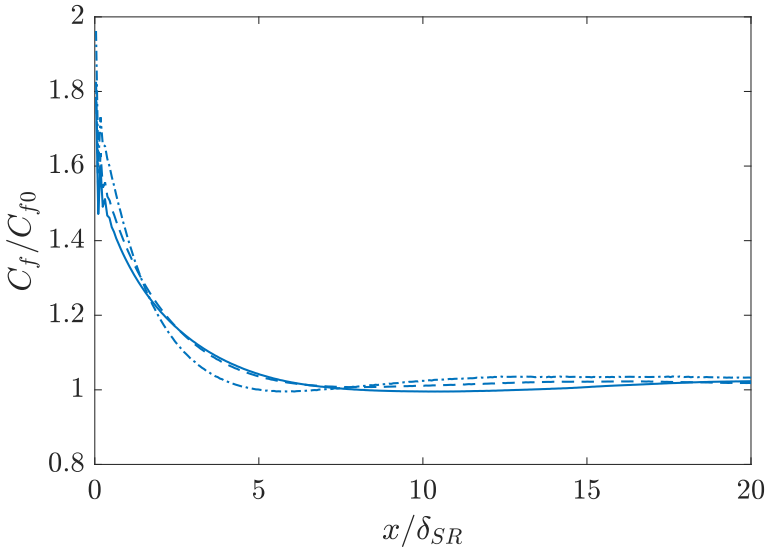

(a) Skin friction ratio, where C_{f0} is the rough wall equilibrium value

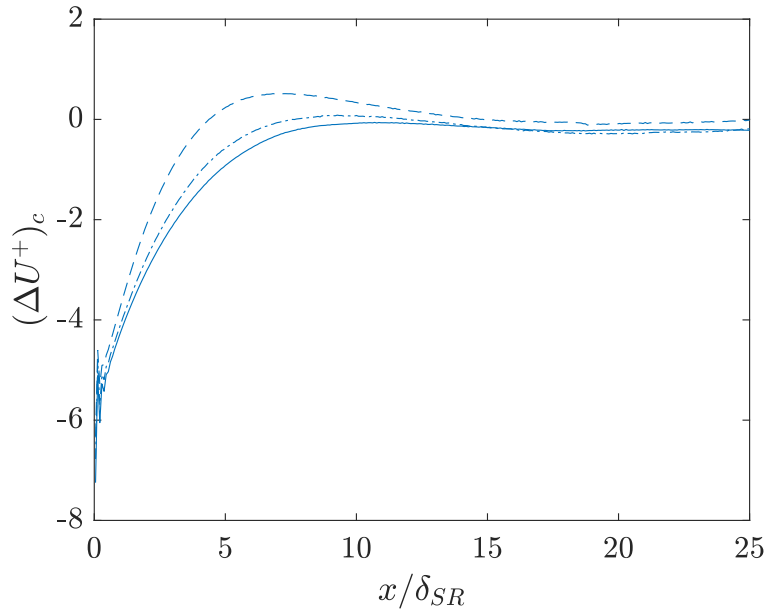

(b) Correction to ΔU^+ required to match LES friction velocity. $\Delta U^+ = 0$ represents equilibrium rough-wall value.

Figure 5.16: Relaxation measures for *SR* transition. Line descriptions: dashed = *S*0; dash-dotted = *S*1; solid = *S*2

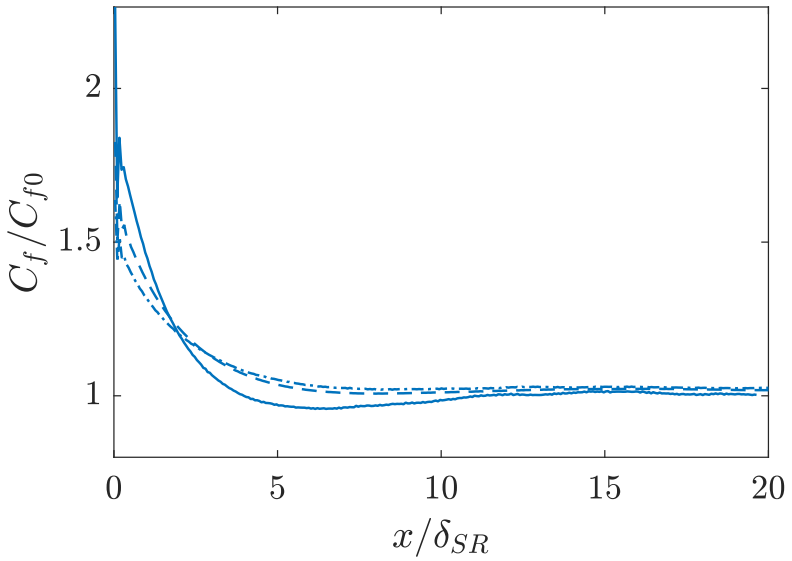

(a) Skin friction ratio, where C_{f0} is the rough wall equilibrium value

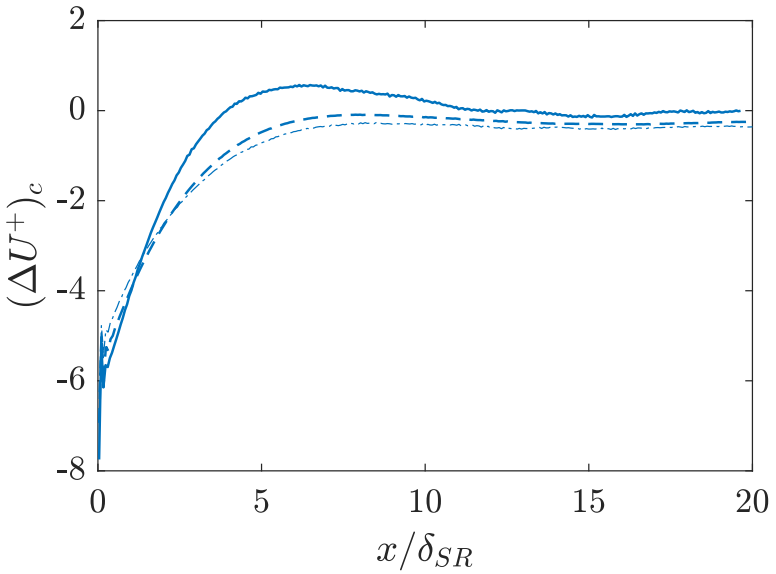

(b) Correction to ΔU^+ required to match LES friction velocity. $\Delta U^+ = 0$ represents equilbrium rough-wall value.

Figure 5.17: Relaxation measures for SR transition, examining k_s^+ effects. Line descriptions: dashed = $S1$; dash-dotted = $S1L$; solid = $S1H$

5.6 Results: Rough to smooth (RS) transition

5.6.1 Summary of LES parameters

We consider the case of RS wall transition using the computational domain described in §5.3.2 to study the streamwise development of the turbulent boundary layer from a fully-rough to a fully-smooth profile. The descriptions of fully-rough and fully-smooth flows are informed by self similarity in the variable z/δ_{99} in the streamwise development of Reynolds stresses in each of the distinct wall boundary regions, such that the entire wall-normal extent of the boundary layer has adjusted to the new wall condition. Detailed descriptions and flow statistics shown henceforth are focused on case $R0$. A summary of the RS numerical simulations has been included in table 5.6. We focus the computational study on constant k_s cases such that $k_s^+ = 115$ immediately upstream of the RS transition for a range of Re_τ between 1.8×10^4 to 8.8×10^4 as shown in table 5.6. The structure of this section closely follows that of the preceding section on SR flow development.

Case	Re_τ	k_s^+	δ_{99}/k_s	x/δ_{in}	y/δ_{in}	z/δ_{in}	L_{rec}/δ_{in}	$L_{R\to S}/\delta_{in}$
R0	1.8×10^4	115	144	133	22	13.3	10.67	20
R1	4.8×10^4	115	416	133	22	13.3	10.67	20
R2	8.8×10^4	115	1040	133	22	13.3	10.67	20

Table 5.6: Summary of parameters in RS simulations

5.6.2 Skin-friction

The skin-friction C_f and non-dimensional friction velocity U_∞^+ are considered as measures of streamwise development of RS non-equilibrium flow in figures 5.18a and 5.18b respectively. The LES in the RS section uses (5.7) for the roughness correction. We again plot both the results from the LES and the expected smooth and rough-wall values using (5.8) with the roughness correction given by (5.2). In figure 5.18a, the skin-friction is shown to undershoot the equilibrium smooth-wall value immediately downstream of the RS transition located at $x/\delta_{RS} = 0$, where $\delta_{RS} = \delta_{99}\big|_{x/\delta_{RS}=0}$. The skin-friction coefficients, and therefore the wall shear stress then gradually recover to the equilibrium smooth wall value between 12-24 x/δ_{RS}. A dependence on Re_τ is also apparent from the figures, and is addressed quantitatively in §5.6.6. The skin-friction in the recovered, or equilibrium smooth-wall flow appear to overshoot the equilibrium value calculated using the Coles-Fernholz empirical relation (5.8). Proceeding further downstream the rate of change of C_f appears consistent with that predicted by equation (5.8). Figure 5.18b presents the alternative representation of the skin-friction in terms of U_∞^+, as in §5.5.2. These parameters

show trends consistent with observed data in the experimental studies of boundary layers with streamwise heterogeneity in roughness [30, 4].

5.6.3 Streamwise development of mean velocities

Mean velocity profiles are plotted in inner scaled units for *RS* transition in figures 5.19a and 5.19b. Figure 5.19a shows that the velocity profiles for $x/\delta_{RS} < 0$ collapse against z^+. Immediately downstream of the jump at $x/\delta_{RS} = 0.497$, we observe, in figure 5.19b, an abrupt overshoot in u^+ across the vertical extent of the boundary layer. A comparison of figures 5.19a and 5.19b suggests that the non-equilibrium flow for $x/\delta_{RS} > 0$ departs from the expected slope of $\kappa = 0.384$ for equilibrium smooth and rough-wall flow. The jump in friction velocities, and therefore U_∞^+ is reflected in Figure 5.19. The results suggest that the upstream influence of the new smooth-wall condition is confined to $-2 < x/\delta_{RS} < 0$, in contrast to the *SR* case where the rough-wall influence is seen for approximately 5 x/δ_{SR} upstream. The *RS* transition exhibits slower development to the downstream wall condition than the *SR* cases. Beyond the initial abrupt undershoot, the velocity profiles gradually relax towards the equilibrium smooth wall value by $x/\delta_{RS} = 57$ as shown in figure 5.20.

Outer scaled velocity profiles are shown in figure 5.21, and demonstrate the gradual merging of profiles closer towards the smooth-wall profile downstream, this suggests one possible diagnostic tool for determining the extent of the internal boundary layer, similar to the *SR* cases. Velocity defects are shown in figures 5.22a and 5.22b and exhibit an overshoot with gradual relaxation with streamwise progression. The inner-scaled defect appears to adjust more rapidly to the equilibrium profile at $z/\delta_{99} > 0.4$. Mulhearn [54] studied mean velocity profiles and the influence of the relative positions of roughness crests to the downstream smooth wall origin at low *Re*. In this study the roughness geometry is not resolved directly and the effect of surface origin adjustment on velocity profiles is not discussed.

5.6.4 Turbulence intensities

The streamwise development of the turbulent intensities for case *R*0 (detailed in table 5.6) are shown in figures 5.23 and 5.24. Figure 5.23a and 5.23b focus attention on the immediate vicinity of the *RS* transition, whereas figure 5.24 emphasises the non-equilibrium nature of the developing smooth-wall flow. The upstream flow state is consistent with that of a fully-rough wall equilibrium flow, showing good collapse against the outer scaled wall-normal coordinate z/δ_{99}. The inner normalised

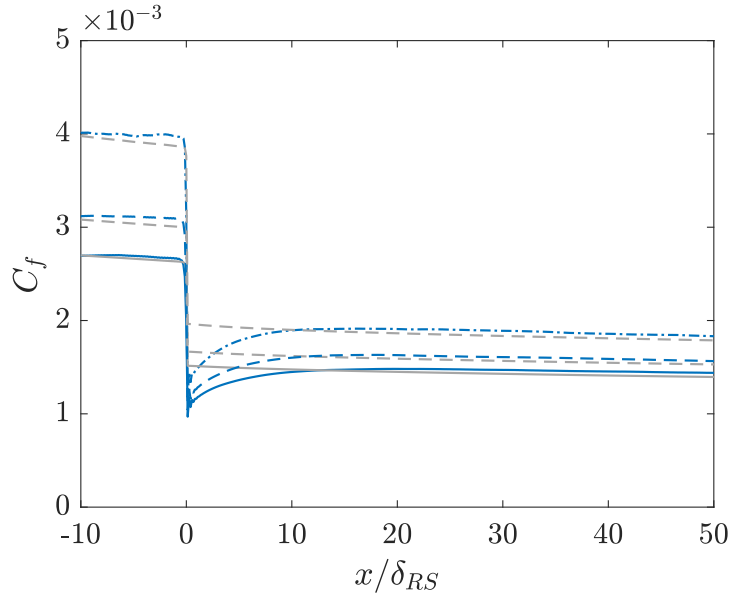

(a) Skin friction, C_f

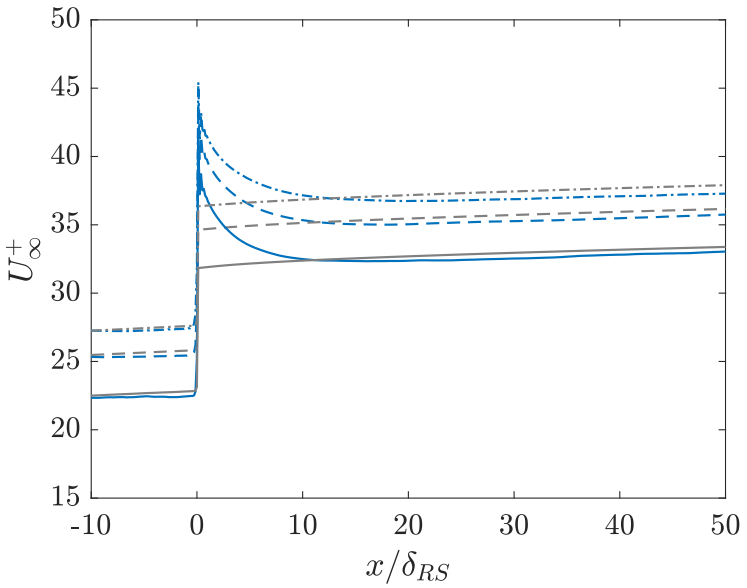

(b) $U_\infty/\overline{u_\tau}$

Figure 5.18: Skin friction, C_f, and non-dimensionalised friction velocity $U_\infty^+ = U_\infty/u_\tau$ in turbulent boundary layers with *RS* wall transition. Darker lines correspond to LES, while lighter lines correspond to theoretical values using Coles-Fernholz 2 (Nagib et al) (5.8) with the ΔU^+ equation (5.2) correction. Solid lines: Case R0, dashed lines: Case R1, dash-dotted lines: Case R2.

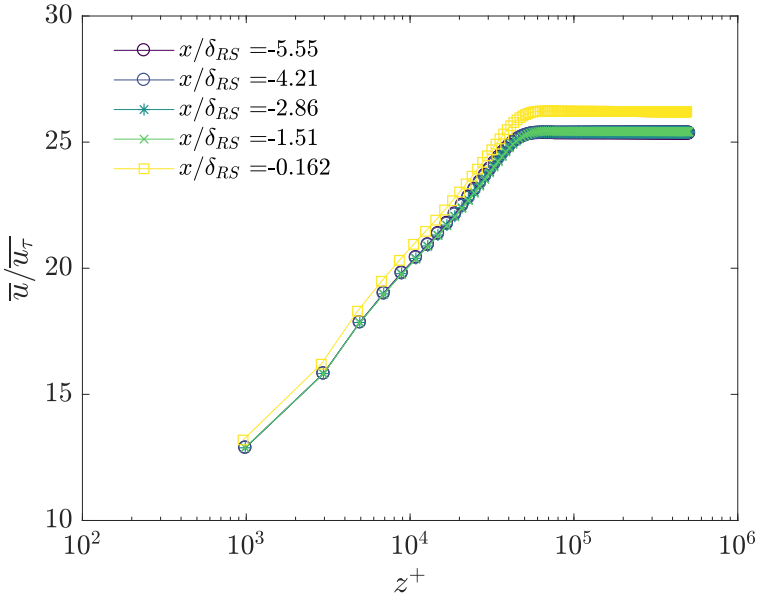

(a) u^+ for $x/\delta_{RS} < 0$

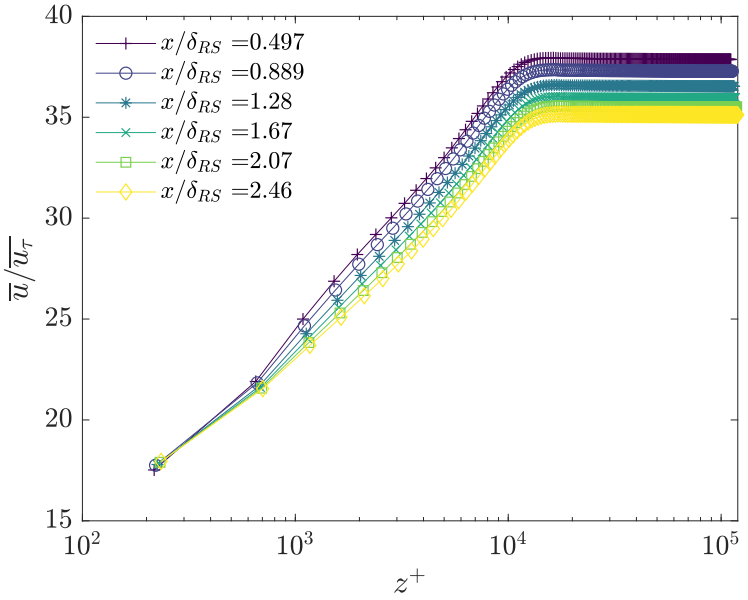

(b) u^+ for $0 \leq x/\delta_{RS} \leq 2.5$

Figure 5.19: Spanwise averaged, normalised velocities $u^+ = \overline{u}/\overline{u_\tau}$ in *RS* transition at near $x/\delta_{RS} = 0$. Symbols represent different streamwise stations described in the embedded key. Dark to light colour gradient indicates a downstream progression. Case *R*0.

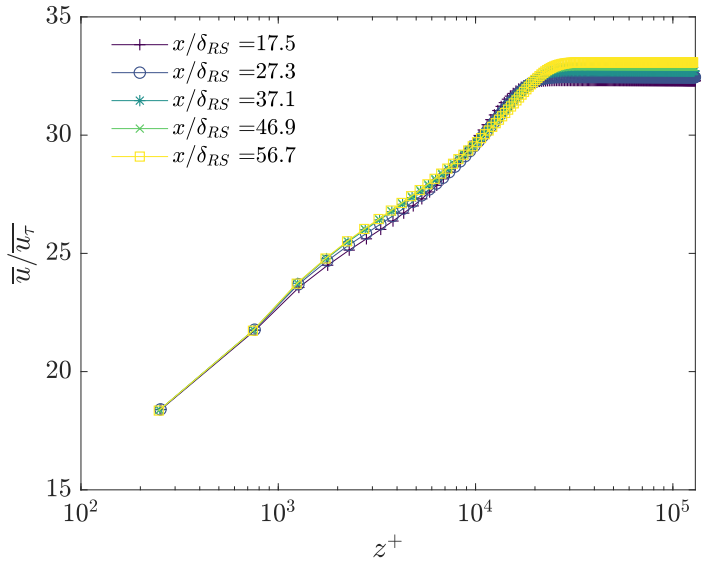

Figure 5.20: Spanwise averaged normalised velocities $u^+ = \overline{u}/\overline{u_\tau}$ in *RS* transition at large x/δ_{RS}. Embedded symbol key describes streamwise location at large x/δ_{RS}. Case *R*0.

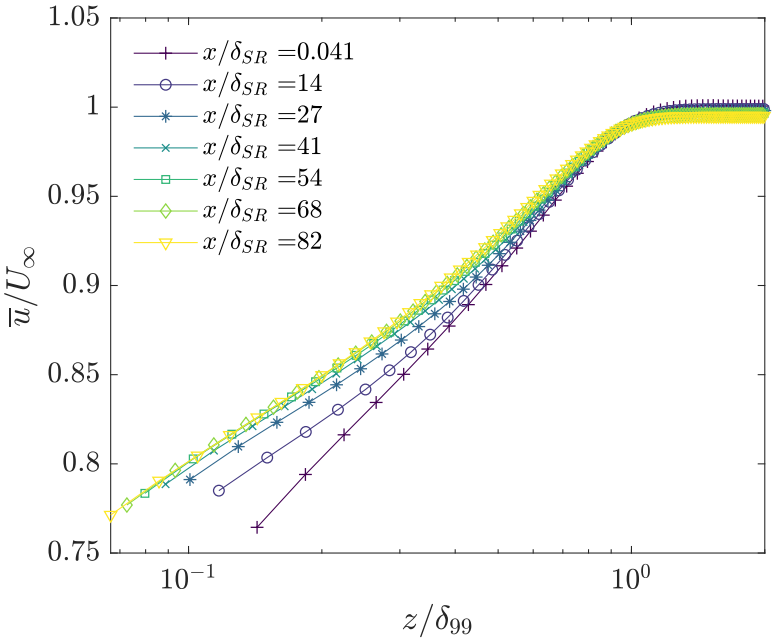

Figure 5.21: Outer scaled spanwise averaged velocity profiles $\overline{u}/U_\infty$ plotted against z/δ_{99} for *RS* flow. Symbols indicate streamwise progression. Color progression from dark to light is in the downstream direction.

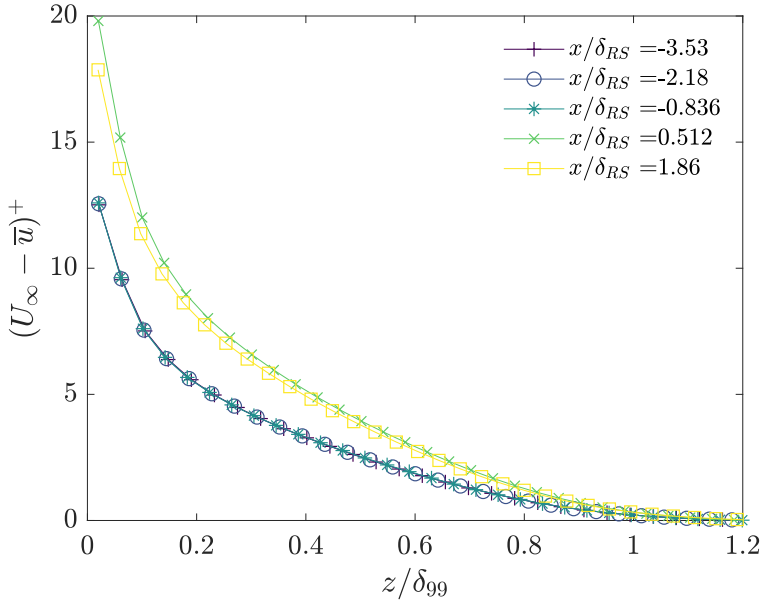

(a) Velocity defects near $x/\delta_{RS} = 0$

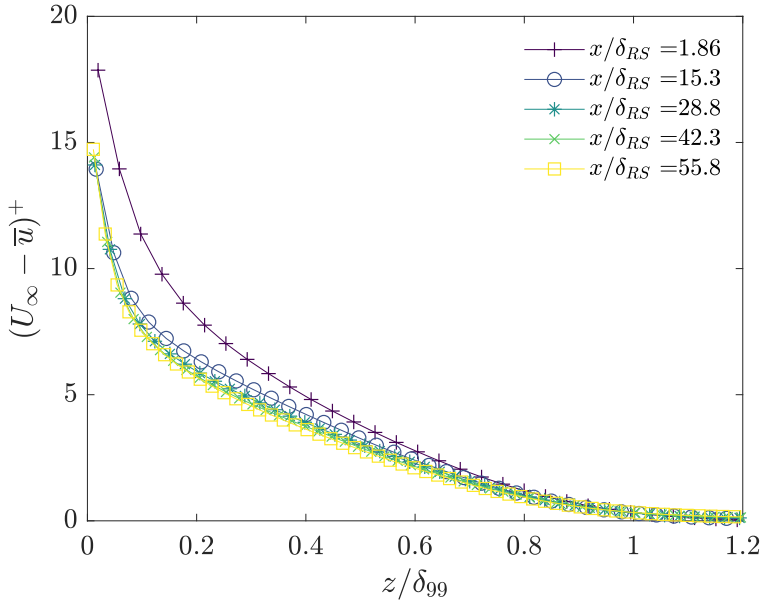

(b) Velocity defects for $x/\delta_{RS} > 0$

Figure 5.22: Development of velocity defect near *RS* transition. Downstream progression is represented with lighter line colours. Symbol keys are embedded in the respective figures and represent streamwise stations x/δ_{RS} for the data plotted. $\delta_{RS} = \delta_{99}$ at the location of wall-surface transition

streamwise Reynolds stress increases sharply in the downstream vicinity of the jump at $x/\delta_{RS} \leq 0.11$ since u_τ decreases abruptly at $x/\delta_{RS} > 0$, before gradually relaxing to the fully equilibrium smooth wall value by $x/\delta_{RS} = 79$. From figure 5.24 we note that it is difficult to identify the internal boundary layer location using the inner-outer layer descriptions of Efros and Krogstad [23] for $x/\delta_{RS} \leq 4.56$. The IBL becomes apparent further downstream at $x/\delta_{RS} \geq 7.25$ with the presence of two distinct slopes in the streamwise turbulent intensities. Comparison between the velocity and turbulence intensity plots 5.20 and 5.24 suggests that the turbulence intensities exhibit a slower relaxation rate when compared to the mean velocity profiles.

5.6.5 Internal boundary layer growth

We consider instantaneous, spanwise averaged growth of the internal layer. By applying least-square, linear fits to the inner and outer regions of streamwise Reynolds stress $\overline{u'^{+2}}$ with $x/\delta_{RS} > 10$, we generate estimates for the internal boundary layer growth rates for the RS cases in a method consistent with that used in the determination of IBLs in the SR case. Figure 5.25 shows an example of this 'knee-point' method applied to RS transition. Antonia and Luxton [4] provide experimental evidence of the growth of the internal layer in RS flow development, with an estimate for the power law growth $\delta_I \propto x^{0.43}$.

Ismail, Zaki, and Durbin [32] found $\delta_I \propto x^{0.41}$, whereas Hanson and Ganapathisubramani [30] suggest $\delta_I \propto x^{0.49}$ and $\delta_I \propto x^{0.46}$ for their mesh and grit roughness experiments respectively. A summary of results from the present LES is included in table 5.7. The present results suggest a dimensional growth rate such that $\delta_I \propto x^{b_2}$ with b_2 between 0.42 and 0.53. By keeping k_s^+ constant, we study the Reynolds number dependence of the internal boundary layer. In the case of RS wall transition, the self-preserving smooth wall boundary layer Reynolds stresses are recovered at $x/\delta_{RS} \approx 80$. We first present in figure 5.26 the power law growth estimates for the RS case. We note that the trend shown in the increasing Re cases from $R0 - R2$ are not self consistent when using the Reynolds stresses to determine the extent of the IBL. Hanson and Ganapathisubramani [30] state that the method of line-fits to the inner and outer layers in the turbulent stress curves is only appropriate for use with the SR transition case, perhaps this is accentuated at higher Re. It is clear from figure 5.27 that the IBL growth obtained via the turbulent stresses overpredicts the value suggested by the velocity profile merge-points. As in the SR section, contour plots of D_r, the relative velocity between adjacent streamwise stations, are shown in figure 5.27 to provide an additional measure of the IBL edge, with the results

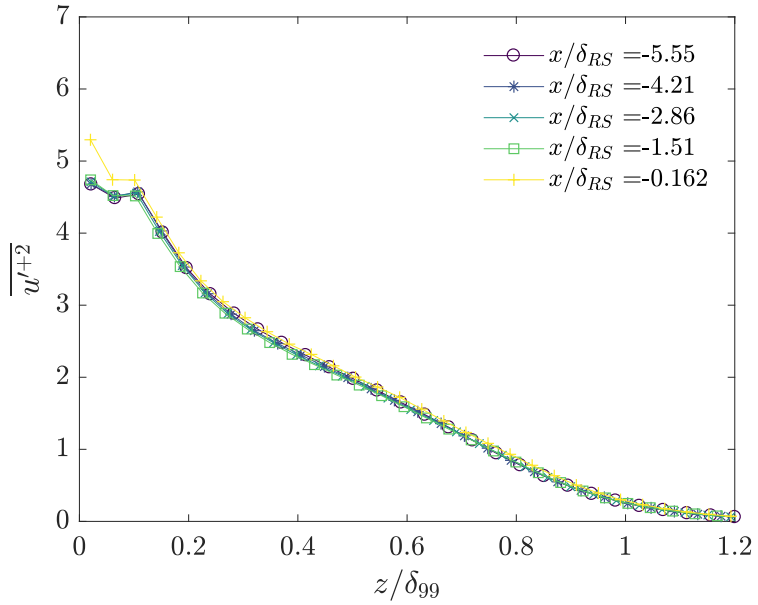

(a) $\overline{u'^{+2}}$, $x/\delta_{RS} < 0$ (equilibrium)

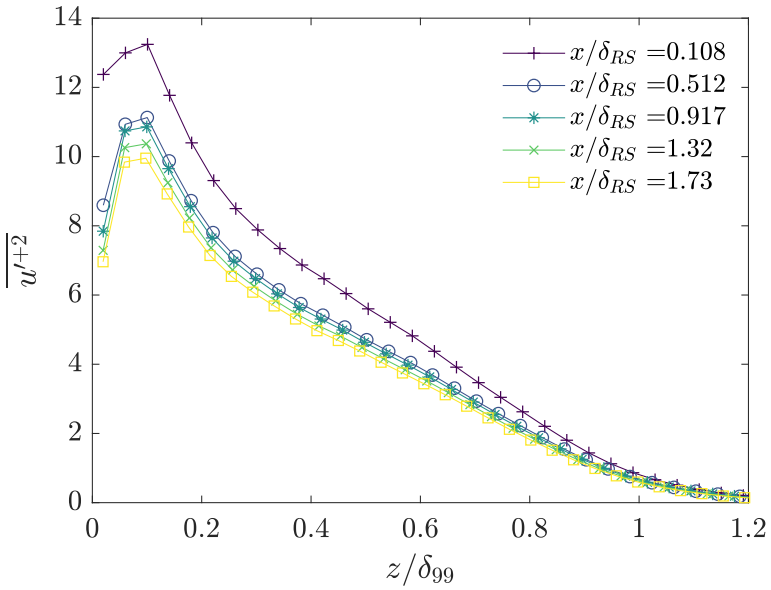

(b) $\overline{u'^{+2}}$ for $0 \leq x/\delta_{RS} \leq 1.73$ (non-equilibrium)

Figure 5.23: Development of streamwise Reynolds stresses near *RS* transition. Downstream progression is represented by dark→light color gradients and detailed with symbols indicating streamwise locations x/δ_{RS}.

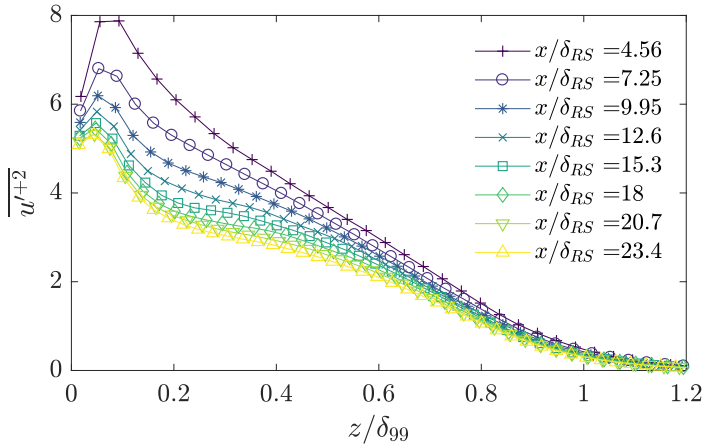

(a) Transitionally smooth region

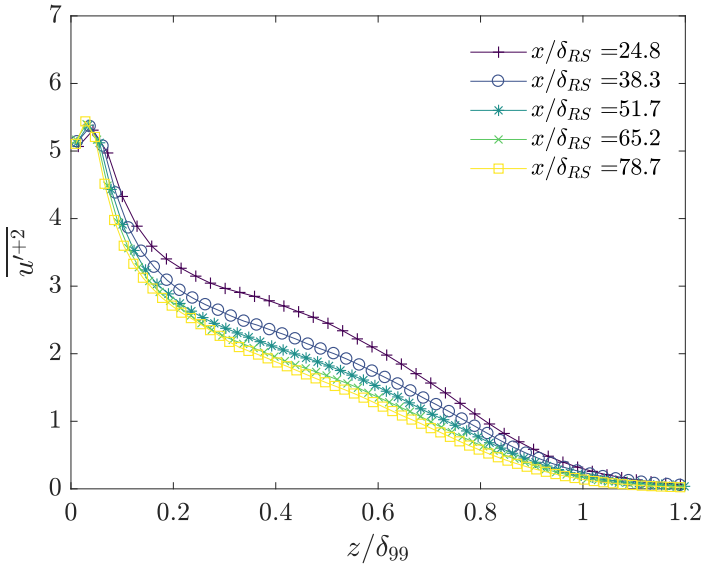

(b) Approach to fully smooth region

Figure 5.24: Development of streamwise Reynolds stresses downstream of *RS* transition. Square symbols indicate stations upstream of *RS* transition, circle symbols indicate stations downstream of *RS* transition

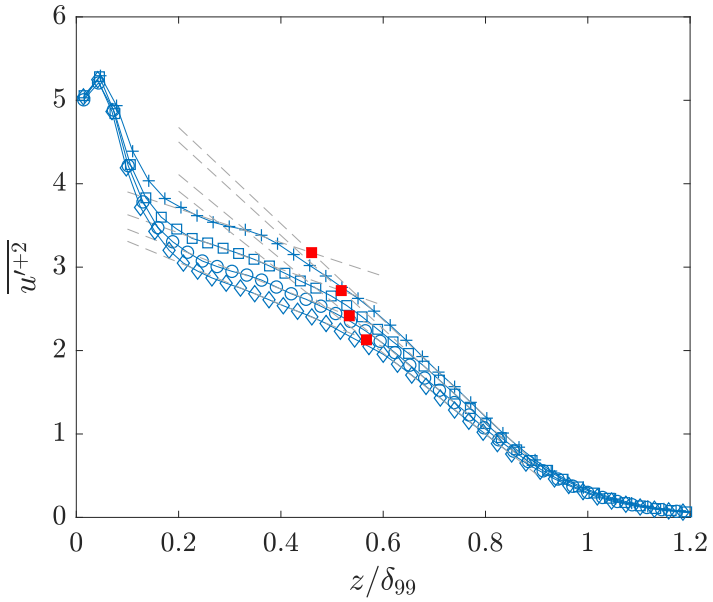

Figure 5.25: Demonstration of method using the inner and outer layer slopes to estimate the position of the internal boundary layer $\delta_I(x)$ in *RS* flow. Examples of IBL edge determination at four stations at $10 \leq x/\delta_{RS} \leq 20$ presented.

of the knee point method superimposed. We observe that the knee point estimate using $10 \leq x/\delta_{RS} \leq 22$ show agreement with the trends in IBL growth identified by the relative velocity measure, with the indication of over-prediction in δ_I using the knee-point method for all three cases, and particularly emphasised in the *R*2 case. Hanson and Ganapathisubramani [30] plot $\sqrt{\overline{u^2}}/\overline{u}$ against $\overline{u}/U_\infty$ as a diagnostic measure for the intermediate region that exhibits composite rough-smooth behaviour.

Hanson and Ganapathisubramani [30] studied *RS* transition at $Re_\tau = 4500$ and 7000 with $k_s^+ = 167$ and 1046 respectively. They used Preston tube measurements with a buffer-layer fit to determine the skin friction, and the velocity profile 'merge' technique (as did Antonia and Luxton [4]) to estimate the edge of the IBL. The present LES framework with the wall model is intended for higher orders of magnitude of Re_τ: hence a direct comparison of the *RS* transition with the experiments of Hanson and Ganapathisubramani [30] is not given here. A discernible trend with increasing Re_τ is observed in the power law exponent for *RS* transition, whereas the effect of the leading multiplicative constant is not as clear as in the *SR* case. Hanson and Ganapathisubramani [30] suggest two distinct growth rates about $x/\delta_{RS} = 1.5$; this is presently not investigated.

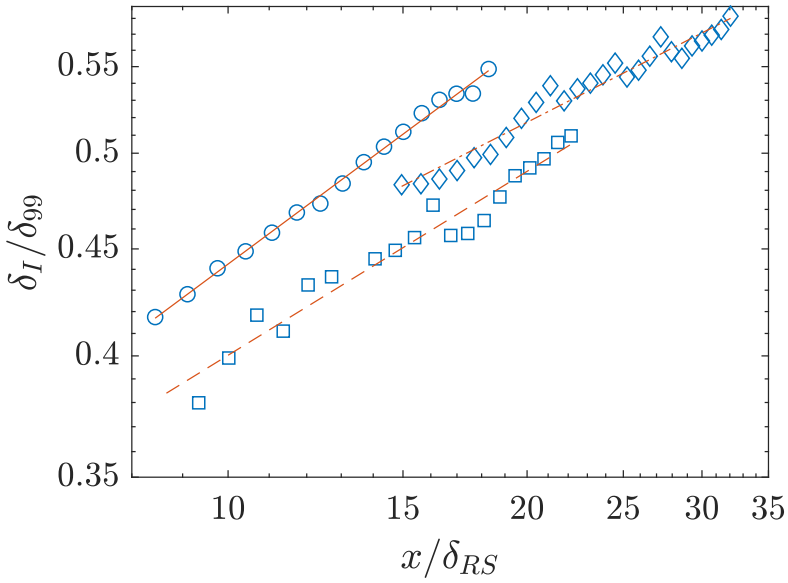

(a) Growth of IBL δ_I/δ_{99}

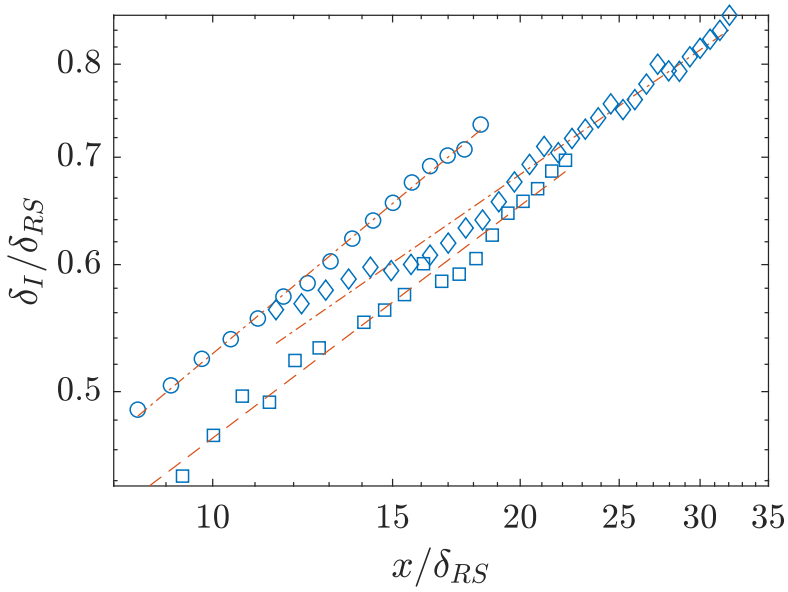

(b) Growth of IBL δ_I/δ_{SR}

Figure 5.26: Internal boundary layer thickness measures inferred from identification of inner and outer regions in streamwise Reynolds stress plots detailed in section 5.5.5. *RS* flow. Symbols are from LES, lines are least square power-law fits shown in table 5.3. squares and dash-dotted line: R0; circles and dotted line: R1, diamonds and dashed line: R2.

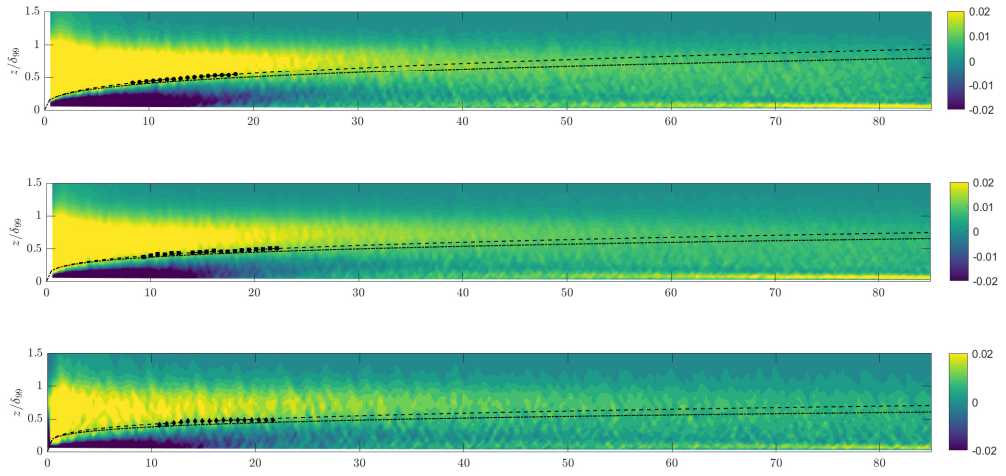

Figure 5.27: Contour plots of $D_r(x/\delta_{RS}, z/\delta_{99}) = (\overline{u_n} - \overline{u_{n+1}})/\overline{u_n}$. Percentage change in mean velocity profiles in x/δ_{RS}. Symbols and dashed lines reproduce non-dimensional power law curves shown in figure 5.26. Top to bottom indicates cases $R0$, $R1$, $R2$. Dash-dotted line indicates 10% reduction in power law exponents with the same leading constants. First three wall-normal points omitted due to near wall effect.

Case	Re_τ	k_s^+	A_1	b_1	A_2	b_2
R0	1.8×10^4	115	0.19	0.35	0.15	0.53
R1	4.8×10^4	115	0.20	0.29	0.15	0.48
R2	8.8×10^4	115	0.25	0.24	0.18	0.44

Table 5.7: Parameters for power-law fit to internal boundary layer in rough-smooth transition. $\delta_I/\delta_{99} = A_1(x/\delta_{99})^{b_1}$ and $\delta_I/\delta_{RS} = A_2(x/\delta_{RS})^{b_2}$

5.6.6 Relaxation length

As in the SR cases in section 5.5.6, we consider the relaxation of the skin friction C_f to equilibrium smooth wall values in addition to the internal boundary layer growth estimated by the power law fits with the same measures $(x/\delta_{RS})_{1,2}$. The relaxation measures defined in §5.5.6 are then used to allow direct comparison between the SR and RS flow cases. Here,

$$U^+_{\infty,RS} = \frac{1}{\kappa}\left[\log\left(\frac{\delta u_\tau}{\nu}\right) + 2\Pi\right] - \Delta U^+ + \Delta U^+_c + A \tag{5.13}$$

so that $U^+_{\infty,RS} = U^+_{\infty,S}$ when the friction velocity has relaxed to equilibrium smooth values as the corrective term ΔU^+_c relaxes to zero. $\Delta U^+ = 0$ in the smooth-wall region as defined in (5.2). Figures 5.28 summarises the skin-friction relaxation measures using the methods suggested in §5.5.6.

In RS transition, the difference in $(x/\delta_{RS})_1$ and $(x/\delta_{RS})_2$ appears to be an order of magnitude. We interpret these results with caution due to the discrepancy noted in case $R2$, and the fact that the estimated equilibrium flow lies beyond the horizontal extent of the computational domain. The relaxation distance is shown to increase with Re_τ for identical k_s^+ values. Table 5.8 presents a comparative summary of the two measures. We note that the local minima in the non-equilibrium C_f/C_{f0} for the SR cases is not observed in the RS cases. The reference boundary layer thickness δ_{RS} is the value immediately upstream of the sudden jump from the rough to smooth surface.

Case	Re_τ	k_s^+	$(x/\delta_{RS})_1$	$(x/\delta_{RS})_2$
R0	1.8×10^4	115	17	114
R1	4.8×10^4	115	20	224
R2	8.8×10^4	115	24	322

Table 5.8: Relaxation length estimates in RS transition: $(x/\delta_{RS})_1$ from recovery of skin-friction. $(x/\delta_{RS})_2$ from extrapolation using internal boundary layer power law fits.

5.6.7 Effect of varied k_s^+ at matched Re_τ

We consider the effect of varying k_s^+ in the case of RS transition, the skin-friction relaxation measure at matched Re_τ using case $R1$ as a reference. Table 5.9 summarises the k_s^+ parameters tested in this series of simulations. As in the SR transition case, we note that one of the instances $R1L$ lies in the transitionally rough regime. Figures 5.29a and 5.29b indicate a stronger dependence of the relaxation length on the upstream Re_τ value than on the roughness scale k_s^+. Again, we see that the peak undershoot in C_f downstream of the RS transition shows a strong dependence on k_s^+.

Case	k_s^+	$(x/\delta_{RS})_1$
R1L	56	20
R1	115	20
R1H	324	21

Table 5.9: Relaxation length estimates in RS transition:$(x/\delta_{RS})_1$ from skin-friction relaxation measures

5.7 Discussion

The qualitative trends in results presented in the previous sections show good agreement with the experiments of Antonia and Luxton [3, 4], Efros and Krogstad [23]

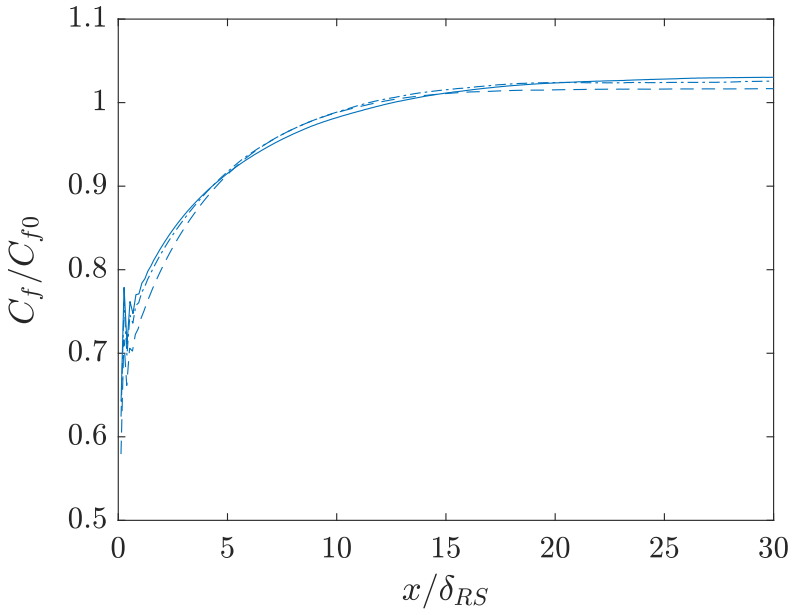

(a) C_f compared against equilibrium values.

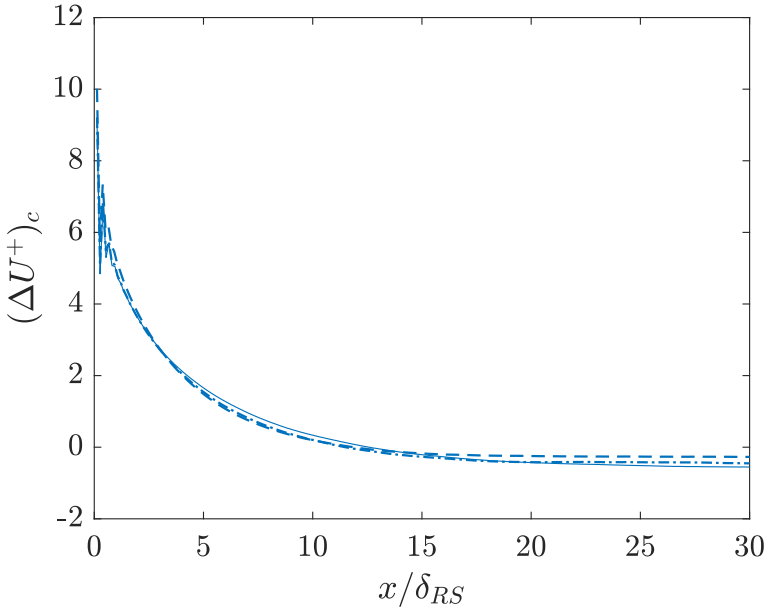

(b) Correction to velocity deficit in *RS* transition, ΔU_c^+ obtained from LES and required to recover non-equilibrium value using empirical form of ΔU^+.

Figure 5.28: Relaxation measures for *SR* transition. Line descriptions: dashed = *R*0; dash-dotted = *R*1; solid = *R*2

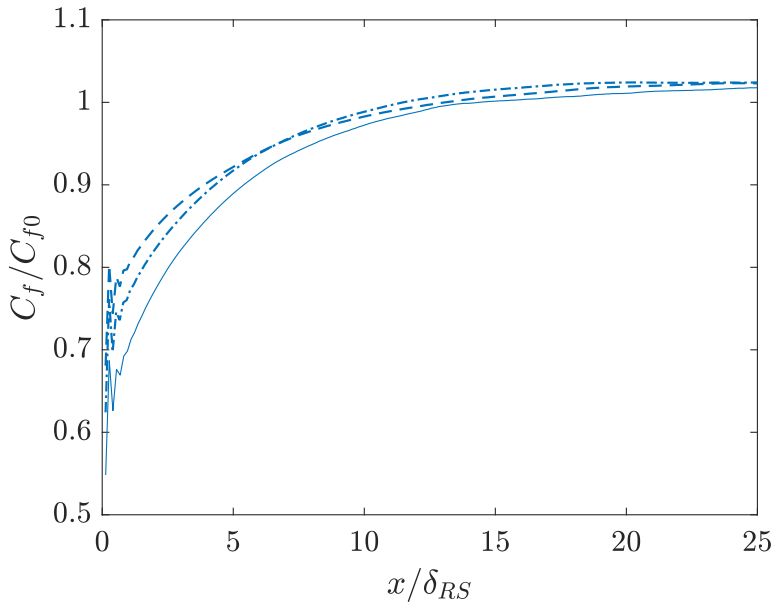

(a) Skin friction ratio with varying k_s^+ for *RS* cases, where C_{f0} is the smooth wall equilibrium value

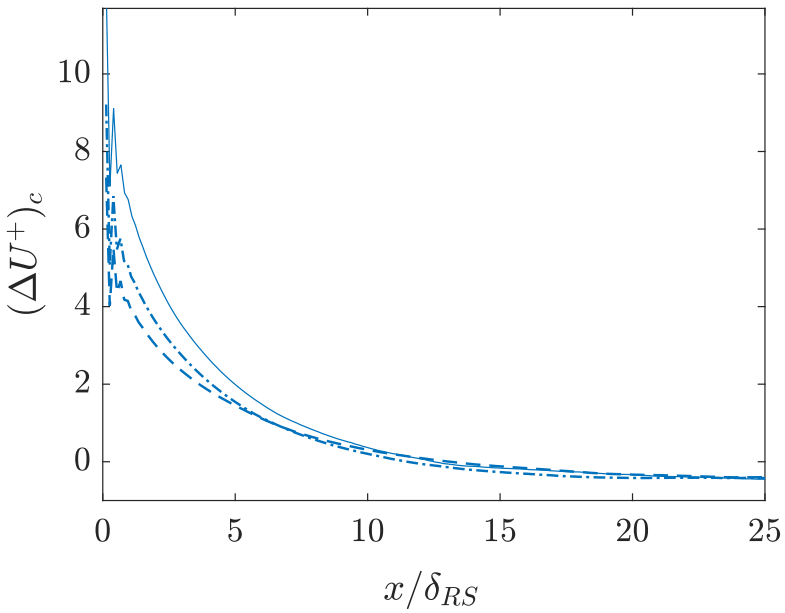

(b) Correction to ΔU^+ required to match LES friction velocity. $\Delta U^+ = 0$ represents equilbrium smooth-wall value.

Figure 5.29: Relaxation measures for *SR* transition case *R*1 with varying k_s^+, examining k_s^+ effects. Line descriptions: dashed = *R*1*L*; dash-dotted = *R*1; solid = *R*1*H*. Cases summarised in table 5.9

and Hanson and Ganapathisubramani [30]. The flat plate turbulent boundary layer is shown to experience slower adjustment (defined by skin-friction relaxation to the equivalent fully rough or smooth walled flow, and by the development of turbulent stress profiles such that the inner layer influenced by the new boundary condition merges completely with the outer flow) to the downstream wall surface in the case of *RS* transition when compared to the *SR* case. This is supported by the relaxation lengths defined in §5.5.6 and §5.6.6.

In *SR* transition, the effect of the new wall condition is first observed in the deviation of the C_f value from upstream equilibrium up to $x/\delta_{SR} \approx -5$, whereas the upstream influence appears minimal in the case of *RS* transition, confined to within $x/\delta_{RS} \approx -2$. We note that the current simulations consider an abrupt, discontinuous change in the surface condition, and this is reflected to some extent in the appearance of oscillations in the skin-friction up to three grid points immediately downstream of the surface change.

In *SR* transition, the oncoming smooth-wall flow experiences a sudden increase in turbulent energy production over the abrupt rough surface change, which is then diffused through the internal boundary layer to the outer flow. In *RS* flow, a sudden decrease in energy production occurs at the location of the transition, with the upstream high intensity turbulence advected over the rough wall surface. This diffusion of turbulent energy over the smooth wall compared with the advection from the upstream state in *RS* flow is a less efficient process than the energy production and outward diffusion over the rough-wall in *SR* flow, and provides an explanation for the generally longer recovery lengths in the *RS* cases. This interpretation is also supported by the study of Antonia and Luxton [4] who state that the larger proportion of turbulent energy in the outer layer offers an explanation of long recovery lengths in *RS* flow. Figures 5.30a and 5.30b show the distribution of turbulent kinetic energy in the non-equilibrium flow. We see that in each case the outer layer retains 'memory' of the upstream wall condition, but the plots support the suggestion that the influence of the outer layer in determining the IBL growth rate is greater in the *RS* case. Comparison of the contour plots of outer-scaled velocity defect measure D_r in figures 5.15 and 5.27 also suggests a stronger influence of the outer layer flow on the growth of the internal boundary layer in *RS* transition.

An alternative viewpoint of the relaxation length based on the friction velocity is seen by considering a defined turbulent timescale $T_t \propto \delta_{99}/u_\tau$ which can be interpreted as a measure of boundary layer turnover, and comparing it with the

mean flow timescale given by $T_m \propto x/U_\infty$, where x is the streamwise coordinate. Nagib, Chauhan, and Monkewitz [55] consider this to be a criterion for 'well-behaved' interactions between turbulent and mean-flow scales. 'Well-behaved' can be interpreted as a comment on flow equilibrium, and suggests that a ratio of these timescales, $T_t/T_m \propto \delta U_\infty^+/x$ may lead to insights on the recovery length. From previous experimental observations and the present LES study, we see that the most severe change in parameters across the SR or RS transition occurs in u_τ. The corresponding lengthscale for the flow is given by $L = U_\infty T_t/\delta$, such that the normalised relaxation parameter scales as $L \propto U_\infty^+$. This is supported by the plots of relaxation length against U_∞^+ in figure 5.31, where proportionality between U_∞^+ (and therefore the Reynolds number) and relaxation to equilibrium is seen. For matched U_∞^+ downstream, we see that relaxation in RS flow is slower and hence agrees with this scaling argument. In figure 5.32 we focus attention on the RS cases only, with U_∞^+ measured downstream. We note that the LES data is obtained at $x/\delta_{RS} = 25$ while the experimental data is obtained at $x/\delta_{RS} = 12.17$. Nevertheless, the simple scaling argument presented here is supported by this plot.

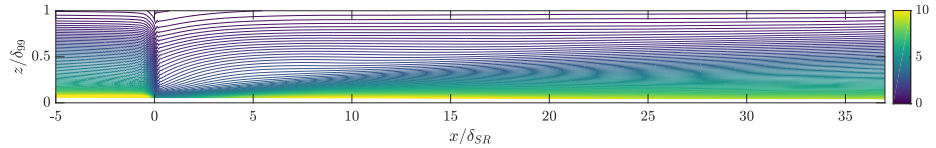

(a) Contours of normalised turbulent kinetic energy, SR, with upstream $Re_\tau = 84000$

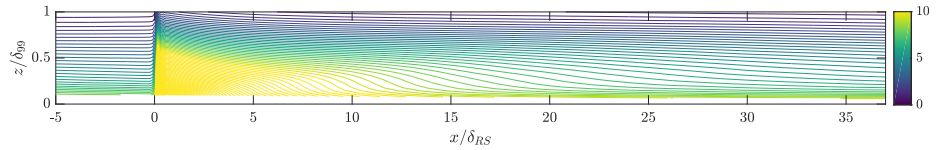

(b) Contour of normalised turbulent kinetic energy, RS, with upstream $Re_\tau = 88000$

Figure 5.30: Contours of $\overline{q^{+2}} = \overline{u'^{+2}} + \overline{v'^{+2}} + \overline{w'^{+2}}$. $\overline{u_\tau}$ overshoots in SR and undershoots in RS compared with downstream equilibrium values.

Figure 5.33 suggests the possibility of multiplicative scaling based on Re_τ as the power law exponents are roughly the same. Using the downstream Re_τ calculated at $x/\delta_{SR} = 20$ as a normalising parameter, we see an indication of the IBL growth rates collapsing in figure 5.33 to within 8.4% in the least-squares power-law fit for the smooth-rough internal boundary layer growth. This selection is to some extent supported by the $u_{\tau 0}$ scale definition by Hanson and Ganapathisubramani [30] and the choice of scaling parameter in internal flows as determined by Saito and Pullin [72] for channel flows. A similar collapse scaling has not been considered

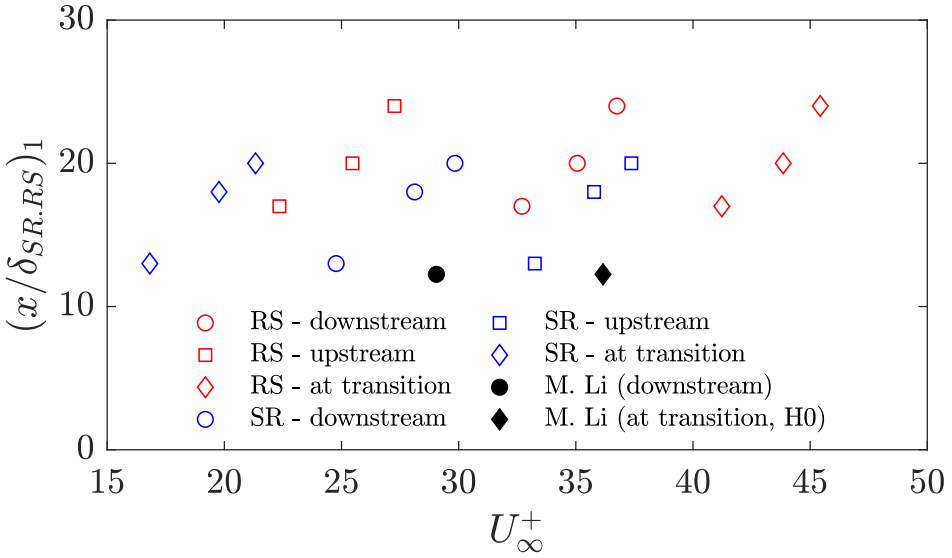

(a)

Figure 5.31: Dependence of relaxation measure $(x/\delta_{SR,RS})_1$ on U_∞^+. Open symbols: LES values calculated at $x/\delta = -5$ (upstream), $x/\delta = 0$ (at transition) and $x/\delta = 25$ (downstream). Red: *RS*, blue: *SR*. Filled symbols (experiments, private communication) show oil-film interferometry results of M. Li using case *H*0 with U_∞^+ calculated at $x/\delta_{RS} = 0.17$ (transition) and $x/\delta_{RS} = 12.17$ (downstream).

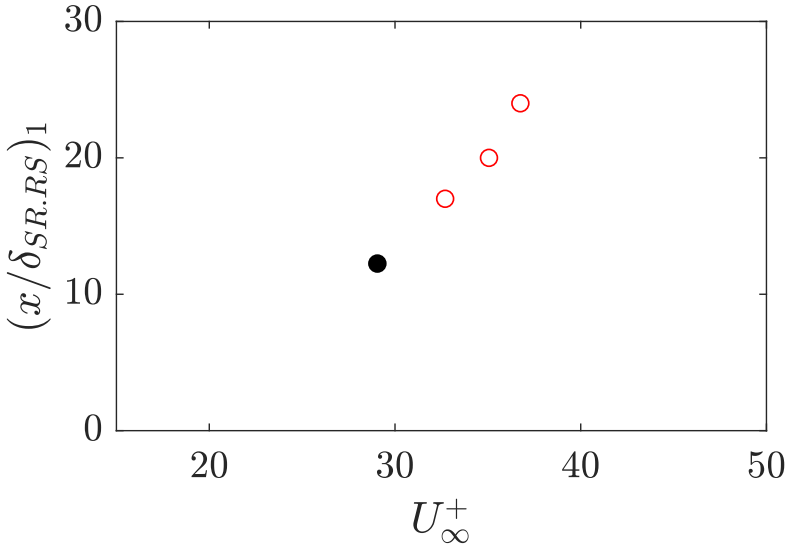

Figure 5.32: Examination of friction-velocity recovery using downstream states in *RS* transition (open symbols), comparison with available experimental data (filled symbol).

for the *RS* case due to the anomalous scatter in the *R*2 case (highest Reynolds number) simulation. In Figure 5.34, we demonstrate the possibility of a power law dependence of the relaxation lengths based on Re_τ. We recall the discrepancy observed in case *R*2, and therefore interpret the results with caution for the *RS* cases. Experimental data at low Re_τ is required to examine this effect over the full range of Re_τ.

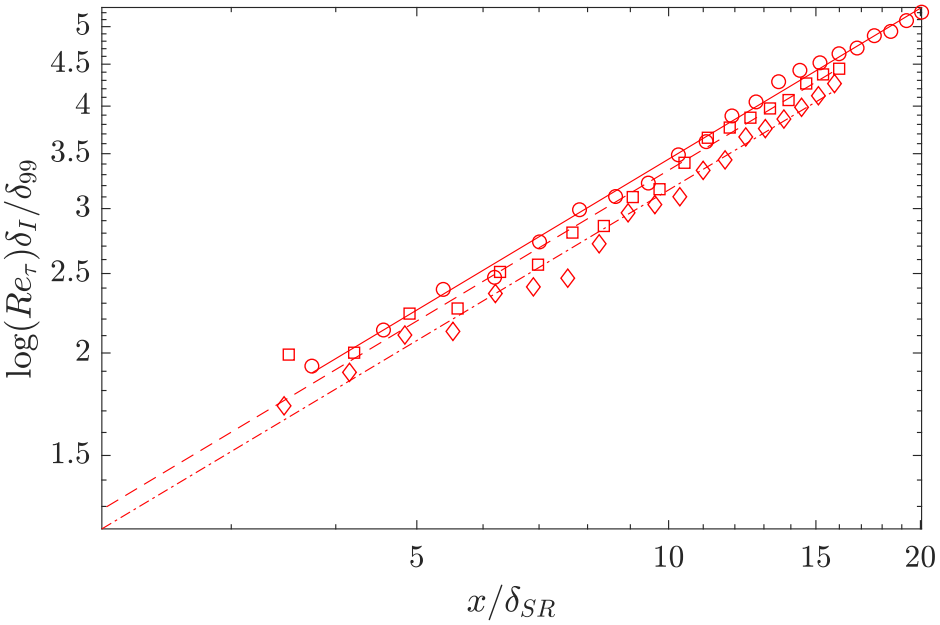

Figure 5.33: *SR* case IBL thickness scaled by Re_τ at $x/\delta_{SR} = 20$. Symbol and line descriptions as in Figure 5.14

Using the method of Andreopoulos and Wood [1], we define the rough and smooth lengthscales z_r and z_s respectively with the perturbation strength $M = \log(z_r/z_s)$ such that $z_r = k_s \exp(\kappa(D - A))$ for a rough wall and $z_s = \nu/u_\tau \exp(-\kappa A)$ for a smooth wall with $D = -4.0$, $A = 4.5$, $\kappa = 0.384$. Considering the specific case *S*0, the downstream lengthscale is that of the rough wall, $z_d = 1.02 \times 10^{-4}$ and $z_u = 4.4 \times 10^{-6}$, suggesting a perturbation strength of $M = 3.14$. Similarly, for case *R*0 we obtain $M = -2.86$.

5.7.1 Comparison with *RS* experiments at low Reynolds number

We briefly compare the skin-friction recovery behaviour to experimental measurements made in the High Reynolds Number Boundary Layer Wind Tunnel (HRNBLWT) at the University of Melbourne. The investigation of Li et al (private communication) focuses on obtaining accurate measurements of non-equilibrium

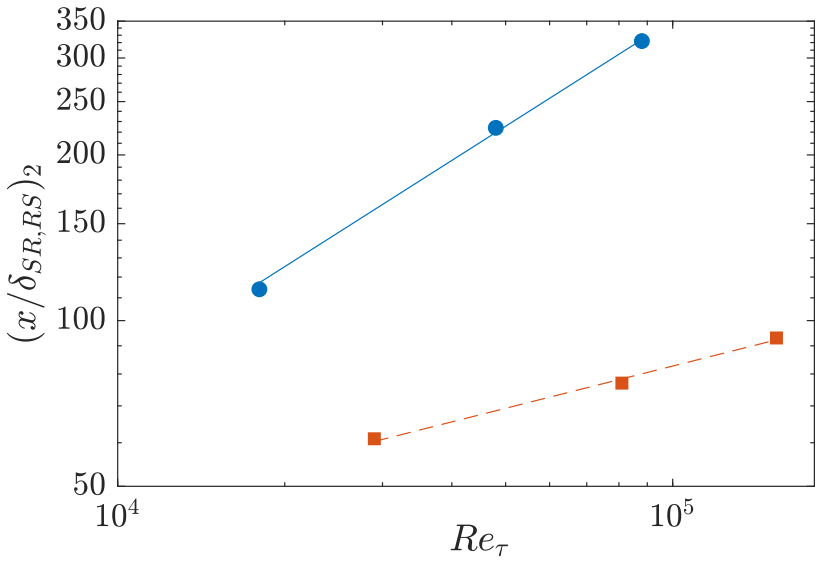

Figure 5.34: Reynolds number dependence of relaxation lengths in both SR and RS transition. (Red) Squares: SR, power law fit $\propto 4.7Re_\tau^{0.25}$; (Blue) Circles: RS, power law fit $\propto 0.22Re_\tau^{0.64}$

wall shear stresses using oil-film interferometry. We note that the wall-model in the present LES is designed for high Re. Their experimental design maintains $Re_\tau = 3500$ for comparison against existing data while keeping the roughness height equal to 3% of the boundary layer thickness at location of roughness transition. In running the simulation at low Re at the experimental value of k_s, we note that present conditions would require $k_s > 3h_0$, which violates the assumption of subgrid roughness in the model development. In running the simulation for the condition with high k_s, we note that numerical instabilities quickly develop in the result, causing large grid-scale oscillations, particularly in the rough-wall extent of the domain; we do not believe the model to be effective at extremely low values of Re_τ/k_s^+. Hence we restrict the comparison shown in figure 5.35 to the low $Re_\tau = 3730$ case in the transitionally rough regime with $k_s^+ = 28$.

In figure 5.35, the skin-friction is normalised against the last data point x/δ_{RS} available in the experimental results and compared with the oil-film interferometry of Li and Hutchins. Items $H0 - H3$ refer to the relative position of the maximum rough element heights to the smooth-wall 'zero' coordinate. In $H0$ the smooth wall is 2.85 mm below the sandpaper roughness crests, while in $H3$ the smooth wall is above the sandpaper by 0.06mm. The experimental investigations revealed a marked influence of the crests of the roughness elements relative to the downstream smooth

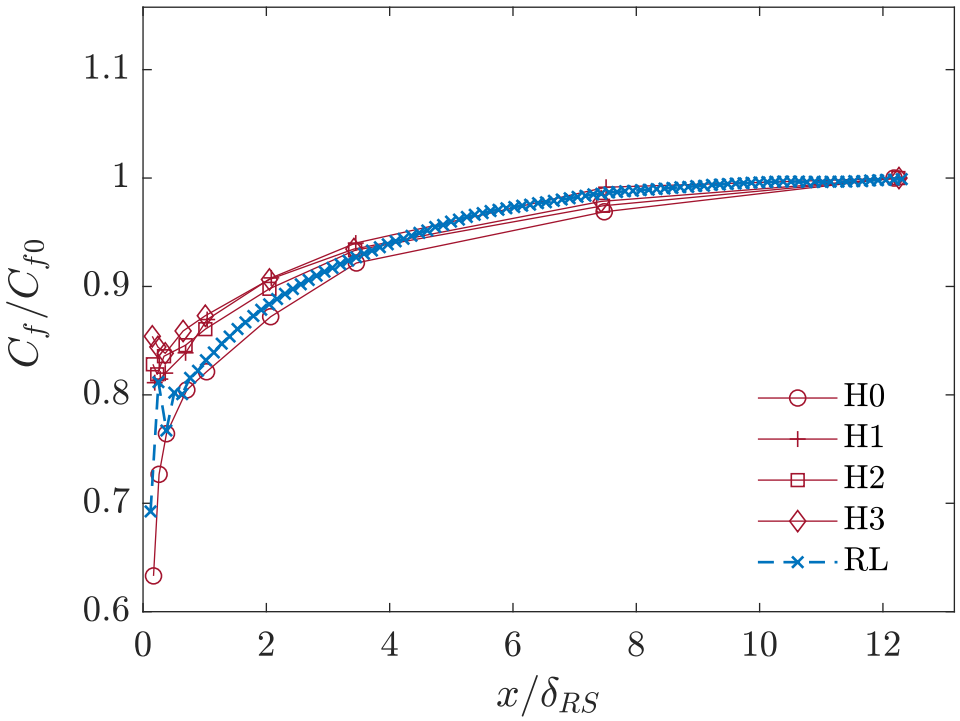

Figure 5.35: Comparison of low Reynolds number *RS* case, identified as *RL* against experimental data at $Re_\tau = 3500$ (Li, Hutchins, private communication). Note $k_s^+ = 28$ in computation. LES upstream $Re_\tau = 3730$, normalised against C_{f0} at $x/\delta_{RS} = 12.25$. $H0 - H3$ denote deviation of rough-wall crest from smooth surface. $H0 = -2.85mm$, $H1 = -1.94mm$, $H2 = -0.98mm$, $H3 = 0.06mm$ (Positive values mean smooth wall is higher)

surface, and the present low *Re* LES show good agreement with the $H0$ case. The relative origin effect is not explicitly captured in the LES; the wall model does not take into account the influence of the 'true' origin in the wall-normal coordinate in the presence of roughness elements. We also note a degree of uncertainty introduced by the choice of $x/\delta_{SR} = 12.25$ as the downstream reference station. The IBL merges with the outer layer (for case $H3$) at $x/\delta_{RS} \approx 25$ (Li and Hutchins, private communication). The present LES study of high *Re RS* transition supports the use of $x/\delta = 12.25$ as the reference location for skin-friction through the finding that the C_f relaxes at a much faster rate than the IBL.

Chapter 6

LES OF TBL WITH SHORT, ABRUPT PATCH OF ROUGHNESS

6.1 Introduction

In this chapter we consider the development of a turbulent boundary layer over a nominally smooth wall with a patch of roughness that extends a short distance in the streamwise coordinate and spans the entire spanwise distance of the bottom wall. The non-equilibrium flow over a short rough patch has previously been studied experimentally at low Reynolds numbers by Andreopoulos and Wood [1], Jacobi and McKeon [33], and computationally by Bou-Zeid, Meneveau, and Parlange [6]. Bou-Zeid, Meneveau, and Parlange [6] approached the problem with a Lagrangian scale-dependent subgrid model with a dynamic Smagorinsky coefficient. Their work also differs in that it considers transitions between rough-walls of different aerodynamic roughness measures, whereas the present research considers transitions between hydrodynamically smooth ($\Delta U^+ = 0$) and rough surfaces.

The present work uses the SV SGS model which does not contain a wall function in the outer LES, and prescribes Dirichlet boundary conditions at the virtual wall. A static (time-invariant) 'impulsive' roughness patch is applied to an upstream equilibrium smooth-walled flow to generate non-equilibrium flow downstream. A numerical simulation of this problem mitigates, to some extent, the difficulties in obtaining measurements over the short rough wall extent. The length of the roughness patch is designed such that the skin-friction (previously shown to relax more rapidly than the Reynolds stresses) does not equilibrate to the rough-wall conditions before the wall boundary becomes abruptly smooth.

Andreopoulos and Wood [1] (henceforth AW) consider an extent of roughness less than than $10\delta_0$ to be sufficient for an 'impulsive' roughness patch, choosing to study a patch of length $3\delta_0$, and the experimental investigation of Jacobi and McKeon [33] (henceforth JM) considers a patch length of $1.5\delta_0$, where δ_0 represents the 99% boundary layer thickness at the onset of the patch. The study is essentially one of the interaction of two internal boundary layers, and presents useful insights into physical scenarios with multiple roughness transitions, and the development of multiple IBLs in turbulent flows.

Results, primarily related to the wall shear stress characteristics are presented first,

Case	Re_τ	k_s^+	$(C_f/C_{f,ref})_{max}$	$(C_f/C_{f,ref})_{min}$
I1L	8.1×10^4	58	2.33	0.70
I1	8.1×10^4	103	3.05	0.65
I1H	8.1×10^4	326	4.98	0.53

Table 6.1: Summary of key parameters at constant Re_τ with varying equivalent roughness

Case	Re_τ	k_s^+	$(C_f/C_{f,ref})_{max}$	$(C_f/C_{f,ref})_{min}$
I0	2.8×10^4	104	3.40	0.68
I1	8.1×10^4	103	3.05	0.65
I2	1.3×10^5	103	2.88	0.60

Table 6.2: Summary of key parameters for varying Re_τ with nominally constant k_s^+

including a comparison with the *SR* transition case presented in chapter 5. The present LES framework allows the simple case described above to be extended to an arbitrary distribution of patches in the streamwise extent specifically in high Re regimes. We first study the effect of k_s^+ keeping Re_τ constant, and then proceed to briefly examine effects of Reynolds numbers and strip length at matched k_s on the integrated flow statistics.

6.2 Problem description and numerical method

The domain setup is identical to that of the *SR* transition case presented in chapter 5, with the exception that the rough-wall is of a shorter streamwise length $x/\delta_{SR} = 3$ and $x/\delta_{SR} = 1.5$, ending well before the exit plane in the computational domain. The numerical methods, including boundary conditions and the SV-SGS model are described in detail in chapter 3.

6.3 Results

Tables 6.1 and 6.2 summarise the simulation parameters. Re_τ and k_s^+ values are reported immediately upstream of the *SR* transition. C_f has been normalised against the smooth-wall skin friction upstream of the *SR* jump at $x/\delta_{SR} = -1$, denoted by $C_{f,ref}$. The tabulated summary supports the broader trends from the previous *SR* transition section with respect to the effect of k_s^+ and Re_τ on the maximum overshoot or undershoot and the relaxation lengths respectively. Re_τ has a larger effect on the relaxation length, while the peak overshoots and undershoots in C_f show stronger dependence on the k_s^+ values.

We begin with an analysis of the skin-friction relaxation in non-equilibrium tran-

sition. Figure 6.1 considers matched upstream Re_τ subject to a range of k_s^+ as summarised in table 6.2. The raw (figure 6.1a) and normalised (figure 6.1b) skin-friction coefficients are presented. Values are normalised by $C_{f,ref}$ which is the skin-friction coefficient at $(x/\delta_{SR} = -1)$. For a roughness patch length consistent with that studied by AW, we observe a larger departure from the equilibrium values in C_f due to the initial SR perturbation with increasing k_s^+. The higher roughness patch is shown to experience faster recovery in C_f, with the general trend consistent with the SR flow studied in chapter 5. Subsequent downstream transition due to the RS perturbation at $x/\delta_{SR} = 3$ also follows this trend, with increasing k_s^+ leading to larger departures from the smooth wall equilibrium for $x/\delta_{SR} > 3$. An examination of the peak overshoot due to the initial roughness impulse in figure 6.2 suggests a power law dependence of the normalised skin-friction coefficient on k_s^+ at matched Re_τ. A similar power-law trend is noted in figure 6.3 considering the undershoot at the RS transition. We note that the power law fit (least-squared) has a greater coefficient of determination R^2 value when using the C_f value at $x/\delta_{SR} = 3$ as the reference for the RS transition, since this accounts for the difference in upstream Re_τ in the rough-wall region.

In figure 6.4, we compare strip widths of $x/\delta_{SR} = 1.5$ and $x/\delta_{SR} = 3.0$, at the same Re_τ, with the same values for the equivalent sand-grain roughness k_s. We note that the SR transition dominates the skin-friction characteristics, with the peak overshoot and recovery rates being remarkably similar (within 2.5%) until $x/\delta_{SR} = 1.5$, at which point the flow over the shorter strip transitions. A comparison with an equivalent transition between the fully-smooth to fully-rough surfaces in figure 6.5 indicates comparable relaxation rates, with a higher initial slope owing to the higher peak in k_s. This scenario is still distinctly different from the SRS case, since the upstream velocity and turbulent stress profiles are modified (and not in equilibrium) when the wall boundary returns to the smooth-wall case.

In figure 6.6, the boundary layer shape factor $H = \delta^*/\theta$ for matched Re_τ is shown for various k_s^+, where δ^* and θ represent the displacement and momentum thicknesses respectively. This series of curves also highlights the upstream influence of the perturbation, which is shown to be abrupt at the onset of the roughness patch near $x/\delta_{SR} \approx 0$, with gradual recovery downstream of the RS transition. AW indicate some uncertainty in their values of θ, and hence H; the LES provides a clear, consistent description of the shape factor over the rough patch, albeit at higher Re. The initial decrease of H at $x/\delta_{SR} = 0$, the rapid increase over the rough patch

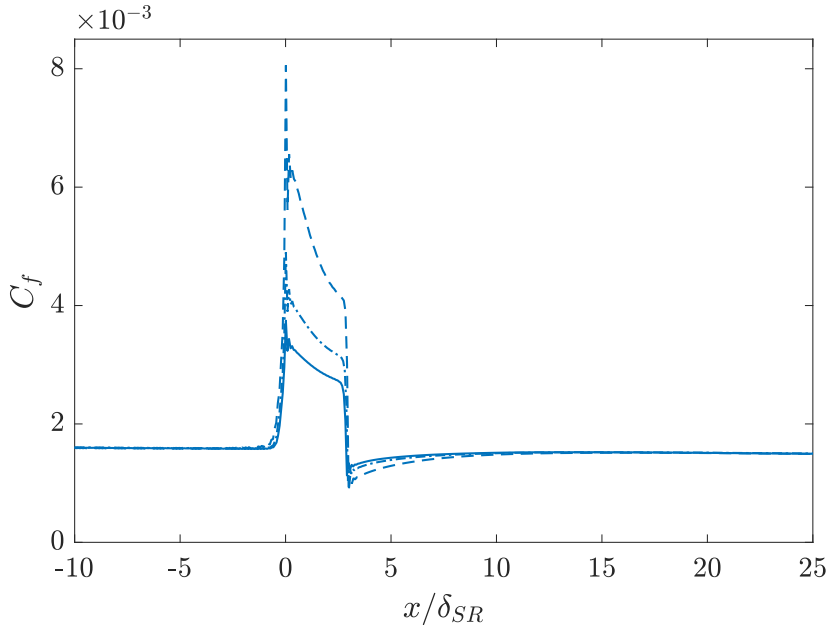

(a) C_f development in SRS transition

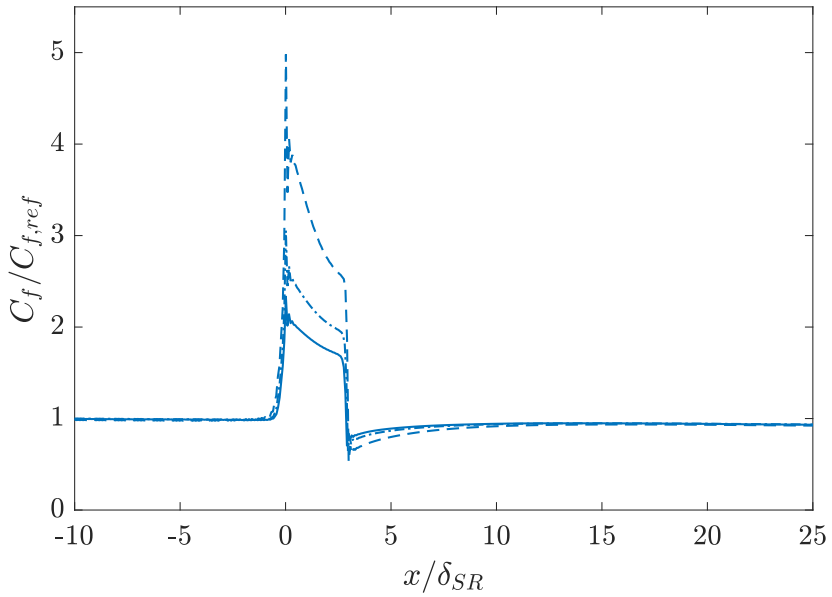

(b) Normalised C_f, $C_{f,ref}$ is given by skin-friction coefficient immediately upstream of transition to rough surface.

Figure 6.1: Skin-friction coefficient, raw and normalised against upstream state in TBL with impulsive roughness patch. Patch length is $3\delta_{SR}$ as in the study of Andreopoulos and Wood [1]. Solid line: I1L; dash-dotted line: I1, dashed line: I1H in order of increasing k_s^+ at matched Re_τ

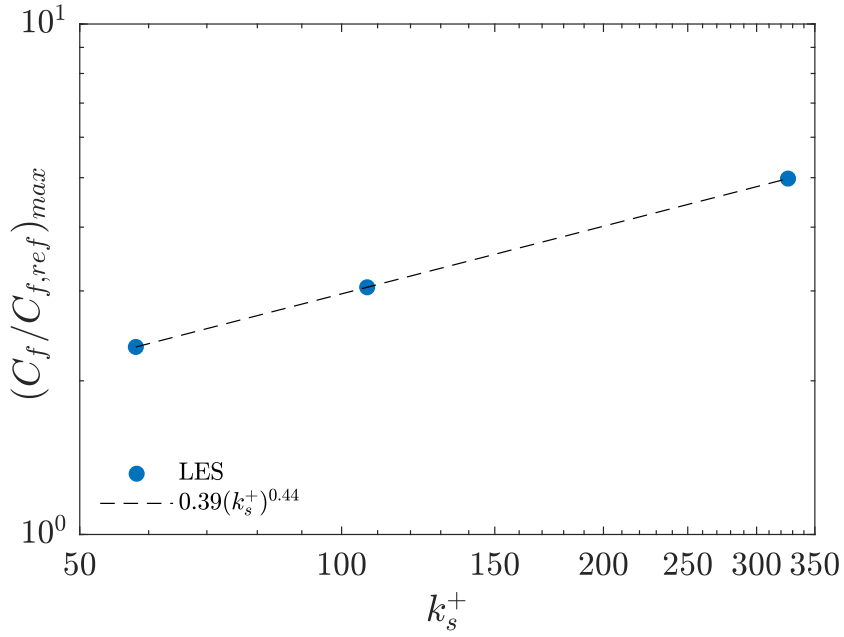

Figure 6.2: Effect of varying k_s^+ on maximum C_f deviation from upstream flow at matched Re_τ on a log-log plot. LES and power law fits shown (Lines offset for clarity)

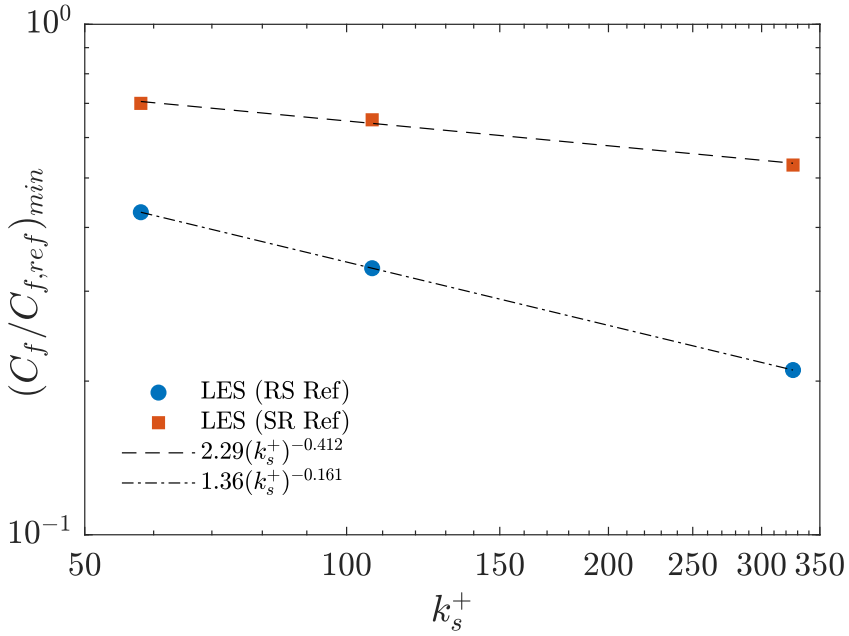

Figure 6.3: Effect of varying k_s^+ on maximum C_f deviation from upstream flow at matched Re_τ on a log-log plot. LES and power law $\propto C_1(k_s^+)^{0.44}$ shown. Least-squares power law fit to $C_1 = 0.39$

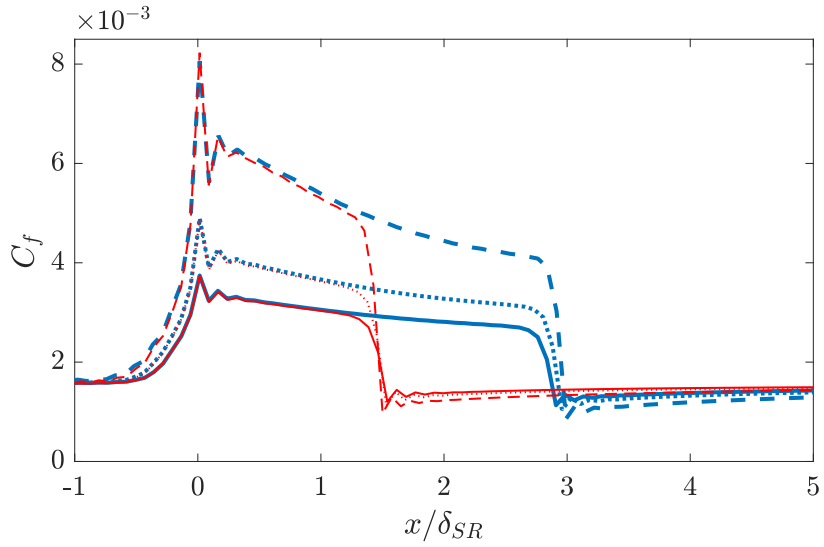

Figure 6.4: Comparison with differing strip widths, $x/\delta_{SR} = 1.5$ (red) and $x/\delta_{SR} = 3.0$ (blue). k_s^+ and Re_τ as in table 6.1

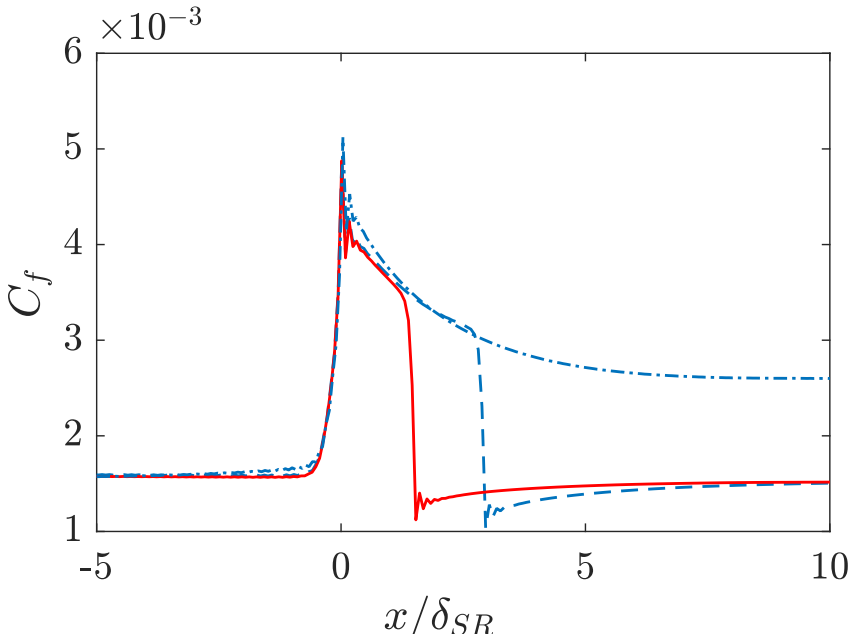

Figure 6.5: Comparison with differing strip widths, including that with a pure SR transition, $x/\delta_{SR} = 1.5$ (red) and $x/\delta_{SR} = 3.0$ (blue). k_s^+ and Re_τ as in table 6.1

extent, and the subsequent downstream relaxation appear as distinct features of the LES result which match the general trend in H shown by AW.

In figure 6.7, we consider Reynolds number effects by plotting the shape factor H at matched equivalent sand-grain roughness k_s. Increasing H with decreasing Re_τ is apparent, and the growth rate of H over the rough patch shows consistent

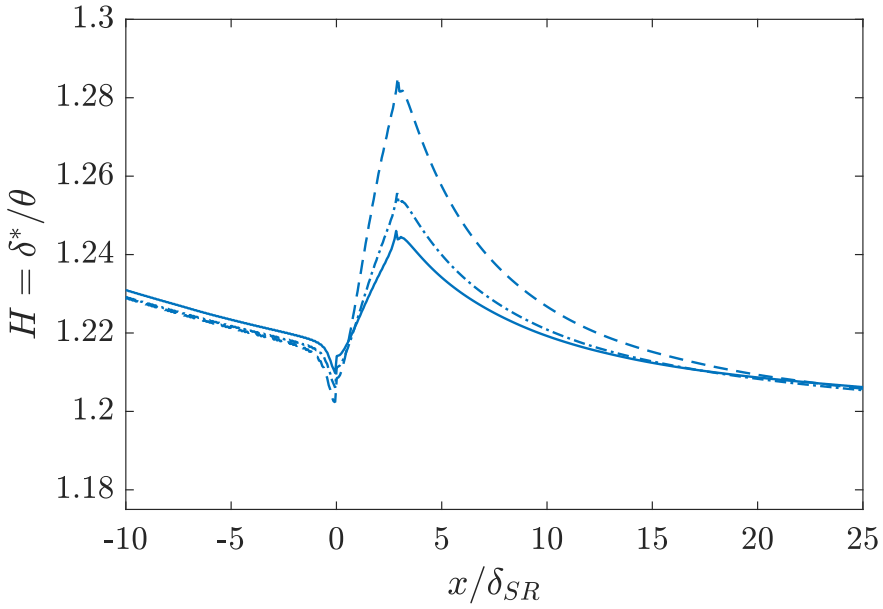

(a) LES results at matched Re_τ

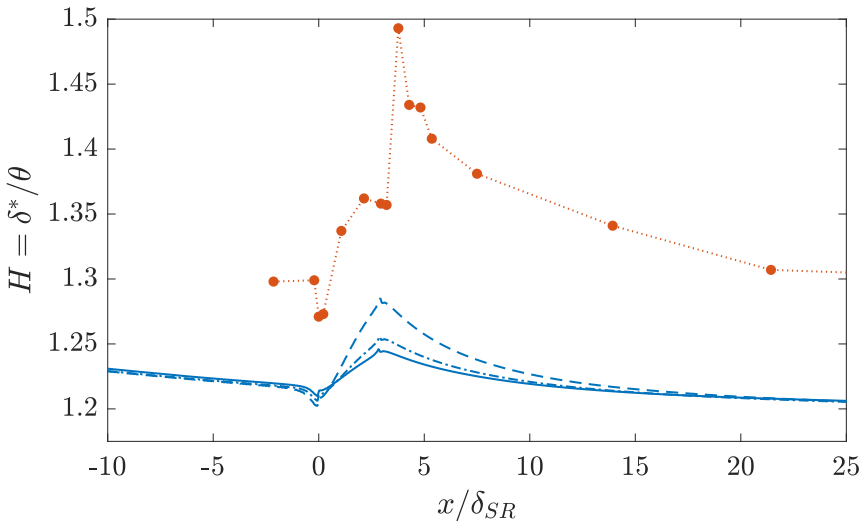

(b) Comparison with low *Re* experiment [1]. Circles are data points listed in AW (Table 1 in AW).

Figure 6.6: Boundary layer shape factor $H = \delta^*/\theta$ for *SRS* transition. Solid line: I1L; dash-dotted line: I1, dashed line: I1H in order of increasing k_s^+ at matched Re_τ

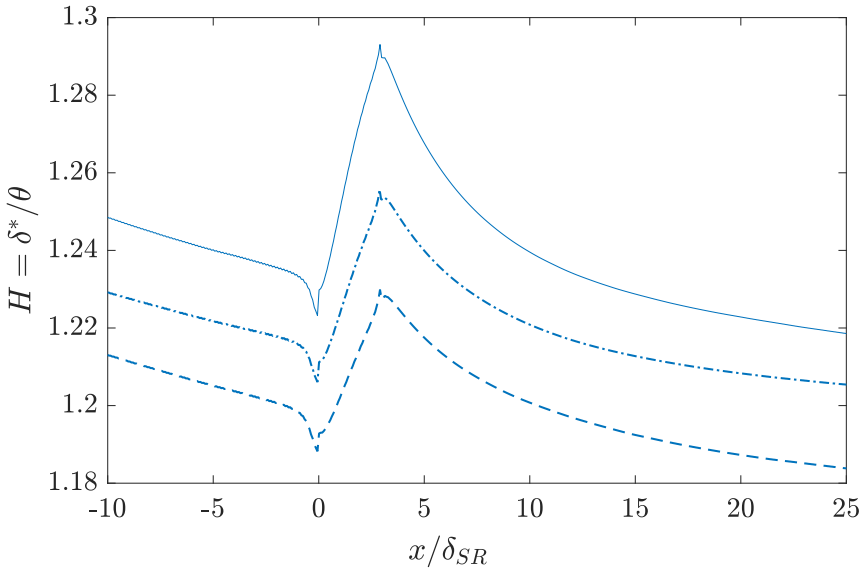

Figure 6.7: Re_τ effects on boundary layer shape factor in static impulsive roughness patch. Solid: I0; dash-dot: I1; dashed: I2, in order of increasing Re_τ. Rough patch length $3\delta_{SR}$

trends amongst the three cases, verifying a strong dependence on k_s^+. In each of the non-equilibrium flows considered, we note that the effect of the roughness elements on the buffer layer, which is proportional to k_s^+, increases at the SR transition due to rapid changes in u_τ beyond the expected values at equilibrium (conversely decreases at the RS transition). Reynolds number effects are perhaps best illustrated by a considering the effect of increasing Re_θ at constant k_s^+ as shown in figure 6.8. Combined with figures 6.2, 6.3, this supports the idea that at high Re, the overshoot and undershoot characteristics are functions of k_s^+ only. Agreement of smooth wall values within 2.4% of the asymptotic Coles-Fernholz 2 expression is achieved with the present model.

6.4 Discussion

The impulsive roughness study suggests that the first perturbation from $S - R$ dominates the flow development by determining the peak overshoot of C_f at a given Re_τ and k_s^+ value. Faster relaxation is observed at higher k_s, but the length of the rough patch has little effect on the development of C_f directly over the patch at matched Re_τ. Comparing the impulsive static roughness problem to the transition from a fully-smooth to fully-rough surface suggests a difference in the underlying dynamics due to the increase in upstream C_f at the location of the SR transition in

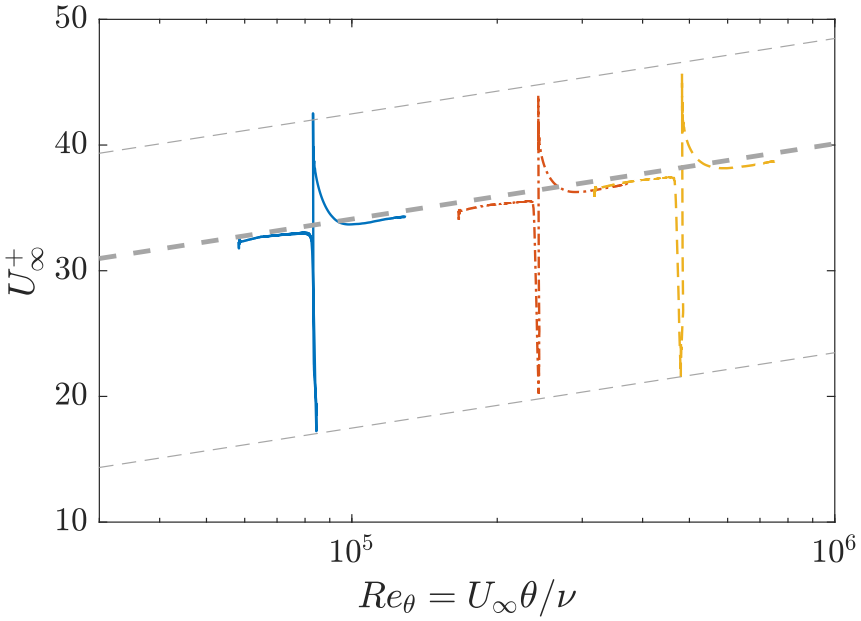

Figure 6.8: Re_θ dependence of normalised friction velocity U_∞^+, with upper and lower bounds on $\Delta U^+ = 8$, lower bound is $\Delta U^+ = -17$ relative to the nominal smooth wall value. Solid line: I0; dash-dot: I1; dash:I2.

the latter case. While we suggest a power law dependence of the peak overshoot on k_s^+ at high Re, any extrapolation must be carefully assessed due to the $\delta/k_s > 40$ constraint at which point the specific roughness geometry may alter the behaviour of the boundary layer significantly. The results presented in this chapter help mitigate some of the difficulty with measuring ΔU^+ directly over the roughness patch.

With flow manipulation via designed roughness a possible motivation, we suggest one potential extension to this problem through a combination of the ideas presented in chapters 4, 5 and 6 by initiating a turbulent flow over a smooth-wall followed by gradual linear increment in the roughness up to $k_s^+ = k_s u_\tau/\nu$ in the asymptotically rough regime. This also allows us to verify the numerical effect of the roughness discontinuity visualised through oscillations in skin-friction immediately downstream of the change in boundary conditions. We include the case of inhomogeneous roughness distribution from a smooth-walled boundary to a linearly increasing roughness distribution in figure 6.9. The initial smooth flow Re_θ matches that of case $S1$. For a range of slopes α consistent with the results presented in chapter 4, we expect, at large Re_θ, that the equilibrium U_∞^+ value is a function of α only. The feasibility of manufacturing a surface with such a controlled roughness profile perhaps merits more studies, with the potential for the linear-roughness case

to be used as the canonical flow in studies of equilibrium rough-wall flows.

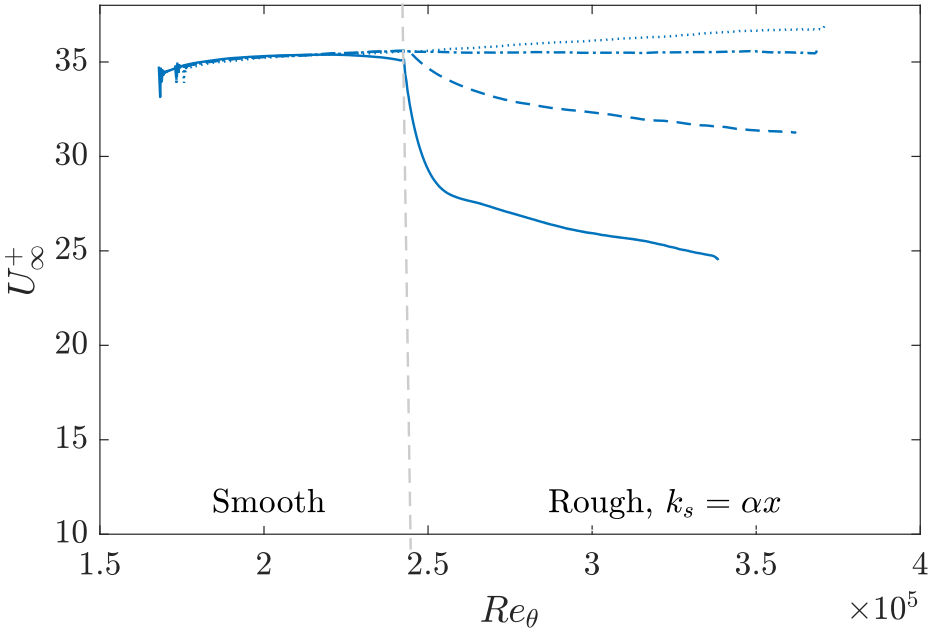

Figure 6.9: Transition from smooth to linearly increasing roughness distribution. Solid line: $\alpha = 10^{-4}$, dashed line: $\alpha = 10^{-5}$, dash-dot line: $\alpha = 10^{-6}$, dot line: $\alpha = 10^{-7}$

Chapter 7

CONCLUSIONS

7.1 Summary of findings

Turbulent boundary layers are present in a variety of engineering applications, and present a challenging class of problems whose detailed understanding will help to improve predictive capabilities, enabling the study of more complicated flow structures, perhaps leading to informed manipulation of desirable flow features. In this dissertation, we focus our attention on the canonical flat plate turbulent boundary layer flow modified by sand-grain type surface roughness subject to varied spatial distribution. To enable the study of such flows, we use large eddy simulations with the stretched vortex subgrid scale model in the outer flow LES, coupled with a virtual-wall model that has built in information on the local roughness geometry through a log-layer velocity deficit function ΔU^+.

In Chapter 4, we introduce an interesting class of self-similar, equilibrium rough-wall flows which exist in the presence of linearly varying surface roughness $k_s = \alpha x$. For fixed values of the Kármán constant, the Coles wake factor and the offset parameter, the model contains two parameters. The first is the exponent m in the outer-flow velocity profile, while the second is the dimensionless slope of the roughness-scale variation with distance α. The model is predicated on the ansatz that all terms in the von Kármán integral relationship are constant in the streamwise direction. This is found to be consistent with constant U_∞^+ (therefore constant skin-friction, since the two parameters are algebraically linked) and with all defined measures of the boundary layer thickness growing linearly with streamwise distance. For given m, α, both the streamwise and the wall-normal component of the mean velocity depend only on the single similarity variable $z/(\alpha\, x)$. Two interesting flows that approximately satisfy the model conditions are the zero-pressure gradient boundary layer, $m = 0$ and pure sink flow $m = -1$.

Large-eddy simulations have been performed for the zero-pressure gradient boundary-layer flow using a wall-modelled region that incorporates a simple semi-empirical model of subgrid wall roughness. This roughness model is local and allows linear growth of the roughness scale with streamwise distance. Utilising a recycling technique for creating appropriate turbulent inflow boundary conditions and employing

an iteration method to ensure that the virtual origin of both the boundary-layer growth and the roughness-scale variation coincide, for given α, the LES produces a statistically steady boundary-layer flow. At sufficiently large Reynolds number Re_x, the displacement, momentum and the ninety-nine percent velocity thicknesses all grow approximately linearly with streamwise distance while U_∞^+ becomes constant. Comparison of the LES and semi-empirical model results for some mean measures of the boundary-layer development show similar qualitative and quantitative trends. Both the mean-velocity profiles and the streamwise mean-square velocity-fluctuations obtained from the LES show self-similar scaling on the length scale $k_s = \alpha\, x$ with dependence on α. The velocity defect profiles show reasonable collapse using the Rotta-Clauser length scale independent of α. In the sense that U_∞^+, or equivalently the surface skin-friction coefficient, remains streamwise constant, both the semi- empirical model and the LES can be interpreted as representing the fully-rough limit of a Moody-like diagram for the zero-pressure gradient boundary-layer flow. Since the present model indicates a range of admissible values of m, the present work suggests that existence of a class of Moody-like diagrams for turbulent boundary-layer flows in the presence of linear streamwise variation in surface roughness.

In Chapter 5, we extend the analysis of Chapter 4 to the study of turbulent boundary layer development subject to an abrupt change in the streamwise roughness distribution. We consider both smooth-rough and rough-smooth transitions. LES with wall-modelling to capture near-wall small scale behaviour and the response to sand-grain type roughness, have been used to study the development of turbulent boundary layers over a flat plate with abrupt spatial variations in surface roughness over a range of Re and k_s parameters. The present wall-model allows a direct calculation of the friction velocity u_τ based on local roughness perturbations, suitable for non-equilibrium flow conditions. Measures of turbulent flow recovery downstream of a step transition in SR and RS flows are obtained, and are shown to have growth rates with trends consistent with previous experimental results. Recovery lengths are shown to be larger in the case of RS transition than in SR with fitted power law curves. Integral parameters such as skin-friction are shown to relax faster than mean velocities and turbulent stresses. Power law dependence of the peak skin-friction departure from equilibrium is shown. Examination of streamwise velocity development contours identifies the internal boundary layer near the wall which is affected by the abrupt roughness modifications; this region is apparent from both the first and second order statistics. The power law growth rates for the IBL in SR

transition exhibit collapse based on Re downstream of the transition. Outer scaled velocity measures provide a better estimate of the IBL edge than inner scaled values, since the abrupt overshoots, undershoots and subsequent relaxation of u_τ mask the magnitude of the jump at low x/δ downstream of the transition.

An extension of the high-Re non-equilibrium TBL flow is then presented in chapter 6 with an investigation of SRS transition focusing on integral parameters. Spatially impulsive roughness patches are investigated, with two cases presented for comparison with the low Re experiments of Andreopoulos and Wood [1] (patch length $3\delta_{SR}$) and Jacobi and McKeon [33] (patch length $1.5\delta_{SR}$). The numerical analysis provides insights into the flow field development at high Reynolds numbers through consistent trends in skin-friction variation including its departure from equilibrium and recovery, including flow statistics directly over and in the immediate vicinity of the short rough-patch where the non-equilibrium effects are strongest. Peak overshoots and undershoots show a power law dependence on the roughness Reynolds number k_s^+. An empirically determined collapse is observed in the boundary layer shape factor over the high-Re range considered at approximately the same k_s^+. The results demonstrate that the present computational framework, with the stretched vortex subgrid-scale model in the outer LES coupled with a near-wall model with a simple roughness correction for ΔU^+ are a viable method of studying flows at high-Re under non-equilibrium conditions.

7.2 Outlook

The work presented in this dissertation supports the use of the wall-modeled large eddy simulation framework in boundary layer flows at high Reynolds numbers. Flow manipulation using roughness has been suggested as one possible motivation for investigations into rough-walled boundary layer flows. Constant skin-friction flows with development dependent only on a single parameter (roughness slope) perhaps merit investigations in greater detail due to implications on passive flow control; this is particularly relevant with improved small scale manufacturing capabilities. The particular LES framework described in this work suggests an opportunity for extensions to codes designed for engineering applications, maybe reducing the need for LES-RANS hybrid modeling. One of the more enticing features is that the code reproduces observed roughness effects with a very simple mean-velocity correction, with no requirement for forcing functions or explicit resolution of roughness elements.

BIBLIOGRAPHY

[1] J. Andreopoulos and D. H. Wood. "The response of a turbulent boundary layer to a short length of surface roughness". In: *Journal of Fluid Mechanics* 118 (1982), pp. 143–164. DOI: 10.1017/S0022112082001001.

[2] R.A. Antonia and P-Å Krogstad. "Turbulence structure in boundary layers over different types of surface roughness". In: *Fluid Dynamics Research* 28.2 (2001), p. 139. URL: http://stacks.iop.org/1873-7005/28/i=2/a=A06.

[3] RA Antonia and RE Luxton. "The response of a turbulent boundary layer to a step change in surface roughness Part 1. Smooth to rough". In: *Journal of Fluid Mechanics* 48.4 (1971), pp. 721–761.

[4] RA Antonia and RE Luxton. "The response of a turbulent boundary layer to a step change in surface roughness. Part 2. Rough-to-smooth". In: *Journal of Fluid Mechanics* 53.4 (1972), pp. 737–757.

[5] G. I. Barenblatt and V. M. Prostokishin. "Scaling laws for fully developed turbulent shear flows. Part 2. Processing of experimental data". In: *Journal of Fluid Mechanics* 248 (1993), pp. 521–529. DOI: 10.1017/S0022112093000886.

[6] Elie Bou-Zeid, Charles Meneveau, and Marc B. Parlange. "Large-eddy simulation of neutral atmospheric boundary layer flow over heterogeneous surfaces: Blending height and effective surface roughness". In: *Water Resources Research* 40.2 (). DOI: 10.1029/2003WR002475. eprint: https://agupubs.onlinelibrary.wiley.com/doi/pdf/10.1029/2003WR002475. URL: https://agupubs.onlinelibrary.wiley.com/doi/abs/10.1029/2003WR002475.

[7] Ian P. Castro, Hong Cheng, and Ryan Reynolds. "Turbulence Over Urban-type Roughness: Deductions from Wind-tunnel Measurements". In: *Boundary-Layer Meteorology* 118.1 (Jan. 2006), pp. 109–131. ISSN: 1573-1472. DOI: 10.1007/s10546-005-5747-7. URL: https://doi.org/10.1007/s10546-005-5747-7.

[8] Leonardo P. Chamorro and Fernando Porté-Agel. "Velocity and Surface Shear Stress Distributions Behind a Rough-to-Smooth Surface Transition: A Simple New Model". In: *Boundary-Layer Meteorology* 130.1 (Jan. 2009), pp. 29–41. ISSN: 1573-1472. DOI: 10.1007/s10546-008-9330-x. URL: https://doi.org/10.1007/s10546-008-9330-x.

[9] H. Cheng and Ian P. Castro. "Near-Wall Flow Development After A Step Change In Surface Roughness". In: *Boundary-Layer Meteorology* 105.3 (Dec. 2002), pp. 411–432. ISSN: 1573-1472. DOI: 10.1023/A:1020355306788. URL: https://doi.org/10.1023/A:1020355306788.

[10] W Cheng, DI Pullin, and Ravi Samtaney. “Large-eddy simulation of flow over a grooved cylinder up to transcritical Reynolds numbers”. In: *Journal of Fluid Mechanics* 835 (2018), pp. 327–362.

[11] W. Cheng and R. Samtaney. “Power-law versus log-law in wall-bounded turbulence: A large-eddy simulation perspective”. In: *Physics of Fluids* 26.1 (2014), p. 011703. DOI: 10.1063/1.4862919. eprint: https://doi.org/10.1063/1.4862919. URL: https://doi.org/10.1063/1.4862919.

[12] Wan Cheng, DI Pullin, and Ravi Samtaney. “Large-eddy simulation of separation and reattachment of a flat plate turbulent boundary layer”. In: *Journal of Fluid Mechanics* 785 (2015), pp. 78–108.

[13] W. Cheng et al. “Large-eddy simulation of flow over a cylinder with Re_D from 3.9×10^3 to 8.5×10^5 : a skin-friction perspective”. In: *Journal of Fluid Mechanics* 820 (2017), pp. 121–158. DOI: 10.1017/jfm.2017.172.

[14] D. Chung. “Numerical Simulation and Subgrid-Scale Modeling of Mixing and Wall-Bounded Turbulent Flows”. In: *Ph.D. thesis, Aeronautics, California Institute of Technology* (2009).

[15] D. Chung. “Numerical simulation and subgrid-scale modeling of mixing and wall-bounded turbulent flows”. PhD thesis. California Institute of Technology, 2009.

[16] D. Chung and D. I. Pullin. “Large-eddy simulation and wall-modeling of turbulent chanel flow”. In: *Journal of Fluid Mechanics* 631 (2009), pp. 281–309.

[17] F. H. Clauser. “The Turbulent Boundary Layer”. In: *Adv. Appl. Mech.* 56 (1956), pp. 1–51.

[18] F. H. Clauser. “Turbulent boundary layers in adverse pressure gradients”. In: *Journal of the Aeronautical Sciences* 21 (1954), pp. 91–108.

[19] C. F. Colebrook. “Turbulent Flow in Pipes, With Particular Reference to the Transition Region Between the Smooth and Rough Pipe Laws”. In: *Journal of the Institution of Civil Engineers (London, England)* 11 (1939), pp. 133–156.

[20] D. Coles. “The law of the wake in the turbulent boundary layer”. In: *Journal of Fluid Mechanics* 1.02 (1956), pp. 191–226. ISSN: 0022-1120.

[21] Donald Coles. “Remarks on the equilibrium turbulent boundary layer”. In: *Journal of the Aeronautical Sciences* 24 (1957), pp. 495–506.

[22] Brian Dean and Bharat Bhushan. “Shark-skin surfaces for fluid-drag reduction in turbulent flow: a review”. In: *Philosophical Transactions of the Royal Society of London A: Mathematical, Physical and Engineering Sciences* 368.1929 (2010), pp. 4775–4806. ISSN: 1364-503X. DOI: 10.1098/rsta.2010.0201. eprint: http://rsta.royalsocietypublishing.org/content/368/1929/4775.full.pdf. URL: http://rsta.royalsocietypublishing.org/content/368/1929/4775.

[23] Vladislav Efros and Per-Åge Krogstad. "Development of a turbulent boundary layer after a step from smooth to rough surface". In: *Experiments in Fluids* 51.6 (Dec. 2011), pp. 1563–1575. ISSN: 1432-1114. DOI: 10.1007/s00348-011-1167-2. URL: https://doi.org/10.1007/s00348-011-1167-2.

[24] Karen A. Flack and Michael P. Schultz. "Roughness effects on wall-bounded turbulent flows". In: *Physics of Fluids* 26.10 (2014), p. 101305. DOI: 10.1063/1.4896280. eprint: https://doi.org/10.1063/1.4896280. URL: https://doi.org/10.1063/1.4896280.

[25] Karen A. Flack, Michael P. Schultz, and Thomas A. Shapiro. "Experimental support for Townsend's Reynolds number similarity hypothesis on rough walls". In: *Physics of Fluids* 17.3 (2005), p. 035102. DOI: 10.1063/1.1843135. eprint: https://doi.org/10.1063/1.1843135. URL: https://doi.org/10.1063/1.1843135.

[26] O. Flores and J. Jiménez. "Effect of wall-boundary disturbances on turbulent channel flows". In: *Journal of Fluid Mechanics* 566 (Oct. 2006), p. 357.

[27] S. Ghosal. "An analysis of numerical errors in large-eddy simulations of turbulence". In: *J. Comp. Phys.* 125 (1996), pp. 187–206.

[28] P. S. Granville. "The frictional resistance and turbulent boundary layer of rough surfaces". In: *Journal of Ship Research* 2 (1958), pp. 52–74.

[29] F. R. Hama. "Boundary-layer Characteristics for Smooth and Rough Surfaces". In: *Trans. Soc. Nav. Arch. Mar. Engrs* 62 (1954), pp. 333–351.

[30] R.E. Hanson and B. Ganapathisubramani. "Development of turbulent boundary layers past a step change in wall roughness". In: *Journal of Fluid Mechanics* 795 (2016), pp. 494–523. DOI: 10.1017/jfm.2016.213.

[31] M. Inoue and D. I. Pullin. "Large-eddy simulation of the zero-pressure-gradient turbulent boundary layer up to $Re_\theta = O(10^{12})$". In: *Journal of Fluid Mechanics* 686 (Sept. 2011), pp. 507–533. ISSN: 0022-1120. DOI: 10.1017/jfm.2011.342. URL: http://null/10.1017/jfm.2011.342.

[32] Umair Ismail, Tamer A. Zaki, and Paul A. Durbin. "Simulations of rib-roughened rough-to-smooth turbulent channel flows". In: *Journal of Fluid Mechanics* 843 (2018), pp. 419–449. DOI: 10.1017/jfm.2018.119.

[33] I. Jacobi and B. J. McKeon. "New perspectives on the impulsive roughness-perturbation of a turbulent boundary layer". In: *Journal of Fluid Mechanics* 677 (2011), pp. 179–203. DOI: 10.1017/jfm.2011.75.

[34] J.W. Jewkes, Y.M. Chung, and P.W. Carpenter. "Modification to a Turbulent Inflow Generation Method for Boundary-Layer Flows". In: *AIAA journal* 49.1 (2011), pp. 247–250. ISSN: 0001-1452.

[35] Javier Jiménez. "Turbulent Flows Over Rough Walls". In: *Annual Review of Fluid Mechanics* 36.1 (Jan. 2004), pp. 173–196. ISSN: 0066-4189. DOI: 10.1146/annurev.fluid.36.050802.122103.

[36] Malcolm Barry Jones, Ivan Marusic, and AE Perry. "Evolution and structure of sink-flow turbulent boundary layers". In: *Journal of Fluid Mechanics* 428 (2001), pp. 1–27.

[37] T. Kameda et al. "Realization of the turbulent boundary layer over the rough wall satisfied the conditions of complete similarity and its mean flow quantities". In: *Journal of Fluid Science and Technology* 3.1 (2008), pp. 31–42.

[38] J. Kim, P. Moin, and R. Moser. "Turbulence statistics in fully developed channel flow at low Reynolds number". In: *Journal of Fluid Mechanics* 177.1 (1987), pp. 133–166.

[39] KC Kim and RJ Adrian. "Very large-scale motion in the outer layer". In: *Physics of Fluids* 11 (1999), pp. 417–422.

[40] P-Å Krogstad, R.A. Antonia, and L.W.B. Browne. "Comparison between rough-and smooth-wall turbulent boundary layers". In: *Journal of Fluid Mechanics* 245 (1992), pp. 599–617.

[41] Myoungkyu Lee and Robert D. Moser. "Direct numerical simulation of turbulent channel flow up to $Re_\tau \approx 5200$". In: *Journal of Fluid Mechanics* 774 (2015), pp. 395–415. DOI: 10.1017/jfm.2015.268.

[42] T.S. Lund, X. Wu, and K.D. Squires. "Generation of turbulent inflow data for spatially-developing boundary layer simulations". In: *Journal of Computational Physics* 140.2 (1998), pp. 233–258.

[43] T.S. Lundgren. "Strained spiral vortex model for turbulent fine structure". In: *Phys Fluids* **2**5 (1982), pp. 2193–2203.

[44] M. MacDonald et al. "Turbulent flow over transitionally rough surfaces with varying roughness densities". In: *Journal of Fluid Mechanics* 804 (2016), pp. 130–161. DOI: 10.1017/jfm.2016.459.

[45] I. Marusic and G.J. Kunkel. "Streamwise turbulence intensity formulation for flat-plate boundary layers". In: *Physics of Fluids* 15.8 (2003), p. 2461. ISSN: 10706631. DOI: 10.1063/1.1589014. URL: http://link.aip.org/link/PHFLE6/v15/i8/p2461/s1%5C&Agg=doi.

[46] I. Marusic et al. "Wall-bounded turbulent flows at high Reynolds numbers: Recent advances and key issues". In: *Physics of Fluids* 22 (2010), p. 065103.

[47] Beverley J Mckeon et al. "Further observations on the mean velocity distribution in fully developed pipe flow". In: *Journal of Fluid Mechanics* 501 (2004), pp. 135–147.

[48] *Proceedings of the Fifth International Congress On Applied Mechanics*. Wiley, New York, 1938.

[49] A. Misra and D. I. Pullin. "A vortex-based subgrid stress model for large-eddy simulation". In: *Phys. Fluids* 9 (1997), pp. 2443–2454.

[50] A. Misra and D.I Pullin. “A vortex-based subgrid model for large-eddy simulation”. In: *Phys. Fluids* **9** (1997), pp. 2443–2454.

[51] Lewis F Moody. “Friction factors for pipe flow”. In: *Trans. Asme* 66.8 (1944), pp. 671–684.

[52] L.F. Moody. “Friction factors for pipe flow”. In: *Trans. Asme* 66.8 (1944), pp. 671–684. URL: http://www.chem.mtu.edu/~fmorriso/cm310/MoodyLFpaper1944.pdf.

[53] Y. Morinishi et al. “Fully conservative higher order finite difference schemes for incompressible flow”. In: *J. Comput. Phys.* 143 (1998), pp. 90–124.

[54] P. J. Mulhearn. “A wind-tunnel boundary-layer study of the effects of a surface roughness change: Rough to smooth”. In: *Boundary-Layer Meteorology* 15.1 (Aug. 1978), pp. 3–30. ISSN: 1573-1472. DOI: 10.1007/BF00165503. URL: https://doi.org/10.1007/BF00165503.

[55] H.M. Nagib, K.A. Chauhan, and P.A. Monkewitz. “Approach to an asymptotic state for zero pressure gradient turbulent boundary layers”. In: *Philosophical Transactions of the Royal Society A: Mathematical, Physical and Engineering Sciences* 365.1852 (2007), p. 755.

[56] T. B. Nickels et al. “Some predictions of the attached eddy model for a high Reynolds number boundary layer”. In: *Phil. Trans. R. Soc.* A 365 (2007), pp. 807–822.

[57] J. Nikuradse. “Law of the wall in rough pipes”. In: *NASA Tech. Memo. 1292* (1933).

[58] B Nugroho, N Hutchins, and JP Monty. “Effects of diverging and converging roughness on turbulent boundary layers”. In: *Proceedings of the 18th Australasian Fluid Mechanics Conference (LauncetonAustralia,)* 2012.

[59] J.M. Österlund. “Experimental studies of zero pressure-gradient turbulent boundary layer flow”. PhD thesis. KTH, Mechanics, 1999.

[60] J. B. Perot. “An analysis of the Fractional Step Method”. In: *J. Comput. Phys.* 108 (1993), pp. 51–58.

[61] A. E. Perry and P. N. Joubert. “Rough-wall boundary layers in adverse pressure gradients”. In: *Journal of Fluid Mechanics* 17.2 (1963), pp. 193–211. DOI: 10.1017/S0022112063001245.

[62] S.B. Pope. “Ten questions concerning the large-eddy simulation of turbulent flows”. In: *New Journal of Physics* 6 (2004), Art. 35.

[63] S.B. Pope. *Turbulent Flows*. Cambridge University Press, 2002.

[64] *Über Flüssigkeitsbewegungen bei sehr kleiner Reibung*. Verhandlungen des III. 1904.

[65] L. Prandtl and H. Schlichting. “Das Widerstandsgesetz rauher Platten”. In: *Werft, Reederei, Hafen* 15.S 1 (1934), p. 4.

[66] M. R. Raupach, R. A. Antonia, and S. Rajagopalan. “Rough-Wall Turbulent Boundary Layers”. In: *Applied Mechanics Reviews* 44.1 (1991), pp. 1–25. DOI: 10.1115/1.3119492. URL: http://link.aip.org/link/?AMR/44/1/1.

[67] O. Reynolds. “An Experimental Investigation of the Circumstances Which Determine Whether the Motion of Water Shall Be Direct or Sinuous, and of the Law of Resistance in Parallel Channels”. In: *Philosophical Transactions of the Royal Society of London* 174 (1883), pp. 935–982. ISSN: 02610523. URL: http://www.jstor.org/stable/109431.

[68] LF Richardson. “Weather Prediction by Numerical Process”. In: (1922).

[69] JC Rotta. “Turbulent boundary layers in incompressible flow”. In: *Progress in Aerospace Sciences* 2.1 (1962), pp. 1–219.

[70] Namiko Saito. “Large-eddy simulations of fully developed turbulent channel and pipe flows with smooth and rough walls”. PhD thesis. California Institute of Technology, 2014.

[71] Namiko Saito, Dale I Pullin, and Michio Inoue. “Large eddy simulation of smooth-wall, transitional and fully rough-wall channel flow”. In: *Physics of Fluids (1994-present)* 24.7 (2012), p. 075103.

[72] Namiko Saito and DI Pullin. “Large eddy simulation of smooth–rough–smooth transitions in turbulent channel flows”. In: *International Journal of Heat and Mass Transfer* 78 (2014), pp. 707–720.

[73] Sergiy A. Savelyev and Peter A. Taylor. “Internal Boundary Layers: I. Height Formulae for Neutral and Diabatic Flows”. In: *Boundary-Layer Meteorology* 115.1 (Apr. 2005), pp. 1–25. ISSN: 1573-1472. DOI: 10.1007/s10546-004-2122-z. URL: https://doi.org/10.1007/s10546-004-2122-z.

[74] Taraneh Sayadi, Curtis W. Hamman, and Parviz Moin. “Direct numerical simulation of complete H-type and K-type transitions with implications for the dynamics of turbulent boundary layers”. In: *Journal of Fluid Mechanics* 724 (2013), pp. 480–509. DOI: 10.1017/jfm.2013.142.

[75] Taraneh Sayadi and Parviz Moin. “Large eddy simulation of controlled transition to turbulence”. In: *Physics of Fluids* 24.11 (2012), p. 114103. DOI: 10.1063/1.4767537. eprint: https://doi.org/10.1063/1.4767537. URL: https://doi.org/10.1063/1.4767537.

[76] M. P. Schultz and K. A. Flack. “The rough-wall turbulent boundary layer from the hydraulically smooth to the fully rough regime”. In: *Journal of Fluid Mechanics* 580 (2007), pp. 381–405. DOI: 10.1017/S0022112007005502.

[77] M. P. Schultz et al. “Economic impact of biofouling on a naval surface ship”. In: *Biofouling* 27.1 (2011). PMID: 21161774, pp. 87–98. DOI: 10.1080/08927014.2010.542809. eprint: https://doi.org/10.1080/08927014.2010.542809. URL: https://doi.org/10.1080/08927014.2010.542809.

[78] M. A. Shockling, J. J. Allen, and A. J. Smits. “Roughness Effects in Turbulent Pipe Flow”. In: *J. Fluid Mech.* 564 (2006), pp. 267–285. DOI: 10.1017/S0022112006001467.

[79] Roger L Simpson. “A generalized correlation of roughness density effects on the turbulent boundary layer.” In: *AIAA Journal* 11.2 (1973), pp. 242–244.

[80] A.J. Smits and D.H. Wood. “The Response of Turbulent Boundary Layers to Sudden Perturbations”. In: *Annual Review of Fluid Mechanics* 17.1 (1985), pp. 321–358. DOI: 10.1146/annurev.fl.17.010185.001541.

[81] P. R. Spalart, R. D. Moser, and M. M. Rogers. “Spectral methods for the Navier–Stokes equations with one infinite and two periodic directions”. In: *J. Comp. Phys.* 96 (1991), pp. 297–324.

[82] DT Squire et al. “Comparison of turbulent boundary layers over smooth and rough surfaces up to high Reynolds numbers”. In: *Journal of Fluid Mechanics* 795 (2016), pp. 210–240.

[83] A. Sridhar, D. I. Pullin, and W. Cheng. “Rough-wall turbulent boundary layers with constant skin friction”. In: *Journal of Fluid Mechanics* 818 (2017), pp. 26–45. DOI: 10.1017/jfm.2017.132.

[84] A. Sridhar, D. I. Pullin, and W. Cheng. “Rough-wall turbulent boundary layers with constant skin friction”. In: *Journal of Fluid Mechanics* 818 (2017), pp. 26–45. DOI: 10.1017/jfm.2017.132.

[85] K.M. Talluru et al. “Self preservation in a zero pressure gradient rough-wall turbulent boundary layer”. In: *Journal of Fluid Mechanics* 788 (2016), pp. 57–69.

[86] A. A. Townsend. *The structure of turbulent shear flow*. second. Cambridge University Press, 1976.

[87] T. Von Kármán. “Mechanical similitude and turbulence”. In: *NACA Technical Memorandum 611* (1931).

[88] X. Wu and P. Moin. “Direct numerical simulation of turbulence in a nominally-zero-pressure-gradient flat-plate boundary layer”. In: *Journal of Fluid Mechanics* 630.-1 (2009), pp. 5–41.

[89] Zheng-Tong Xie, Omduth Coceal, and Ian P. Castro. “Large-Eddy Simulation of Flows over Random Urban-like Obstacles”. In: *Boundary-Layer Meteorology* 129.1 (Aug. 2008), p. 1. ISSN: 1573-1472. DOI: 10.1007/s10546-008-9290-1. URL: https://doi.org/10.1007/s10546-008-9290-1.

Appendix A

NUMERICAL STABILITY WITH MARGINALLY SUBGRID ROUGHNESS

A brief comment is included here on the suitability of the virtual-wall stretched vortex subgrid scale model at low Reynolds numbers. In chapter 5 we attempted a comparison with the low Reynolds number experiments ($Re_\tau = 3500$) of our collaborators at the University of Melbourne. If we require the criteria determined by Jiménez [35] (for rough-wall flow rather than flow over obstacles) $\delta/k_s > 40$ at low Re, we require that, with the present mesh configuration, k_s approaches the vertical grid size Δz. At this point we can no longer consider the roughness to be strictly subgrid, since we define $h_0 = 0.18\Delta z$ as the vertical extent of the virtual wall. In running simulations at such low Re, two issues presented themselves. Either the code crashes within 1-2 particle transition times, or large fluctuations in C_f upstream of the roughness transition are observed. Attempting the calculation at an equivalent Re_τ for case RL while keeping $k_s^+ > 100$ violates the subgrid assumption, and the measure $k_s > 3h_0$, where h_0 is the virtual wall height in the wall-modelled LES. We note rapid deterioration of the solution via numerical instabilities (streamwise oscillations in C_f such that the upstream state is not considered to be in equilibrium) in this case, and therefore do not present results in the asymptotically rough regime for the lowest Re_τ case. Thus we restrict our primary set of simulations to have large k_s^+ in the asymptotically rough regime with large Reynolds numbers. One other minor concern noticed throughout this LES study (and in previous usage of the present model and numerical methods through boundary layer, channel flows) is a near wall effect which, while predicting u_τ reasonably well (based on validation tests presented in Chung [15] and Saito and Pullin [72] and in chapter 5), is the existence of slight discrepancies in mean velocity profiles and turbulent stresses over the first 3 grid points. These do not appear to have a major effect on the exterior flow behaviour, and minimal log-layer mismatch is observed.